Leiden University
Delft University of Technology
Erasmus University Rotterdam

Mitigating Neuropathic Pain: From Theory to Practice

Inhibiting Neuroma Pain *In-silico* and Measuring Neural Activity *In-vivo*

U.C.A.M. Verzijl

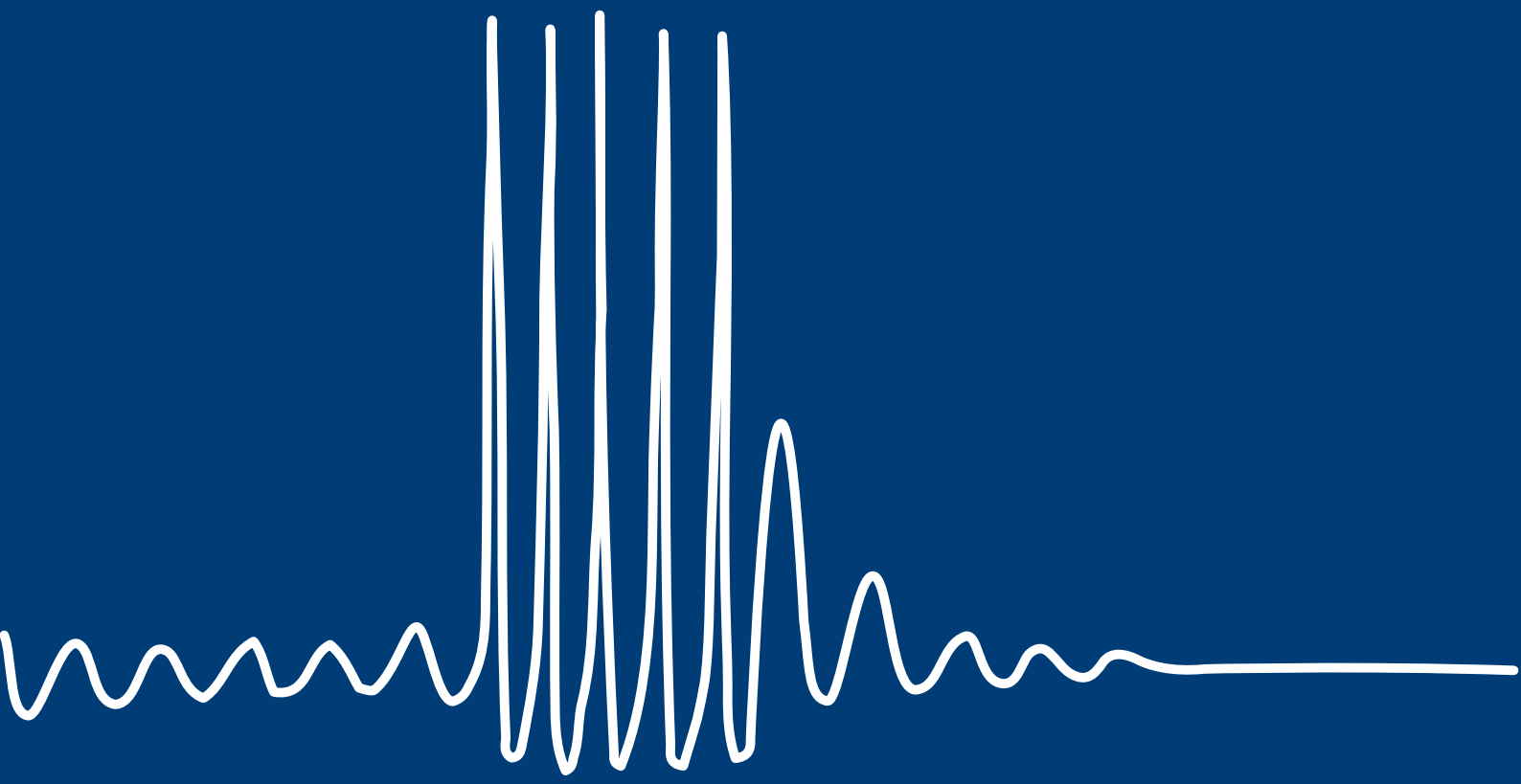

TU Delft

LUMC Leiden University Medical Center

Mitigating Neuropathic Pain: From Theory to Practice

Inhibiting Neuroma Pain *In-silico* and Measuring Neural Activity *In-vivo*

by

U.C.A.M. Verzijl

in partial fulfilment of the requirements for

the degree of
Master of Science
in Systems and Control
at the Delft University of Technology

and

the joint degree of
Master of Science
in Technical Medicine
at the Leiden University, the Delft University of Technology, and the Erasmus University Rotterdam

to be defended publicly on Tuesday October 26, 2021 at 14:00.

Student number:	4257936		
Project duration:	October 1, 2020 – October 26, 2021		
Project location:	Department of Neurosurgery, *Leiden University Medical Center* (LUMC)		
	Department of Systems and Control, *Delft University of Technology* (TU Delft)		
Thesis committee:	Prof.dr. M.J.A. Malessy,	Chair, TM Medical supervisor,	LUMC
	Prof.dr.ir. W.A. Serdijn,	TM Technical supervisor,	TU Delft
	Dr. S. Pequito,	S&C supervisor,	TU Delft
	Dr. S.G.A. van Neerven,	TM Medical supervisor,	LUMC
	K. Kolovou-Kouri, M.Sc.,	TM Technical supervisor,	TU Delft
	Prof.dr.ir. J. Harlaar,	External thesis evaluation,	TU Delft
	Dr. M. Negrello,	External thesis evaluation,	Erasmus MC

This thesis is confidential and cannot be made public until October 26, 2022.

Universiteit Leiden The Netherlands

TU Delft Delft University of Technology

Erasmus University Rotterdam

Preface

During my *Technical Medicine* clinical internships, I had the chance to speak with neuropathic pain patients. These patients experience terrible pain throughout the day, which is very hard to comprehend as a healthy person. It is not surprising that these patients score their *Quality of Life* far worse compared to healthy people. In one of the conversations with Prof.dr. M.J.A. Malessy, my clinical internship supervisor at the time, we brainstormed on methods to mitigate neuropathic pain at the peripheral level: we could focus on the origins of neuropathic pain and try to inhibit the neural signals that cause it. That meeting formed the basis of this thesis where I combine the medical knowledge from the *Technical Medicine* master program, and the technical knowledge from the *Systems and Control* master program to inhibit neuroma pain *in-silico* and measure neural activity *in-vivo*.

Before I start to take you as a reader through my thesis project, I would like to thank some people and organizations for helping me during my thesis. First, my supervisors, Prof.dr. M.J.A. Malessy, Prof.dr.ir. W.A. Serdijn, Dr. S. Pequito, Dr. S.G.A. van Neerven, and K. Kolovou-Kouri, M.Sc., for guiding me during the ups-and-downs of this project. Without you as supervisors, this work would have looked totally different. The process of writing a scientific article together was very educational.

I would like to thank Prof.dr. M. Devor for pointing out to me the possibility to use the software of the extended Hodgkin-Huxley model through the open-access *ModelDB database* and Dr. O. Dick for sharing her software implementation of the extended Hodgkin-Huxley model by email. I express my thanks to Ing. J. Bastemeijer for helping me with the design of the amplifier, the Jitter company for providing software examples of GUI design, Mr. M. Chalaki for helping me during the *in-vivo* experiments, Dr. S. Chatterjee for sharing software for the *in-silico* experiments, and Dr. V. Giagka for giving feedback on my work. Furthermore, I express my thanks to Prof.dr.ir. J. Harlaar and Dr. M. Negrello for being in my graduation committee, and the Painless foundation for supporting this research.

I would also like to thank my parents, who have proofread my work. My girlfriend has always been there to give me advice and has reviewed some parts; many thanks!

Finally, I would like to thank the developers of the *Zoom Video Communications* platform for developing such an excellent teleconferencing tool. It was indispensable during the coronavirus pandemic.

U.C.A.M. (Hubald) Verzijl
Delft, October 2021

Summary

Neuropathic pain (NP) affects approximately seven to ten percent of the general population. Seventeen percent of NP patients scored their life as “worse than death”. A myriad of causes may underlie NP, such as stroke or spinal cord injury. Also, damage or disease of the *peripheral nervous system* (PNS) may result in NP. One of the main issues of NP caused by a *peripheral nerve injury* (PNI) is the development of a neuroma, which is a tumor-like mass at the proximal end of a severed nerve that can become very painful. Neuromas show unique neurophysiological characteristics. Cell membrane alternations lead to different ion channel distributions, which in turn result in *subthreshold oscillations* (SO) and *ectopic discharges* (ED). It is assumed that this behavior could lead to NP generation.

Electrical neurostimulation (ENS) is used to treat patients, thereby applying pre-programmed stimulation patterns to the affected nerves. However, the pain-provoking signals which run through the nerves are not detected and analyzed before ENS is provided. Furthermore, it is questionable whether (the currently applied) pre-programmed ENS defuses these signals anyway. In addition, pre-programmed ENS is not effective at all moments of the pain experience caused by fluctuations in signal intensity. As the clinical results are discouraging, and in view of the high costs, the popularity of this technology is currently waning. Optimization of this potentially powerful technique is needed to improve the outcome and make this technology useful to implement in the treatment strategy of patients with intractable otherwise difficult to treat pain syndromes. Theoretically, optimization of stimulation technology is possible by actually neutralizing SO and ED, which should lead to mitigating the generation of NP.

We propose an approach to neutralize SO and ED consisting of several steps. Firstly, the nerve activity is real-time monitored. Secondly, a decision mechanism (called a ‘controller’) is developed that constructs *electrical neurostimulation* (ENS) patterns to neutralize SO and ED. Finally, these patterns are actually applied to the nerve by an electrical stimulator.

To design a SO and ED neutralizing controller, we seek to provide a data-driven real-time (closed-loop) ENS that suppresses SO and ED in individual neurons *in-silico*. Because of related stimulation, neurophysiological, and computational limitation constraints, we leverage a scheme known as *model predictive control* (MPC). We use a class of models known as *fractional-order systems* (FOS) as a proxy to avoid complex models. We show that by applying MPC with a FOS proxy, it is possible to neutralize SO and ED in three well-established mathematical models of neuropathic pain. Since SO and ED are considered drivers of NP, suppression might mitigate NP.

To apply our approach, a dedicated setup is required, capable of measuring the pain-provoking signals in nerves (which are in the range of 10 µV), while embedding processing power and extensions for simultaneous stimulation. As this setup is currently unavailable, we designed a hardware setup consisting of a preamplifier, a main amplifier, and corresponding software to control the setup. Analog band-pass filters, the driven right leg circuit, and shielding techniques were implemented to increase the maximum signal-to-noise ratio. We validated the setup using specifically designed artificial calibration signals. During *in-vivo* experiments, recordings of nerve action potentials were performed in lugworms and in the sciatic nerve of rats, which revealed single-unit and multi-unit neural activity. This full functional, validated and *in-vivo* tested neural amplifier for microneurography can thus measure activity from a peripheral origin, potentially also pain-related activity, such as SO and ED. Additionally, this setup could implement real-time closed-loop ENS to suppress SO and ED *in-vivo*.

To close the loop, the suggested (arbitrary shaped) ENS patterns from the *in-silico* experiments should be applied at the level of the peripheral nerve. Currently, available ENS systems cannot apply arbitrary waveforms to biological tissue. We elaborated on methods to implement arbitrary waveforms using *pulse-width modulated* (PWM) signals by taking advantage of the biological tissue’s dielectric properties. Increasing the PWM frequency is required, or a low-pass filter should be added to the stimulator’s output.

This thesis provides the essential information to eventually apply our theoretical proposed strategy *in-vivo*. We conclude this work with a review of the ultimate goal: relief of NP. We outline the next steps within this project, and we make some recommendations for further research to translate *NP mitigation from theory to practice*.

Contents

Preface iii

Summary v

Contents vii

General introduction 1
Neuropathic pain . . . 1
Affect neuroma behavior . . . 2
Extended neural signal amplifier for microneurography . . . 2
An arbitrary waveform electrical neurostimulator . . . 3
Outcome of the thesis . . . 3
Outline of the thesis . . . 3

1 Neurostimulation to mitigate neuroma pain using closed-loop control 5
1.1 Introduction . . . 6
1.2 Data and methods . . . 6
1.2.1 Cell membrane and action potentials . . . 6
1.2.2 Subthreshold oscillations and ectopic discharges . . . 7
1.2.3 State-of-the-art mathematical models of spontaneous neuroma discharge . . . 7
1.2.4 Dynamical system-based feedback control . . . 11
1.3 Simulation results . . . 14
1.3.1 Extended Hodgkin-Huxley model . . . 14
1.3.2 Extended Morris-Lecar model . . . 15
1.3.3 Extended map-based model . . . 16
1.4 Discussion . . . 17
1.4.1 Mitigating neuropathic pain . . . 17
1.4.2 Computational implementation remarks . . . 17
1.4.3 State-of-the-art versus proposed control . . . 17
1.4.4 Implications for real-time neurostimulation . . . 18
1.4.5 Translation to in-vivo experiments . . . 19
1.5 Conclusion . . . 19

2 Design of an extended neural signal amplifier for microneurography 21
2.1 Introduction . . . 22
2.1.1 Nervous system . . . 22
2.1.2 Microneurography . . . 23
2.1.3 Interference . . . 24
2.1.4 Available hardware for microneurography . . . 25
2.1.5 Hardware proposal and requirements for microneurography . . . 26
2.1.6 Chapter structure . . . 26
2.2 System design . . . 27
2.2.1 Global system design . . . 27
2.2.2 Filter design background . . . 27
2.2.3 Driven right leg circuit background . . . 29
2.2.4 Preamplifier v1.0 . . . 30
2.2.5 Preamplifier v2.0 . . . 33
2.2.6 Main amplifier . . . 37
2.2.7 Software . . . 41

2.3 System validation . . . 47
2.3.1 Main amplifier . . . 47
2.3.2 Preamplifier v2.0 . . . 49
2.4 In-vivo experiments . . . 53
2.4.1 Measurements in lugworms . . . 53
2.4.2 Measurements in rats . . . 56
2.5 Discussion . . . 61
2.5.1 Amplifier's gain . . . 61
2.5.2 Too much bandwidth . . . 61
2.5.3 Interference rejection . . . 61
2.5.4 Digitization and real-time data visualization . . . 61
2.5.5 Recorded action potential shape . . . 62
2.5.6 Lugworm's ventral nerve cord versus rat's sciatic nerve . . . 62
2.5.7 Setup improvements . . . 63
2.6 Conclusion . . . 63

3 A discussion on arbitrary waveform electrical neurostimulators 65
3.1 Introduction . . . 66
3.1.1 Direct electrical stimulation . . . 66
3.1.2 Stimulus mode . . . 66
3.1.3 Stimulus shape . . . 66
3.1.4 Ultra-high frequency stimulation . . . 67
3.1.5 Chapter structure . . . 67
3.2 Basic stimulator . . . 68
3.2.1 Circuit design . . . 68
3.2.2 Board design . . . 69
3.2.3 Validation . . . 69
3.3 Up-grade stimulator . . . 70
3.3.1 Modeling biological tissue . . . 70
3.3.2 Tissue potential following current stimulation . . . 71
3.3.3 Implementation of an arbitrary tissue voltage shape . . . 72
3.4 Discussion . . . 73
3.4.1 Basic stimulator design limitations . . . 73
3.4.2 Stimulator extensions . . . 73
3.4.3 Arbitrary current waveforms . . . 74
3.4.4 Charge balancing . . . 74
3.5 Conclusion . . . 74

General discussion 75
Mitigating neuropathic pain . . . 75
From theory to practice . . . 76

A Appendixes 79
A.1 Modeling subthreshold oscillations and ectopic discharge . . . 79
A.1.1 Extended Hodgkin-Huxley model . . . 79
A.1.2 Extended Morris-Lecar model . . . 80
A.1.3 Extended map-based model . . . 81
A.2 An MPC with fractional-dynamics proxy approach using a linear control scheme . . . 82
A.3 An open-loop strategy with predetermined stimulation patterns using the ML model . . . 83
A.4 An MPC with fractional-dynamics proxy approach including additional constraints . . . 84
A.4.1 Biphasic pulse constraint . . . 84
A.4.2 Charge balancing constraint . . . 84
A.4.3 Complicated optimization problems . . . 84
A.5 Types of axons . . . 86
A.6 Recording neuronal activity . . . 87
A.6.1 Intracellular recording . . . 87
A.6.2 Extracellular recording . . . 87

A.7 Theoretical Bode plots of the preamplifier v2.0 88
A.8 Preamplifier schematic 89
A.9 Main amplifier schematic 90
A.10 Main amplifier PCB regions 96
A.11 PCB assembling process 97
A.12 Stimulator power efficiency 98
A.13 Basic stimulator schematic 99

References **101**

General introduction

Neuropathic pain

Neuropathic pain (NP) affects approximately seven to ten percent of the general population [1]. NP is one of the main types of chronic pain, and is defined by the *International Association for the Study of Pain* (IASP) as “pain caused by damage or disease affecting the somatosensory nervous system” [2]. NP hugely impacts a patient’s everyday life, either at work or at home [3]. A questionnaire among NP patients revealed that seventeen percent scored their life as “worse than death” [4, 5].

In principal, the treatment of NP focuses on the source of the pain. However, a myriad of causes may underlie NP. Any type of injury to the *central nervous system* (CNS), such as stroke or spinal cord injury, may lead to the development of a central NP syndrome [6]. Also, damage or disease of the *peripheral nervous system* (PNS) may result in NP, e.g., *peripheral nerve injuries* (PNI) due to trauma or surgery [6]. One of the main issues of NP caused by a PNI is the development of a *neuroma*. Neuroma formation following PNI may occur, and that is the result of an unsuccessful neuro-regeneration process unable to restore original axonal connections. A neuroma is a *tumor-like* mass at the proximal end of a severed nerve that can become very painful [7].

In case a painful neuroma has developed, the first step to relieve pain is by using medications. Unfortunately, specific neuropathic painkillers do not exist since the exact cause of NP generation is unknown. Therefore, NP is treated with unconventional analgesics; these medications have other indications in other medical settings and are not normally thought of as analgesics [8]. Considering NP, an antidepressant such as amitriptyline can be used to treat NP [9]. The medications to treat NP are, however, frequently ineffective or induce severe side effects, such as drowsiness [10, 11]. In selected cases, resection of the neuroma may be considered [12], which also does not consistently lead to pain relief. Patients may still experience NP even after the neuroma has been resected [13, 14]. An alternative treatment option for NP is *electrical neurostimulation* (ENS), which can be applied at different target levels, e.g., the peripheral nerve or spinal cord [15, 16]. In *open-loop* ENS, pre-programmed patterns of electrical pulses are applied via electrodes [17, 18]. These systems do not always result in pain relief for all types of chronic pain either [16]. The downside of open-loop ENS is that the patterns are predefined and independent of any signals in the body that are interpreted by the brain as ‘pain’. Therefore, open-loop ENS may not even diminish these pain-provoking signals. Furthermore, open-loop ENS is not effective at all moments of the pain experience caused by fluctuations in signal intensity. In addition, the side effect of open-loop ENS is the generation of a constant cumbersome sensation in an area that is larger than the original pain area. As the clinical results are disappointing, and in view of the high costs, the popularity of this technology is currently waning. Optimization of this potentially powerful technique is needed to improve the outcome and make this technology useful to implement in the treatment strategy of patients with intractable otherwise difficult to treat pain syndromes.

Neuromas show unique neurophysiological characteristics. Cell membrane alternations result in different ion channel distributions [19–21], which in turn result in *subthreshold oscillations* (SO) and *ectopic discharges* (ED) [22]. It is assumed that this behavior could lead to NP generation [22]. Theoretically, by neutralizing SO and ED, it should be possible to mitigate the generation of NP [23]. In this thesis, we defined our working hypothesis as “by neutralizing SO and ED, the generation of NP could be mitigated”. In other words, we target the NP-causing characteristics of a neuroma.

We propose a methodology to neutralize SO and ED by adapting the ENS pattern real-time in response to sensed physiological signals. This methodology is called *closed-loop* and is visualized in Figure 1; it consists of several steps. Firstly, the nerve’s activity is *real-time* monitored and compared to the ultimate goal: neutralizing SO and ED. Secondly, any deviations in the nerve activity are used by a decision mechanism (called a ‘controller’) to construct an ENS pattern that influences the activity in the nerve, such that our *goal* (neutralization of SO and ED) is achieved. Finally, the stimulation pattern is applied to the nerve by a stimulator. However, the currently available stimulation patterns are (hardware) limited. This thesis elaborates on several aspects of our proposed methodology: the controller design, the nerve monitor setup, and the stimulator design.

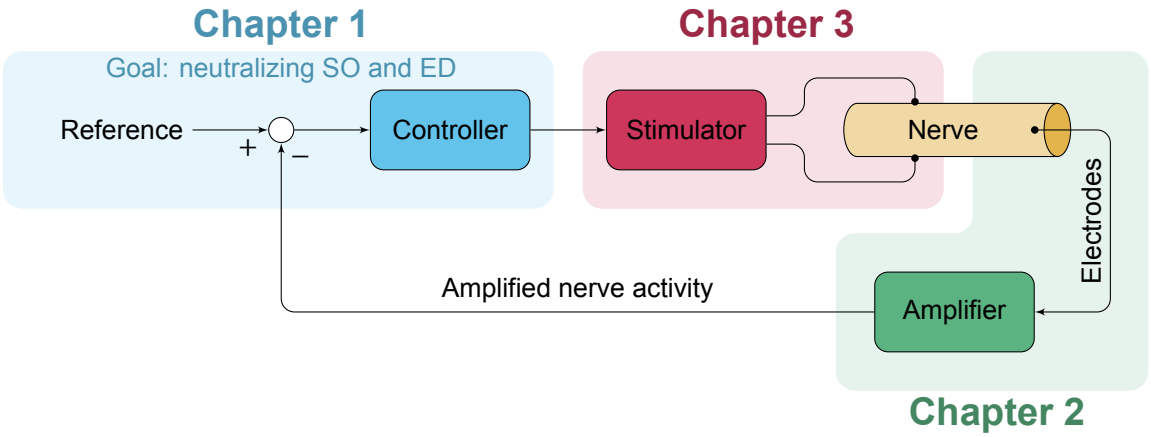

Figure 1: Proposed closed-loop methodology to neutralize SO and ED, and thereby mitigate the generation of NP. The controller determines stimulation patterns that (theoretically) neutralize SO and ED. We design the controller in Chapter 1. The controller requires real-time neural activity; therefore, electrodes are applied to a nerve to monitor the nerve activity, for which an amplifier is required. We discuss the design of a neural amplifier further in Chapter 2. Next, the stimulation pattern (obtained in the controller) is applied by the stimulator and is discussed in Chapter 3.

Affect neuroma behavior

In Chapter 1, we discuss the NP mitigation at the neuron level through ENS. In prior research, mathematical models were designed that capture the neuroma's unique neurophysiological aspects [24–26]. These models describe the SO and ED at a single axon level based on the cell membrane characteristics or phenomenological properties. We will derive specific ENS patterns to neutralize SO and ED. These patterns are data-driven and real-time updated and are applied during *in-silico* experiments on several mathematical models. In the experiments, we observed that certain ENS patterns could be found which do neutralize SO and ED. However, translating these *in-silico* findings to *in-vivo* validation experiments, entails several challenges: *(i)* the neuroma behavior must be quantifiable; and *(ii)* the ENS systems should be capable of implementing the developed ENS patterns.

Extended neural signal amplifier for microneurography

Nerve *action potentials* (AP) are electrical signals generated by the nervous system. They encode information, which is generated in the sensory organs of the body, and are conducted via peripheral nerves to the brain. Thereby, the brain receives signals regarding the status of the internal organs and the outer world. Revealing these APs gives us fundamental knowledge about the functioning of the human nervous system. For example, this information may yield helpful insights in neural functions and dysfunctions concerning blood pressure control and thermoregulation [27]. In addition, this information may be beneficial during the improvement of hand prostheses functionality [28]. Furthermore, neuromas generate activity in the PNS (in the form of SO and ED) that is interpreted by the brain as 'pain', it is also essential to detect APs that are related to the neuroma. In this way, the unique neuroma characteristics, in relation to the generation of NP, can be observed *in-vivo*. Moreover, the effect of ENS can be monitored.

Neural activity can be recorded *in-vivo* using microneurography. Commercially available hardware is available, but is, however, only capable of performing microneurography recordings, i.e., there are no possibilities of performing calculations online (or *real-time*) by the hardware itself. In addition, the available setup does not allow to connect additional hardware, e.g., an ENS system. These shortcomings emphasize the need for improvement by a dedicated setup, capable of measuring this nerve activity, while embedding processing power and extensions for simultaneous stimulation. Therefore, we focus in Chapter 2 on the design of an *open-source* neural signal amplifier for microneurography that tackles classical problems with interference rejection, ease of use, and customizability. This design should include possibilities to perform online calculations, connect additional hardware, and should be able to implement algorithms that require simultaneous neural recording and stimulation. We designed a full functional, validated and *in-vivo* tested microneurography amplifier.

An arbitrary waveform electrical neurostimulator

Neural signals which run within the peripheral nerve can be blocked or altered in order to reduce the generation of pain, which is currently done by applying open-loop ENS. Electrical neurostimulators can activate the tissue using several stimulation techniques [29]. However, the stimulation patterns as suggested in Chapter 1 (to reduce the generation of pain) cannot be applied by the stimulator right away: the stimulation hardware is restricted to a number of patterns.

In Chapter 3 we elaborate on a basic stimulator design and discuss extensions that use the biological tissue's characteristics to apply arbitrary electrical waveforms. Using these extensions, future experiments could be performed that validate the SO and ED suppression *in-vivo*.

Outcome of the thesis

This thesis has several outcomes. Firstly, the *in-silico* experiments (Chapter 1) show that ENS patterns can be derived which are able to neutralize SO and ED, and so, the generation of NP could potentially be blocked. These findings contribute to improving ENS technology for the treatment of NP pain caused by neuromas and different sources with similar phenomenological characteristics. The content of Chapter 1 has been used for a scientific paper that is currently under review:

U.C.A.M. Verzijl, M.J.A. Malessy, S.G.A. van Neerven, W.A. Serdijn, K. Kolovou-Kouri, V. Giagka, and S. Pequito (2021). *"Mitigating neuropathic pain at the neuron level through electrical neurostimulation: a model predictive control approach with fractional-dynamics proxy".*

Secondly, our work covers multiple aspects of mitigating NP. Besides the theoretical point of view, we incorporate the practical side of NP mitigation, such as recording neural activity and stimulating neural tissue. These combined conditions result in valuable insights into how NP could be mitigated in future research. Thirdly, this thesis has led to the development of a functional signal amplifier for microneurography with a user-friendly setup that can be applied to measure the activity in nerves, while embedding processing power and extensions for simultaneous stimulation. It is a first step in tackling the limitations of existing hardware and shows promising results for future development aimed at neutralizing the NP generating activity.

Outline of the thesis

This master thesis reflects research performed in a combined setting of two master programs: Systems and Control at the Delft University of Technology and the joint program Technical Medicine at the Leiden University, the Delft University of Technology, and the Erasmus University Rotterdam.

Chapter 1 focuses on neutralizing neuroma behavior *in-silico* causing neuropathic pain. The chapter covers the Systems and Control research activities of this project and consists of *(i)* mathematical models mimicking neuroma behavior; *(ii)* the development of a control strategy to neutralize SO and ED; and *(iii)* the conduction of various *in-silico* experiments.

Chapter 2 and Chapter 3 cover the Technical Medicine research activities. Chapter 2 presents the design of a neural signal amplifier, including the design requirements for successful microneurography recordings, design considerations, setup validation, and *in-vivo* experiments. In Chapter 3, the basic requirements for the design of a stimulator are presented, and several options are introduced to extend the design to implement arbitrary waveforms using the biological tissue's dynamics.

Finally, in the general discussion, we reflect on the findings of our research and look into possible future *in-vivo* experiments to validate our *in-silico* findings.

1

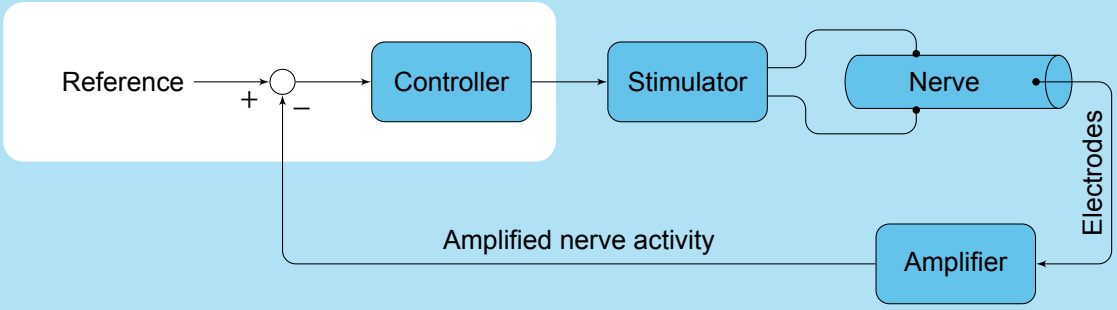
Reference
+
–
Controller
Stimulator
Nerve
Electrodes
Amplified nerve activity
Amplifier

1

Mitigating neuropathic pain at the neuron level through electrical neurostimulation: a model predictive control approach with fractional-dynamics proxy

Objective: To suppress neuropathic pain at the neuron level through electrical stimulation.
Approach: Today's electrical stimulators are open-loop or event-triggered. We seek to provide a data-driven real-time (closed-loop) electrical neurostimulation that suppresses neuropathic pain *in-silico* under the assumption that this pain is generated in a neuroma by subthreshold oscillations (SO) and ectopic discharges (ED) in individual neurons. Because of related stimulation, neurophysiological, and computational limitation constraints, we leverage a scheme known as model predictive control (MPC). We use a class of models known as fractional-order systems (FOS) as a proxy to avoid complex models. We consider three well-established mathematical models of neuropathic pain. The first two models are based on neurophysiological principles; and the third model is based on a phenomenological modeling approach. Specifically, we consider the stimulation pattern required to regulate the FOS to regulate the mathematical model of a neuron.
Main results: We show that by applying MPC with a FOS proxy, it is possible to suppress SO and ED at the single-axon level.
Significance: Our *in-silico* results suggest that at a single-axon level, SO and ED can be suppressed. Since SO and ED are considered drivers of neuropathic pain, suppression might mitigate pain. Our findings contribute to improving electrical stimulation technology for the treatment of neuropathic pain caused by neuromas and different sources with similar phenomenological characteristics.

1.1 Introduction

Peripheral nerve injuries (PNI) may result in the development of a neuroma that could become painful [6]. In case a painful neuroma developed, the first step to relieve pain is by using specific neuropathic painkillers, such as amitriptyline [9]. Unfortunately, these types of medications are frequently ineffective or induce severe side effects, such as drowsiness [10]. In selected cases, resection of the neuroma may be considered [12], which also does not always lead to pain relief. Patients may still experience *neuropathic pain* (NP) even after the neuroma has been resected [13, 14]. An alternative treatment option for NP is *electrical neurostimulation* (ENS), which can be applied at different target levels, e.g., the peripheral nerve or spinal cord [15, 16]. In ENS, electrical pulses are applied via electrodes [18]. Patients experience the stimuli as a constantly present (non-painful) tingling sensation, which may, to a certain extend, mask the pain [16, 30]. Different stimulation schemes can be applied to reduce the pain. If a stimulation scheme is defined before the application and is, therefore, without real-time (or 'on the fly') adjustments, it is called *open-loop* stimulation [31].

In contrast, *closed-loop* stimulation is data-driven. It adapts the level and intensity of the provided stimuli based on measurements of pain-causing processes. This type of stimulation can be either *responsive* or with *real-time feedback*. In a closed-loop setting, measurements of specific processes that cause pain are used to update the stimulation scheme, thereby aiming at optimization of pain neutralization. This contrasts with the former that uses a predefined set of strategies to address specific (broader) scenarios. That said, pain-generating neuromas have unique pathophysiological properties which do not occur in healthy nervous tissue: *(i)* an increase of *subthreshold oscillations* (SO); and *(ii) ectopic discharges* (ED). Both SO and ED likely underlie the generation of NP [22, 23]. Our *working hypothesis* is that NP generation can be naturalized by suppressing SO and ED, as was suggested in theory before [23]. In order to suppress SO and ED, a closed-loop ENS need to be developed that will minimize the rate of the ED and/or the amplitude of the SO.

In what follows, we aim to develop a (data-driven) system that continuously adapts the stimulation scheme based on real-time tissue measurements to suppress SO and ED on a single-axon level. In order to develop data-driven real-time ENS to mitigate NP, it is of importance to show first whether it is theoretically possible to neutralize SO and ED *in-silico*. We present the fundamentals of mathematical modeling and introduce several mathematical models which capture the neuroma firing pattern. Next, we enumerate the fundamentals of feedback, model predictive control, and fractional-order models. These different concepts are applied using simulations on several well-established mathematical neuroma models to show how SO, ED, and potentially NP can be neutralized. Data-driven real-time ENS has the potential to optimize the pain neutralizing effect and solve problems related to habituation and fluctuating pain experience. We envisage that a closed-loop strategy will prevent over- and under-stimulation and, therefore, reduce the need for painkillers and enhance the individual's quality of life in the long term. Data-driven real-time ENS possesses the potential to treat NP not only caused by a neuroma, but also pain generated by different sources with similar phenomenological characteristics.

1.2 Data and methods

This section is organized in subsections. Firstly, the nerve anatomy relevant for the development of NP and action potential generation is reviewed. Subsequently, the current understanding of SO and ED generation within a neuroma leading to NP will be outlined. Additionally, several mathematical models that capture the neuropathophysiological processes of SO and ED in the neuroma will be described. We will conclude this section with our proposed dynamical system-based feedback control scheme to suppress SO and ED *in-silico*.

1.2.1 Cell membrane and action potentials

The *peripheral nervous system* (PNS) connects the *central nervous system* (CNS) to the end-organs in the limbs and organs. The PNS is composed of numerous nerves that conduct information from the periphery to the CNS and vice versa. This information is encoded in *action potentials* (AP). A peripheral nerve contains multiple axons depending on its location and type. The axons are the extensions of the nerve cell (also called *neuron*), connecting the cell with the end organ in the body. The axon is a hollow tube-like structure consisting of a *membrane*, the *axolemma*, containing *cytoplasm* or *axoplasm*. Each axon throughout its length is wrapped around by multiple *Schwann cells*. These cells form a myelin sheath for insulation. Between the Schwann cells lie uninsulated gaps, called *nodes of Ranvier*. Here,

the axolemma is exposed to the extracellular space.

Ion channels are located within the nodes. These channels are specialized proteins through which charged ions can cross the membrane, e.g., sodium (Na^+), potassium (K^+), and some are leak channels which will be denoted as l. These channels are *voltage-gated*: the voltage (or potential) across the membrane will open or close a specific channel. The electrical voltage across the membrane that balances this system is called the *equilibrium potential* and is often around $-65\,\text{mV}$. A small external positive current stimulus of several µAs could lead to a positive membrane inward electrical current flow, depolarizing the neuron. If the cell membrane potential exceeds the *threshold potential*, an AP will be generated. An AP is a fast depolarization, repolarization, and hyperpolarization of a specific part of the neuron, depolarizing adjacent areas. Consequently, an AP is conducted along an axon, e.g., from the brain to the muscles in the foot. The AP conduction velocity is increased by saltatory conduction: the AP jumps from one node of Ranvier to the next node.

1.2.2 Subthreshold oscillations and ectopic discharges

Following axonal damage, the part of the axon which is disconnected from the cell body will disintegrate; a process called *Wallerian degeneration*. The proximal part of the axon, still in continuity with the cell body, will start to elongate and attempt to re-establish its connection with the end organ, a process called *neuroregeneration* [32]. This process is often complicated by the presence of damaged fibrous tissue around the tip of the severed axon. This fibrous tissue will block the outgrowth of axons, which results in the formation of a neuroma.

In turn, neuroma formation may lead to the development of NP elicited by the spontaneous discharge of the blocked axons in the neuroma [22]. The cell membranes of the axons in a neuroma show an abnormal distribution and typing of ion channels compared to ‘normal’ axons [19–21]. This transformed distribution results in an altered response to a small stimulus or depolarization.

Neurophysiological recordings (using patch-clamp techniques) from neuroma tissue show membrane potential fluctuations below the AP generation threshold. These fluctuations have been explained and abbreviated previously, and are called *subthreshold oscillations* (SO) [22]. Additionally, random generation of APs is observed, which are termed *ectopic discharges* (ED) [22]. SO and ED are occasionally also measured in healthy neurons [23] and are illustrative shown in Figure 1.1. However, in neuroma tissue, this behavior is amplified [22, 23]. We and others [23] hypothesize that by blocking SO and ED, the experienced NP can be reduced.

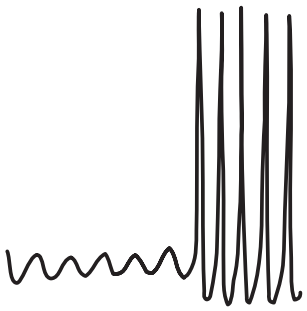

Figure 1.1: Illustration of *subthreshold oscillations* (SO) and *ectopic discharges* (ED), as measured with patch-clamp techniques. The left part of the figure contains SO (frequency of 100 Hz and amplitude around 10 mV). The right part contains randomly fired APs.

1.2.3 State-of-the-art mathematical models of spontaneous neuroma discharge

Mathematical models use the mathematical language to describe the behavior of a system. These models are able to predict the system’s future behavior for specific input conditions. In our context, mathematical models should describe and predict the neurophysiological signals of a neuroma (SO and ED) at the level of a single neuron, for different levels of stimulation currents. These models can then be used for *in-silico* experiments to show how SO and ED can be inhibited by applying our feedback control scheme. Several mathematical models of spontaneous neuroma discharge have been described in the literature, which we briefly discuss here.

State-space models are mathematical models that describe the future behavior of a system through

a finite set of time-dependent variables $x_1(t), \ldots, x_n(t) \in \mathbb{R}$ called *state variables*, grouped together in the *state vector* $x(t) \in \mathbb{R}^n$, where time $t \in \mathbb{R}_+ \equiv \{t \in \mathbb{R} \mid t \geq 0\}$ [33]. State variables can represent arbitrary characteristics of a system. In the case of a cell membrane model, these variables can represent the flow of ions through a specific ion channel. The input to the model is given by $u(t) \in \mathbb{R}^{n_u}$, and, in our case, this input is a stimulation current.

The state vector is continuously updated through a set of equations

$$\dot{x}(t) = f(t, x(t), u(t)), \tag{1.1}$$

called *continuous-time* (CT) state-space representation, where $x(0)$ is the initial condition. Additionally, $\dot{x}(t) := \frac{d}{dt}x(t)$ and $f : \mathbb{R}_+ \times \mathbb{R}^n \times \mathbb{R}^{n_u} \to \mathbb{R}^n$ is a known function which describes the dynamics of the neurophysiological system as SO and ED. Differential equation solvers are used to obtain the time-domain response. If $x(t)$ is restricted to a set of discrete points $x_k = kT$, where $k \in \mathbb{Z}_+ \equiv (0, 1, 2, \ldots)$ and T is the sampling period, the variable x_k is called the *discrete-time* (DT) variable. A DT state-space is written as

$$x_{k+1} = f(k, x_k, u_k), \tag{1.2}$$

where x_0 is the initial condition, $u_k \in \mathbb{Z}^{n_u}$ and $f : \mathbb{Z}_+ \times \mathbb{Z}^n \times \mathbb{Z}^{n_u} \to \mathbb{R}^n$ [34].

In reality, function f (CT or DT) is often a simplification of the actual system. After time t or steps k, the model's state can deviate from the actual system's state. *State estimation* is then applied to update the mathematical model's state using measurements from the real system to overcome system-model mismatch [33].

1.2.3.1 Extended Hodgkin-Huxley model

In 1952, *Hodgkin and Huxley* described the AP. They modeled the cell membrane by using a mathematical state-space representation [35]. The model since then bears their name: the *Hodgkin-Huxley* (HH) model. It expresses the current flow over time $t \in \mathbb{R}_+$, through a sodium ($I_{Na^+}(t) \in \mathbb{R}$), a potassium ($I_{K^+}(t) \in \mathbb{R}$) and a leak channel ($I_l(t) \in \mathbb{R}$) [35]. The total current through the membrane ($I(t) \in \mathbb{R}$) is defined as

$$\begin{aligned} I(t) = C_m \dot{v}_m(t) &+ \overbrace{\bar{g}_{Na^+} m(t)^3 h(t) (v_m(t) - E_{Na^+})}^{I_{Na^+}(t)} \\ &+ \overbrace{\bar{g}_{K^+} n(t)^4 (v_m(t) - E_{K^+})}^{I_{K^+}(t)} + \overbrace{\bar{g}_l (v_m(t) - E_l)}^{I_l(t)}. \end{aligned} \tag{1.3}$$

In Equation (1.3), $C_m \in \mathbb{R}_+$ is the membrane capacitance and $v_m(t) \in \mathbb{R}$ a state variable representing the membrane potential. Parameters $\bar{g}_{Na^+} \in \mathbb{R}_+$, $\bar{g}_{K^+} \in \mathbb{R}_+$, and $\bar{g}_l \in \mathbb{R}_+$ represent the channel's conductance, and $E_{Na^+} \in \mathbb{R}$, $E_{K^+} \in \mathbb{R}$, and $E_l \in \mathbb{R}$ the Nernst potential, or resting potential. The HH model contains several *gating parameters*; namely, $m(t) \in [0, 1]$, $h(t) \in [0, 1]$, and $n(t) \in [0, 1]$. These are state variables and are described by first order systems

$$\dot{m}(t) = \frac{m_\infty(v_m(t)) - m(t)}{\tau_m(v_m(t))}, \tag{1.4}$$

$$\dot{h}(t) = \frac{h_\infty(v_m(t)) - h(t)}{\tau_h(v_m(t))}, \tag{1.5}$$

$$\dot{n}(t) = \frac{n_\infty(v_m(t)) - n(t)}{\tau_n(v_m(t))}, \tag{1.6}$$

where $\dot{m}(t) \in \mathbb{R}$, $\dot{h}(t) \in \mathbb{R}$, and $\dot{n}(t) \in \mathbb{R}$. The (membrane voltage dependent) steady-state values for activation are indicated by $m_\infty(v_m(t)) \in [0, 1]$, $h_\infty(v_m(t)) \in [0, 1]$, and $n_\infty(v_m(t)) \in [0, 1]$. Lastly, $\tau_m(v_m(t)) \in \mathbb{R}_+$, $\tau_h(v_m(t)) \in \mathbb{R}_+$, and $\tau_n(v_m(t)) \in \mathbb{R}_+$ represent the (membrane voltage dependent) time constants of the different ion channels. The steady-state values for activation and time constants are ion channel-specific: by adjusting these two parameters, we can capture the dynamics of different subtypes of, e.g., Na^+ ion channels.

The mathematical HH model from Equation (1.3) appeared to be insufficient to capture SO and ED completely. Others extended the HH model to include a *fast* (F), *medium* (M), and *slow* (S) sodium

channel, and neglected the potassium channel, based on the cell membrane characteristics of a neuroma [24]. The modified HH then became

$$I(t) = C_m \dot{v}_m(t) + I^F_{Na^+}(t) + I^M_{Na^+}(t) + I^S_{Na^+}(t) + I_l(t), \tag{1.7a}$$
$$I^F_{Na^+}(t) = \bar{g}^F_{Na^+} m_F(t)^3 h_F(t)(v_m(t) - E_{Na^+}), \tag{1.7b}$$
$$I^M_{Na^+}(t) = \bar{g}^M_{Na^+} m_M(t) h_M(t)(v_m(t) - E_{Na^+}), \tag{1.7c}$$
$$I^S_{Na^+}(t) = \bar{g}^S_{Na^+} m_S(t) h_S(t)(v_m(t) - E_{Na^+}). \tag{1.7d}$$

The different $m_\infty(v_m(t))$, $\tau_m(v_m(t))$, $h_\infty(v_m(t))$, and $\tau_h(v_m(t))$ constants of each channel (S, M, and F) were modified such that they fell within the range of a *dorsal root ganglion* (DRG) neuron of a rat [24].

Figure 1.2 shows the membrane voltage over time for several input currents for the mathematical model described by Equations (1.7a) - (1.7d). This model resulted in SO and ED, with the same properties as seen during *ex-vivo* neurophysiological recordings [36]. See Appendix A.1.1 for further details on the influence of different ion channels.

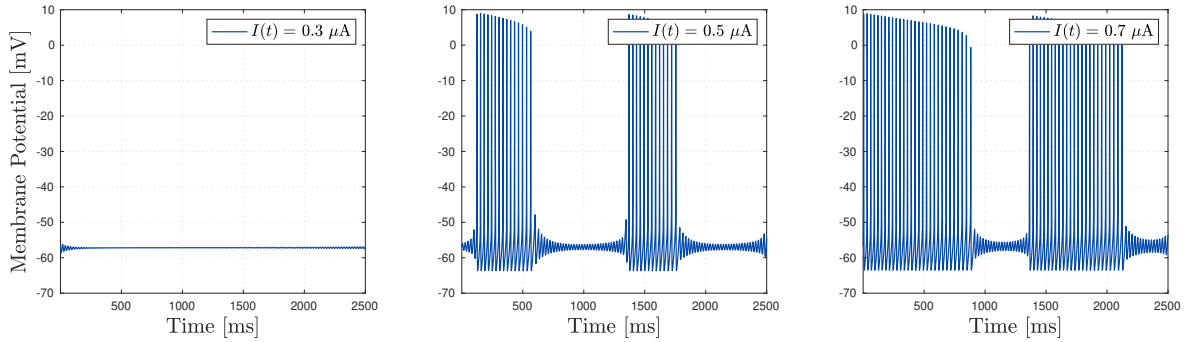

Figure 1.2: Different responses (i.e., outputs captured by $v_m(t)$) upon different stimulation inputs $I(t)$ to the extended HH model described by Equations (1.7a) - (1.7d).

1.2.3.2 Extended Morris-Lecar model

APs can also be modeled using other mathematical models. *Morris and Lecar* introduced a model that also describes the current flow through the membrane. Although the *Morris-Lecar* (ML) model uses potassium and leak channels, a calcium channel (Ca^{2+}) was implemented instead of a sodium channel [37]. Thereby, it was assumed that the Ca^{2+} ion channel is much faster (i.e., almost instantaneously) as compared to the K^+ channel at all times $t \in \mathbb{R}_+$. Formally, $\tau_{Ca^{2+}}(v_m(t)) \to 0^+$. Therefore, the dynamics of the Ca^{2+} channel become neglectable. The mathematical ML model describes the current through the cell membrane as

$$I(t) = C_m \dot{v}_m(t) + \overbrace{\bar{g}_{Ca^{2+}} M_\infty(v_m(t))(v_m(t) - E_{Ca^{2+}})}^{I_{Ca^{2+}}(t)} + \overbrace{\bar{g}_{K^+} N(t)(v_m(t) - E_{K^+})}^{I_{K^+}(t)} + \overbrace{\bar{g}_l(v_m(t) - E_l)}^{I_l(t)}, \tag{1.8a}$$
$$\dot{N}(t) = \frac{N_\infty(v_m(t)) - N(t)}{\tau_N(v_m(t))}, \tag{1.8b}$$

where $\bar{g}_{Ca^{2+}} \in \mathbb{R}_+$ is the conductivity of the calcium channel and $E_{Ca^{2+}} \in \mathbb{R}$ the Nernst potential. The functions $M_\infty(v_m(t)) \in [0, 1]$, $N_\infty(v_m(t)) \in [0, 1]$, and $\tau_N(v_m(t)) \in [0, 1]$ are only dependent on $v_m(t)$. The reduced system has two state variables: $v_m(t)$ and $N(t)$, which represent the membrane voltage and a recovery variable [37].

Next, *Rho and Prescott* made adaptions to the ML model such that it captured SO and ED [25]. They modified the functions which describe $M_\infty(v_m(t))$, $N_\infty(v_m(t))$ and $\tau_N(v_m(t))$ and added a weak noise term to Equation (1.8a). This noise approximates the effect of stochastic channel opening. The extended ML model became

$$I(t) = C_m \dot{v}_m(t) + I_{Ca^{2+}}(t) + I_{K^+}(t) + I_l(t) + n(t), \tag{1.9}$$

where $n(t) \sim \mathcal{N}(0, \sigma^2)$ represents an *additive white Gaussian noise* (AWGN) source with $\sigma = 20\,\text{mV}$. We refer to Appendix A.1.2 for further details on the ML model. In Figure 1.3, SO and ED for different inputs are shown using the model from Equation (1.9).

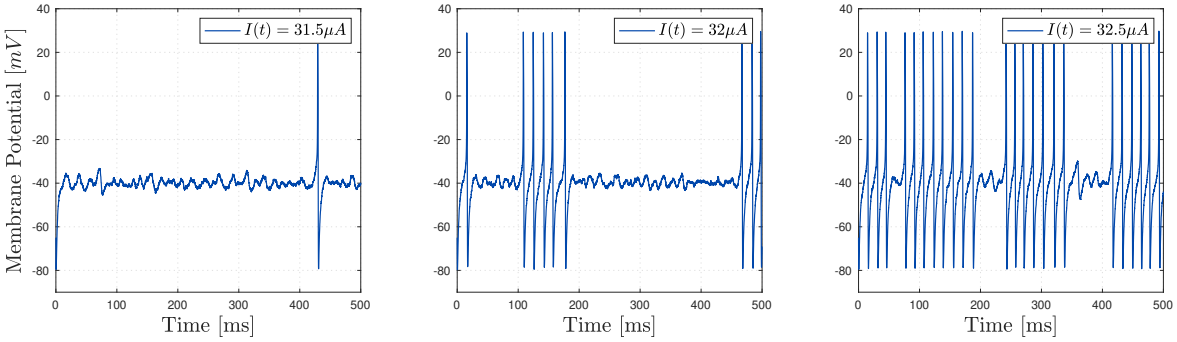

Figure 1.3: Different responses (i.e., outputs captured by $v_m(t)$) upon different stimulation inputs $I(t)$ to the extended ML model described by Equation (1.9).

1.2.3.3 Map-based model

The mathematical HH and ML models were based on neurophysiological principles. However, SO and ED can also be modeled by neglecting the dynamics of the individual ion channels, and by only describing the membrane potential patterns. This is called a *phenomenological modeling approach*. A *map-based* (MB) model captures the dynamical properties of a neuron, without modeling specific ion channels [38]. The basis of a MB model entails the following dynamics

$$x_{k+1} = f(x_k), \tag{1.10}$$

$$\text{where } f(x_k) = \begin{cases} v(x_k) & \text{if } x_k < \theta, \\ v_s & \text{if } \theta < x_k < v_s, \\ v_{reset} & \text{if } x_k \geq v_s, \end{cases}$$

with $x_k \in \mathbb{R}$ representing the membrane potential in mV at time $k \in \mathbb{Z}_+$ and $\theta \in \mathbb{R}$ representing the firing threshold of a neuron. The spike voltage is indicated by $v_s \in \mathbb{R}$, the membrane voltage after a spike by $v_{reset} \in \mathbb{R}$ and $v(x_k) : \mathbb{R} \to \mathbb{R}$ can be an arbitrary function to shape the AP. This model is defined in discrete time steps k, thus without having a unit as 'ms'.

The standard MB model appeared to be incapable of including SO and ED. In order to exhibit SO and ED, *Shilnikov and Rulkov* extended the MB model by introducing an additional state. By doing so the model became

$$x_{k+1} = f_\alpha(x_k, y_k + \beta) + \zeta_k, \tag{1.11a}$$

$$y_{k+1} = y_k - \mu(x_k + 1 - \sigma), \tag{1.11b}$$

where $x_k \in \mathbb{R}$ represents the membrane potential and $y_k \in \mathbb{R}$ an arbitrary state that can turn the spike generator on or off [26]. The (dimensionless) injected current is modeled by $\sigma \in \mathbb{R}$, $\alpha, \beta \in \mathbb{R}$ are arbitrary tuning parameters and $0 < \mu \ll 1$ is the coupling parameter of both states. They assumed that noise influences the spiking behavior of a neuron. This noise was modeled by an AWGN source, i.e., $\zeta_k \sim \mathcal{N}(0, s^2)$. A piecewise continuous function was defined for $f_\alpha(x_k, y_k + \beta) : \mathbb{R} \times \mathbb{R} \to \mathbb{R}$. For further details see Appendix A.1.3.

The AWGN source, modeled by ζ_k, randomly shifts x_{k+1}, which will constantly move the stable point of the system. In the time domain, this resulted in SO. If stable points are absent, they will appear as ED in the time domain. Figure 1.4 illustrates the MB model for $\sigma \in \{-0.005, -0.001, 0.001\}$.

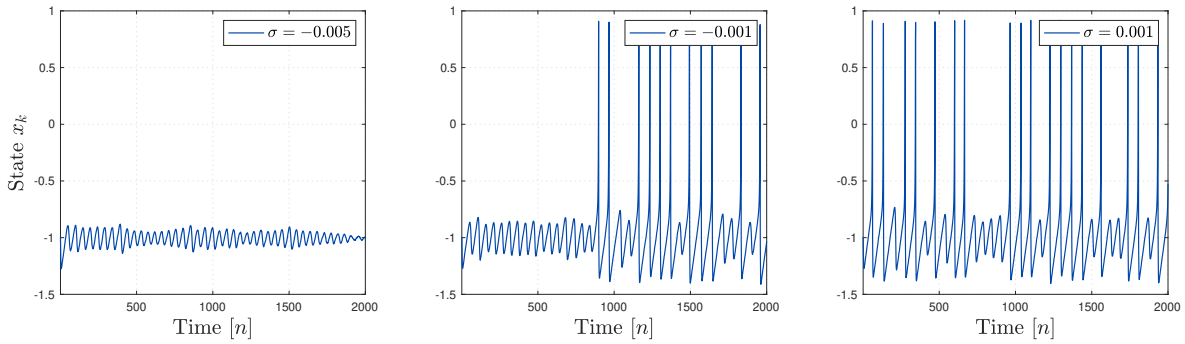

Figure 1.4: Different responses (i.e., outputs captured by x_k) upon different stimulation inputs σ to the extended MB model described by Equation (1.11a) and (1.11b).

1.2.4 Dynamical system-based feedback control

In an open-loop system, the input of a system does not change upon the system's output. Simply speaking, in the case of ENS for NP, the applied stimulus is independent of the presence of SO and ED. If the opposite occurs, then we have a closed-loop system, which is also called *feedback control*. The dependency can be defined such that the system will achieve a certain objective. The goal of feedback control is to find an input signal which steers the state from its initial state $x(0) = x_{init} \in \mathbb{R}^n$ to a destination state $x(T) = x_{des} \in \mathbb{R}^n$ at destination time $T \in \mathbb{R}_+$ by adapting $u(t) \in \mathbb{R}^{n_u}$ for $t \in [0, T]$, and for a desirable sequence of instances of T. In our case, the input signal should be an electrical stimulus that will steer the state away from causing NP by inhibiting SO and ED. Thus, we aim to establish a control scheme to find an input $u(t) \equiv u(0), \ldots, u(T)$ that suppresses SO and ED. To this end, we leveraged one type of control scheme, namely *Model Predictive Control* (MPC), to find $u(t)$.

1.2.4.1 Model Predictive Control

A control strategy was used to steer the output of a process to a specific objective while satisfying a set of constraints on the state and the input. These constraints may represent hardware limitations or patient safety requirements (e.g., limiting the maximum stimulus current to prevent tissue damage). MPC uses the system's mathematical model to predict how the output of a process will respond to an arbitrary input. For a specific time horizon, called the *prediction horizon* P, the MPC solves an optimization problem to find an input sequence that steers the state towards the specified goal. After solving the optimization problem, a subsection of the prediction horizon (the *control horizon* M) is applied to the process. Repeating this process at a regular sampling time interval results in *closed-loop* feedback.

Since control devices are often digital, we require DT models and controller types. Therefore, all the models defined in CT were cast as DT systems; see [34] for further details.

To steer the state towards a certain goal, we pursue to make the states within the prediction horizon (x_{k+j} for $j = 1, 2, \ldots, P$) look like the predefined reference r_{k+j} for $j = 1, 2, \ldots, P$ by adapting u_{k+j} for $j = 0, 1, \ldots, P-1$. An optimization function can be defined that penalizes any difference between the future states within the prediction horizon and the predefined reference using a weight matrix Q. Moreover, to limit large fluctuations on the input u_{k+j} for $j = 0, 1, \ldots, P-1$, the input can be penalized using a weight matrix R.

In mathematical terms, in the discretized MPC framework, the goal is to find an optimal control input u^*_{k+j} for $j = 0, 1, \ldots, P-1$ that minimizes the quadratic cost function of the form

$$\begin{aligned} &\text{(cost function)} \quad \underset{u_k,\ldots,u_{k+P-1}}{\text{minimize}} \quad \mathbb{E}\left\{ \sum_{j=1}^{P} \|x_{k+j} - r_{k+j}\|^2_{Q_{k+j}} + \sum_{j=0}^{P-1} \|u_{k+j}\|^2_{R_{k+j}} \right\} \\ &\text{(constraints)} \quad \text{subject to} \quad x_k = \text{observed or estimated current state}, \\ &\qquad\qquad\qquad\qquad\quad x_{k+j+1} = f(k+j, x_{k+j}, u_{k+j}), \quad j = 0, 1, \ldots, P-1, \\ &\qquad\qquad\qquad\qquad\quad \text{other linear constraints on } x_{k+1}, \ldots, x_{k+P}, u_k, \ldots, u_{k+P-1}, \end{aligned} \tag{1.12}$$

where $\|x_{k+j} - r_{k+j}\|^2_{Q_{k+j}} = (x_{k+j} - r_{k+j})^\intercal Q_{k+j}(x_{k+j} - r_{k+j})$ and $\|u_{k+j}\|^2_{R_{k+j}} = (u_{k+j})^\intercal R_{k+j}(u_{k+j})$. Furthermore, $Q_{k+1}, \ldots, Q_{k+P} \in \mathbb{R}^{n \times n}$ and $R_k, \ldots, R_{k+P-1} \in \mathbb{R}^{n_u \times n_u}$ are given positive semidefinite matrices

representing a weight, penalizing state deviations or large input changes, respectively [39]. The prediction horizon is indicated by P.

Spontaneous neuroma discharge is difficult to capture with state-space models and often results in highly nonlinear models, see Section 1.2.3 for the extended HH model, the extended ML model, and the map-based model. In addition, the models can only predict the system's evolution accurately for a small time interval. Furthermore, using the presented (highly nonlinear) mathematical neuroma models within the MPC resulted in computationally intensive optimization problems that could not be solved within the sampling time of simple hardware (e.g., implantable stimulation devices).

Therefore, we propose to leverage a class of parametric mathematical models with few interpretable parameters, that can serve as a proxy for rather complex mathematical models. These proxies do not show the same behavior as the well-known models. Nevertheless, they capture key statistical properties, making them useful within the MPC scheme, while overcoming difficulties with computationally intensive optimization problems. We will discuss these models in further detail in Section 1.2.4.2 before we incorporate them into our proposed control scheme described in Section 1.2.4.3.

1.2.4.2 Fractional-order systems

Neurophysiological processes often poses properties (regarding the current state of these processes) which show a non-negligible dependence on several past states. These properties could be sufficient to create a mathematical model which may serve as a proxy for the (complex) well-established neuroma models. Therefore, we introduce a *fractional-order system* (FOS)

$$\Delta^{\alpha}\hat{x}_{k+1} = A\hat{x}_k + Bu_k + B_k^w w_k, \quad \hat{x}_0 = 0, \tag{1.13}$$

where $\hat{x}_k \in \mathbb{R}^n$ represents the state vector of the FOS, $A \in \mathbb{R}^{n\times n}$ is the state coupling matrix and $\alpha \in \mathbb{R}_+^n$ the vector of *fractional-order coefficients*. Here, w_k denotes an AWGN vector following an $\mathcal{N}(0,\Sigma)$ distribution (where $\Sigma \in \mathbb{R}^{n\times n}$ represents the covariance matrix) that is scaled by matrix B_k^w with appropriate dimensions. The input to the system is given by $u_k \in \mathbb{R}^{n_u}$, and matrix $B \in \mathbb{R}^{n\times n_u}$ is a scaling matrix that describes how the stimuli are provided to different states and these are referred to as the *input matrix*.

To illustrate the non-negligible dependency in time of neuroma dynamics upon the past states, the sample autocorrelation function for the extended ML model is provided in Figure 1.5. This function is decaying slowly with non-negligible values for increasing lags. This suggests that the system has an *intrinsic long-range memory* which is often modeled well with fractional systems [40, 41]. As such, the statistical properties of the highly nonlinear models are captured by a linear FOS by determination of the fractional-order coefficients [42, 43].

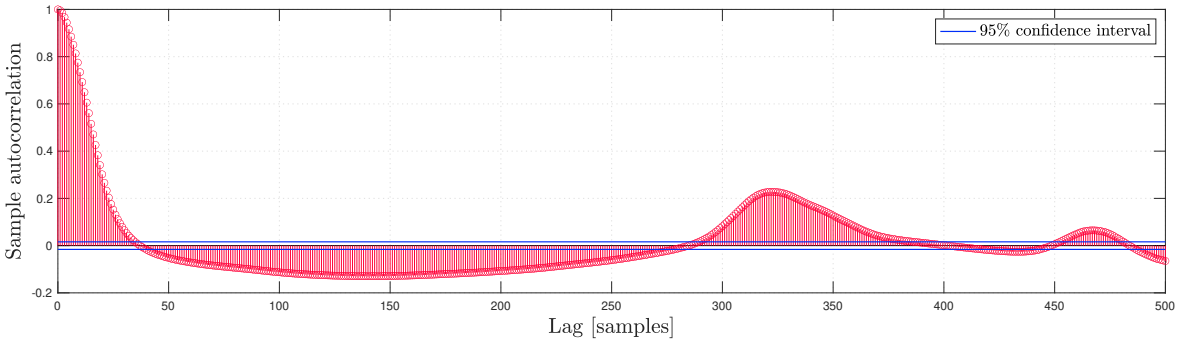

Figure 1.5: Sample autocorrelation of the extended ML model. This figure illustrates that the system has significant intrinsic long-range memory.

These FOSs can be used within the MPC framework to retrieve an input that regulates the FOS and, simultaneously, informative to regulate the real model. Simply speaking, we can use $\hat{x}_k$ (i.e., the state estimate using linear FOS) instead of x_k (i.e., the state of the nonlinear system describing the true mathematical model) within the MPC scheme.

1.2.4.3 Proposed dynamical system-based feedback control scheme

In Figure 1.6, we show our applied methodology. First, we used *system identification* (SI) to find the parameters of a FOS using one of the (detailed) mathematical models presented in Section 1.2.3. Next, we defined the cost function and constraints for the MPC as specified by Equation (1.12) by using the obtained FOS instead of the real model. Therefore, we adjusted the third line of Equation (1.12) to

$$\Delta^{\alpha}\hat{x}_{k+j+1} = A_{k+j}\hat{x}_{k+j} + B_{k+j}u_{k+j}, \quad j = 0, 1, ..., P-1. \tag{1.14}$$

Within the optimization objective, we penalized the error $e_{k+1}, ..., e_{k+P}$ between reference $r_{k+1}, ..., r_{k+P}$ and the predicted future states of the FOS $\hat{x}_{k+1}, ..., \hat{x}_{k+P}$. After solving the optimization problem for the prediction horizon P, we applied the derived optimal inputs $u_k^*, u_{k+1}^* ..., u_{k+M-1}^*$ to the FOS and the real mathematical model for the control horizon M to update k with $k + M - 1$. We used a state estimator – more specific a Kalman filter – to update the states of the FOS $\hat{x}_{k+1}, ..., \hat{x}_{k+P}$ by using the real mathematical model's output $x_{k+1}, ..., x_{k+P}$. In this way, state estimates of the FOS were derived using real mathematical model's input and output. Thereafter, we solved the optimization problem again for the next time step k to find the optimal inputs $u_k^*, u_{k+1}^* ..., u_{k+M-1}^*$ for the subsequent control horizon M.

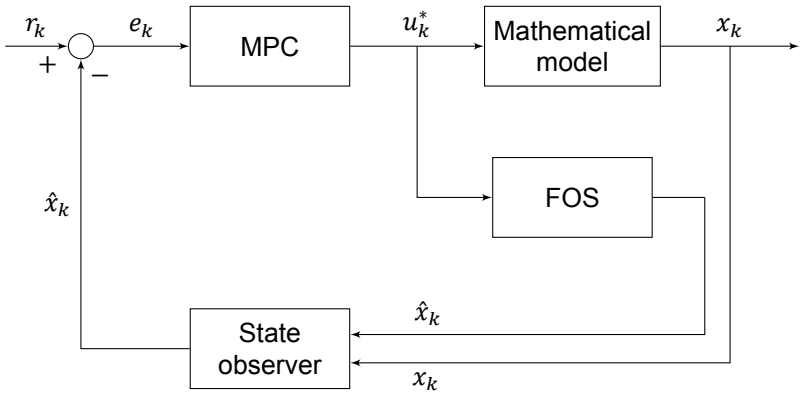

Figure 1.6: Our proposed dynamical system-based feedback control scheme. The reference is indicated by r_k, the state vector of the FOS by $\hat{x}_k$, and the state vector of one of the well-known mathematical models by x_k. We used a Kalman filter as a state observer to update $\hat{x}_k$, using x_k such that the state estimates of the FOS are derived using the real mathematical model's input and output. The error e_k between the reference and state vector of the FOS was used within the MPC scheme to find an optimal input u_k^*.

1.3 Simulation results

In the following, we will show the results of the application of our proposed feedback. We used the fractional-order MPC as a proxy for the three well-established mathematical models in the context of mitigating the SO and ED described above. Notice that the FOS in Equation (1.13) is described by scalar parameters A and α.

1.3.1 Extended Hodgkin-Huxley model

1.3.1.1 System identification from the model

To utilize A and α of the FOS in Equation (1.13), we simulated the extended HH model for 2500 ms – sampled at 100 kHz with a stimulation current of 0.5 µA. Using these parameters, SO and ED could clearly be identified. Lowering the stimulation current will diminish the SO and ED, while lowering the sampling frequency results in incorrectly shaped APs. We created a subsection from the data between 750 and 900 ms and by using the method as in [42], we obtained $A = -0.0098$ and $\alpha = 1.1532$. Any interval could be chosen for the subsection, as long as it contains some SO and ED. Furthermore, we assumed that $B = 1$.

1.3.1.2 An MPC with fractional-dynamics proxy approach

We created a predictive model using a ($p = 15$)-step (0.15 ms) approximation of the FOS plant, with a ($P = 20$)-step (0.5 ms) prediction horizon and a ($M = 10$)-step (0.2 ms) control horizon. These values were chosen to create a predictive model that takes into account the non-negligible dependency of the last 15 steps and uses this dependency to predict the system's next 20 future outputs. Increasing these values results in more computational problems, while a decrease could lead to a predictive model that captures too few statistical properties of the real neuroma model.

We have set the reference to achieve a membrane potential of −57 mV. In this range, the SO and ED should be inhibited. The predictive model was used within the MPC framework as shown in Equation (1.12). We defined $Q_k = I_n$ and $R_k = I_{n_u}$ to penalize the importance of the membrane voltage and for overly aggressive stimulation. The safety constraints for the stimulation current were implemented as $-5 \leq u_k \leq 5$. We applied the obtained inputs to the FOS and to the HH model; a Kalman state estimator with disturbance and noise covariance data $Q = 1$ and $R = 1$, respectively, was used to update the states of the FOS using the outputs of the HH model.

The results are presented in Figure 1.7: the open-loop response (red curve) contains SO and ED, while the closed-loop response (blue curve) does not show this behavior within the controller active interval. These results indicate that it is possible to find pulse-shaped stimuli that suppress SO and ED with our proposed dynamical system-based feedback control scheme.

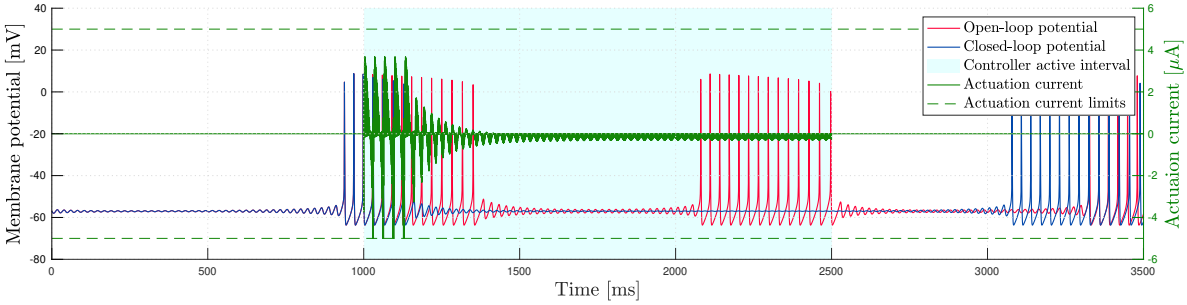

Figure 1.7: An MPC with a fractional-dynamics proxy approach applied to the extended HH model. The red curve shows the open-loop response (without any feedback). We created a predictive model using a ($p = 15$)-step (0.15 ms) approximation of the FOS plant, with a ($P = 20$)-step (0.5 ms) prediction horizon and a ($M = 10$)-step (0.2 ms) control horizon. The simulation results are represented by the blue curve. The reference for the membrane potential was −57 mV. The controller was active between 1000 and 2500 ms. The green curve indicates the applied stimulation current.

1.3.2 Extended Morris-Lecar model

1.3.2.1 System identification from the model

The extended ML model was sampled at 20 kHz and simulated for 800 ms, while the applied stimulation current was 32 µA to obtain SO and ED. The required stimulation current was much higher than the current applied to the extended HH model. We will further address these findings in the discussion. We used the interval between 375 and 400 ms as input signal for system identification of the FOS. However, any interval should suffice, as long as it contains SO and ED. Using the method proposed in [42], we obtained $A = -0.01$ and $\alpha = 1.1502$. Thereby, we assumed that $B = 1$.

1.3.2.2 An MPC with fractional-dynamics proxy approach

For this model, we created a predictive model with a ($p = 15$)-step (0.75 ms) approximation of the FOS plant, a ($P = 20$)-step (1 ms) prediction horizon and a ($M = 10$)-step (0.5 ms) control horizon. To inhibit SO and ED, we set the membrane potential's reference at −40 mV, which equals the equilibrium potential of this model if the stimulation current equals 0. The membrane voltage and overly aggressive stimulation were penalized with $Q_k = I_n$ and $R_k = I_{n_u}$. The safety constraints for the stimulation current were set as $-5 \leq u_k \leq 5$. A Kalman state estimator with disturbance and noise covariance data $Q = 1$ and $R = 1$, respectively, was implemented to update the FOS states using the ML model's outputs. Figure 1.8 shows the results of this simulation. With this strategy, the SO and ED were also inhibited.

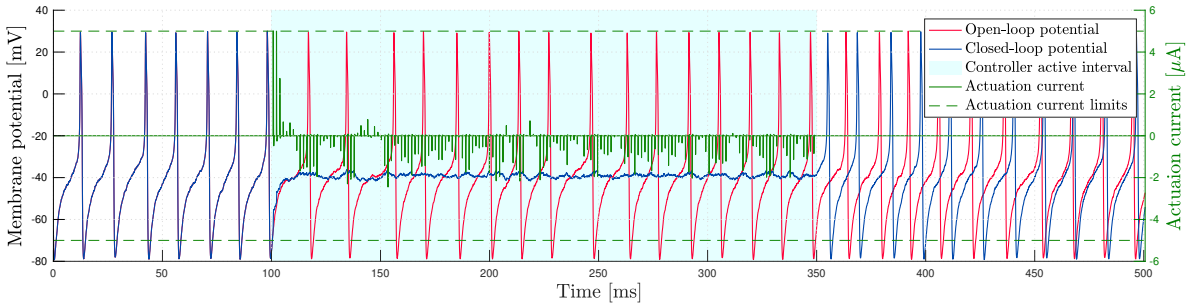

Figure 1.8: An MPC with a fractional-dynamics proxy approach applied to the extended ML model. The open-loop response is given by the red curve. The predictive model was a ($p = 15$)-step (0.75 ms) approximation of the FOS plant, using a ($P = 20$)-step (1 ms) prediction horizon and a ($M = 10$)-step (0.5 ms) control horizon. The response is shown by the blue curve. The reference for the membrane potential was −40 mV. Suppression of SO and ED could be observed within the controller active interval (between 100 and 350 ms). The green curve indicates the applied stimulation current.

1.3.3 Extended map-based model

1.3.3.1 System identification from the model

The extended HH and ML models are based on neurophysiological principles. The extended MB model is a phenomenological model that describes SO and ED patterns, only based on arbitrary time and membrane potential units. The FOS described in Equation (1.13) was identified using a simulation (with $\sigma = -0.001$) of the MB model for 2000 time steps, where the subsection between time step number 1 and 1550 was used to perform SI. We obtained $A = 1.0131$ and $\alpha = -0.0083$, and assumed furthermore that $B = 1$.

1.3.3.2 An MPC with fractional-dynamics proxy approach

The predictive model that we created was based on a ($p = 15$)-step approximation of the FOS plant, a ($P = 50$)-step prediction horizon, and a ($M = 10$)-step control horizon being arbitrary time units. Noise ζ_k in the MB model initiates SO and ED by constantly moving or canceling the model's stable point. For further details, we refer to Appendix A.1.3.

To inhibit SO and ED, we aimed to steer the state in a direction such that ζ_k had less effect on the model's behavior. By pushing the stable point towards $x_n \leq -1.5$, noise ζ_k still resulted in SO, without any ED. Therefore, we defined the state reference at -1.5, although this state value can never be reached due to the system characteristics. We completed our strategy by penalizing the membrane voltage and overly aggressive stimulation with $Q_k = I_n$ and $R_k = I_{n_u}$. To limit the stimulation current, we set $-0.5 \leq u_k \leq 0.5$. Due to the arbitrary units of the stimulation current, these saturation limits are smaller than applied to the two models described above. Again, we used a Kalman state estimator with disturbance and noise covariance data $Q = 1$ and $R = 1$, respectively, to update the states of the FOS. The results show SO and ED suppression (Figure 1.9). Note the arbitrary *x-axis* and *y-axis* units: this model does not describe the membrane potential in mV nor the stimulation current in µA. Note also that the reference state value of -1.5 was never reached.

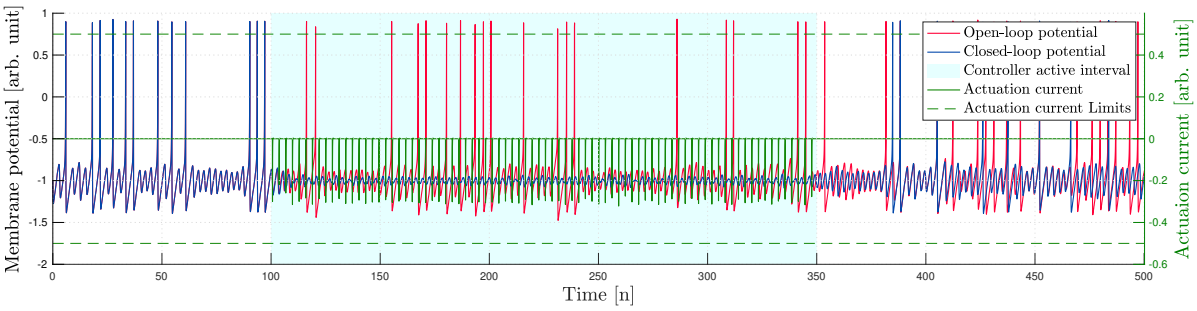

Figure 1.9: An MPC with a fractional-dynamics proxy approach was applied to the extended MB model. The open-loop response is illustrated by the red curve. This model is a phenomenological model. The time scale and membrane potential have arbitrary units. The predictive model was a (p = 15)-step approximation of the FOS plant, with a (P = 20)-step prediction horizon and a (M = 10)-step control horizon. The reference for the membrane potential was −1.5, and the red curve shows the closed-loop response. Within the controller active interval (between 100 and 350), suppression of SO and ED could be observed. The green curve represents the applied stimulation current.

1.4 Discussion

1.4.1 Mitigating neuropathic pain

Currently, NP is regarded as being caused by the firing of neurons in a neuroma, which in turn leads to SO and ED. Theoretically, by neutralizing SO and ED, it should be possible to mitigate the generation of NP. To capture SO and ED formation, three models were proposed: an extended HH model [24], an extended ML model [25], and an extended MB model [26]. The underlying elements in the three mathematical neuroma models of SO and ED are different.

The extended HH and ML models describe the ion channels in the cell membrane. Where the HH model is based on sodium, potassium, and leak channels, the ML is based on calcium, potassium, and leak channels. Both models can capture similar membrane potential patterns, despite the different characteristics between sodium and calcium channels. Interestingly, the stimulation current required to obtain a similar input-output response for the ML model, when compared to the HH model, differs by a factor of 64, while they both model SO and ED. This is important while implementing the control strategy *in-vivo* in the future: stimulation amplitude scaling may be required to obtain the correct behavior.

The extended MB model is based on a phenomenological modeling approach, bypassing the properties and function of different ion channels in the cell membrane. This model focuses on capturing similar patterns as the HH and ML models. As a result, the time scale, the output, and the stimulation 'current' have arbitrary units. This makes it difficult to compare the output 'voltages' and stimulation 'currents' of the MB model to the HH and ML models. Although the MB model is not based on any biological cell membrane characteristics, our proposed dynamical system-based feedback control scheme shows outstanding results in terms of SO and ED suppression.

These models are highly nonlinear. In order to avoid the usage of a model of great complexities within the MPC framework, we used a FOS and showed that it could capture the statistical properties of the three well-known neuroma models. By regulating the FOS, our results (see Section 1.3, and corresponding Figure 1.7, Figure 1.8, and Figure 1.9, respectively) imply that it is possible to regulate the real neuroma model. In all simulations, the obtained input to suppress SO and ED resembled pulse-shaped patterns.

Our results suggest that the proposed scheme enables a data-driven real-time approach to neutralize SO and ED. These results may contribute to the development of ENS systems to mitigate NP. Furthermore, the variability in the stimulation patterns observed can equip us with a mechanism to solve problems related to lead migration, habituation, and fluctuating pain experience. We envisage that a closed-loop strategy will prevent over- and under-stimulation and, therefore, reduce the need for painkillers and enhance the individual's quality of life in the long term. Data-driven real-time ENS possesses the potential to treat NP caused by neuromas and different sources with similar phenomenological characteristics.

1.4.2 Computational implementation remarks

One of the disadvantages of using the well-established neuroma models for MPC is that it can become too computationally intensive to implement on (simple) stimulation hardware. Therefore, we used a FOS as a proxy for the ground truth mathematical model and provided evidence that this could be a feasible and computationally efficient alternative for the well-established models. However, one could argue that this approach still results in computationally intensive optimization problems, while a linear model, one that only uses the last state to determine the current one, would be sufficient as well. Hence, we performed simulations using a truncation that boils down to a linear model approximation (i.e., with $p = 1$). These simulation results lead to the conclusion that it might not be possible to attain the desired goal. For further details see Appendix A.2.

1.4.3 State-of-the-art versus proposed control

ENS technology is already applied in neuropathic pain treatment, but the level of pain reduction is generally not sufficient and side effects are frequently present. Open-loop and closed-loop stimulators are available to treat the symptoms of neuropathic pain [17, 31]. These stimulators target the spinal cord or the DRG. A rate of stimulus pulses is applied, and the patient experiences a constantly present (non-painful) tingling that masks the pain. The closed-loop stimulator of *Saluda Medical* monitors the tissue level activation (e.g., the result of summation of many action potentials) at the spinal cord and aims to keep this level constant by adapting the stimulator's intensity [31]. By doing so, the stimulator

is able to compensate for lead dislocation and movement of the spinal cord, which is one of the disadvantages of ENS. However, the effectiveness of the treatment – the *percentage pain relief* (PPR) – is not monitored. Furthermore, the system does not recognize any fluctuations in the experienced level of pain or pain habituation, and therefore, it does not compensate for these shifts.

We focused on ENS application at the level of the peripheral nerve and explored the possibilities to suppress ED and SO on a single-axon level. The advantage of stimulation at the peripheral nerve level is, that it is less invasive than spinal cord stimulation in terms of the implantation of electrodes. Additionally, it might provide stimulation of a targeted area relate to the painful nerve, rather than involving stimulation of an entire region, which is actually larger than the painful area. To distinguish the effect of open-loop stimulation on the suppression of SO and ED, we also applied biphasic pulses, comparable to stimulation patterns currently in use. In Appendix A.3, we show the results for an open-loop strategy where the *pulse width* (PW) of the anodic and cathodic phase of the biphasic pulses equals 250 µs. The pulses were applied with a frequency of 50 Hz and amplitude 2 µA. We observed that in the open-loop strategy using biphasic pulses, the SO and ED were not suppressed. Application of anodic non-biphasic pulses (PW 250 µs and amplitude 2 µA at 500 Hz) showed similar results. However, application of cathodic non-biphasic pulses (PW 250 µs and amplitude -2 µA at 500 Hz) resulted in improved outcomes in terms of SO and ED suppression. Thus, with an open-loop strategy using non-biphasic pulses, suppression of SO and ED appears to be possible. In our experience, this holds for specific patterns that can only be found by trial-and-error. An advantage of the closed-loop strategy is that continuous application of stimulation pulses is not necessary. In contrast, in the open-loop strategy, continuous application of stimulation pulses takes place, even when SO or ED are not present. Thus, the proposed strategies can lead to a significant battery performance increase.

1.4.4 Implications for real-time neurostimulation

During the *in-silico* experiments, our proposed dynamical system-based feedback control scheme resulted in arbitrarily shaped stimulation pulses that could inhibit SO and ED. The next step needs to be the implementation of our proposed control scheme in a real-time *in-vitro* setup to verify the results on DRG neurons. However, the currently available stimulation hardware is not capable of implementing such arbitrarily shaped stimulation pulses.

The total energy that is transferred during a single constant current stimulation pulse is expressed by the charge $Q = I_{stim} t_{pulse}$, where $I_{stim} \in \mathbb{R}$ is the constant stimulation current and $t_{pulse} \in \mathbb{R}_+$ the pulse duration. State-of-the-art stimulators often implement charge-balanced biphasic stimulation pulses, in other words, after a stimulation pulse $Q = 0$. Charge balancing is required to prevent electrolysis with electrode dissolution and tissue destruction [44]. We added this charge balancing constraint and a biphasic pulse constraint to our MPC strategy to simulate the prevention of electrolysis while SO and ED should be suppressed. The results suggest that the SO and ED could not be inhibited in this situation. In this respect, we refer to Appendix A.4. It is questionable whether these mathematical models can be used in combination with a charge balancing constraint. Injecting and removing the same amount of current could create an altered cellular response *in-vivo*, while these models do not capture this behavior *in-silico*.

After taking a closer look at the stimulation patterns (e.g., Figure 1.8, the actuation current shown in green), it becomes clear that the applied stimulation pulses become mainly negative after some time. This indicates that a particular charge is constantly removed from the cell. During simulations, we applied a continuous positive stimulation current to initiate SO and ED. Our MPC strategy will eventually try to cancel out this additional artificial stimulation current to inhibit SO and ED, and the applied stimulation pulses will be, therefore, mainly negative. However, in an *in-vivo* setup, this non-balanced stimulus could lead to electrolysis.

We assumed that the strength-duration relationship for a stimulation equals $Q = I_{stim} t_{pulse}$. The strength-duration curve relates the intensity of a stimulus (required to activate a neuron) to its duration [45]. A lower stimulation current would require a longer duration to activate the neuron. However, this does not hold for all $t_{pulse} \in \mathbb{R}_+$. For a neuronal membrane, if $t_{pulse} \to \infty$, the minimal required current to create an AP equals the rheobase current, $I_{rheobase}$ [45, 46]. During extracellular current stimulation, the applied current should be higher than a certain lower threshold ($I_{rheobase}$) to create an AP. Recent work showed that an upper threshold might also be possible for specific pulse durations [46]. Increasing the stimulation above this upper threshold does not lead to an altered cellular response. It has been argued that the transferred energy for pulses shorter than polarization time ($t_{pulse} \leq 1$ µs)

becomes constant. Strictly speaking, increasing the stimulation current for high frequency pulses (≥ 1 MHz) does not increase the total transferred charge [46].

We could utilize the strength-duration relationship of a neuronal stimulation in our strategy. Arbitrarily shaped pulses could be applied to inhibit the SO and ED, after which the charge was balanced with a current below the $I_{rheobase}$ to prevent additional induced activity. A different, more aggressive charge balancing method would be by compensating the applied charge by large ultra-high frequency pulses (≥ 1 MHz), such that the total transferred charge to the membrane is less or equal to $I_{stim}t_{pulse}$. These pulses will probably introduce additional activity. This post-stimulation protocol can be included in our strategy, such that the arbitrarily shaped pulses will compensate for this additional activity.

1.4.5 Translation to in-vivo experiments

We considered three well-established mathematical models of neural firing patterns in neuromas. These models capture the behavior of a single-axon. In an *in-vitro* setup, measurements can be performed on, and stimuli can be applied to a single-axon. However, translating this work to *in-vivo* to mitigate NP by measuring and stimulating a peripheral nerve introduces several additional challenges. 1) During *in-vivo* measurements, the SO and ED activity of multiple axons will be measured simultaneously using, e.g., microneurography. This activity is called *compound action potential* (CAP). In the current work, SO and ED are measured on a single-axon level using patch-clamp techniques. Therefore, additional work needs to be done to discriminate the activity of individual axons from CAP recordings. 2) By stimulating a peripheral nerve, the activation field is spread over the nerve, which will affect the membrane potential of many axons. Ideally, the stimulation should be adapted such that SO and ED are suppressed in NP axons and at the same time not affecting the (healthy) axons. 3) Without charge balancing, tissue damage could occur. The strength-duration relationship of a neuronal stimulation is not included in the well-known neuroma models. Including these characteristics could result in stimulation patterns that inhibit SO and ED while having a balanced charge in the tissue after stimulation. 4) We assumed that by suppressing SO and ED, the NP could be mitigated. However, instead of minimizing the ED's rate and the SO's amplitude, different objectives (e.g., a non-constant membrane potential without ED, or having a healthy nerve signal as the reference) can be formulated that could potentially lead to NP decrease as well.

1.5 Conclusion

Subthreshold oscillations (SO) and *ectopic discharges* (ED) generated in neuroma may cause *neuropathic pain* (NP). This pain may be suppressed by electrical neurostimulation. However, current technology using continuous stimulation often proofs insufficient. We proposed a dynamical system-based feedback control scheme for stimulation that uses the key statistical properties of SO and ED. By employing three well-known mathematical neuroma models, we provided evidence *in-silico* that our proposed scheme is capable of neutralizing SO and ED at the single axon level. Our results contribute to the development of electrical neurostimulation systems with which it will be possible to reduce NP significantly.

2

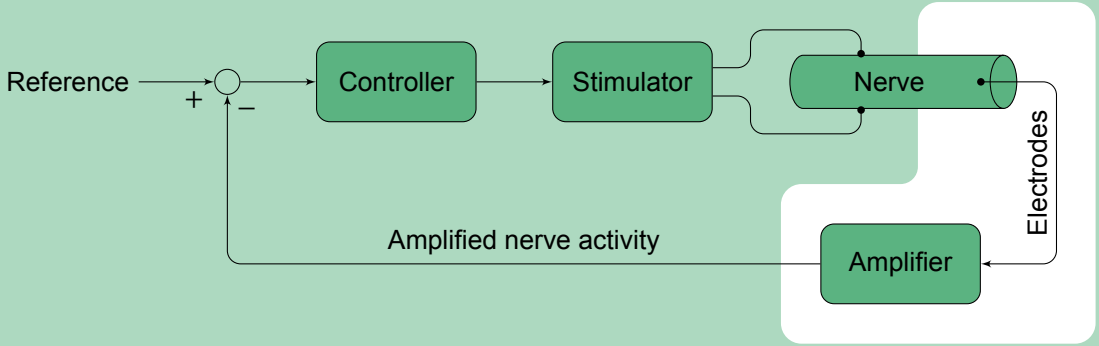
Reference
+
–
Controller
Stimulator
Nerve
Electrodes
Amplified nerve activity
Amplifier

2

Design of an extended neural signal amplifier for microneurography

Objective: To measure nerve action potentials using a setup that embeds expansion capabilities, such as electrical neurostimulators.
Approach: Nerve action potentials are electrical signals generated by the nervous system. They encode information which is generated in the sensory organs of the body, conducted via peripheral nerves to the brain. Thereby, the brain receives signals regarding the status of the internal organs and the outer world. Depending on the type of stimuli and, in particular, those related to pathological processes, these signals can evoke 'pain'. Neural signals which run within the peripheral nerve can be blocked or altered in order to reduce the generation of pain, which is currently done by applying constant electrical stimulation. The pain provoking signals which run through the nerves are commonly not detected and analyzed before electrical stimulation is provided. Constant electrical stimulation is not effective at all moments of the pain experience caused by fluctuations in signal intensity. In addition, the side effect of constant stimulation is the generation of a constant cumbersome sensation in an area which is larger than the original pain area. These shortcomings emphasize the need for improvement by a dedicated setup, capable of measuring this nerve activity, while embedding processing power and extensions for simultaneous stimulation. As the main goal, this setup should amplify and digitize signals from the peripheral nerve, which are in the range of 10 µV, while the bandwidth of interest is between 500 and 5000 Hz. We designed a hardware setup that consists of a preamplifier, a main amplifier, and corresponding software to control the amplifier. Analog band-pass filters, the driven right leg circuit, and shielding techniques were implemented to increase the maximum signal-to-noise ratio. We validated the setup using specifically designed artificial calibration signals. During *in-vivo* experiments, recordings of nerve action potentials were performed in lugworms and in the sciatic nerve of rats.
Main results: The designed setup was capable of measuring nerve action potentials at the level of a single or a few axons. The driven right leg circuit, analog band-pass filter, and shielding implementation fulfilled the hardware requirements.
Significance: The *in-vivo* experiments show that our setup can measure action potentials in peripheral nerves. With this setup, it is potentially possible to detect pain-related activity and discriminate subthreshold oscillations and ectopic discharges that are related to neuropathic pain. Additionally, this setup could implement closed-loop algorithms that require simultaneous neural recording and stimulation.

2.1 Introduction

2.1.1 Nervous system

Scientists and physicians separate the nervous system into two parts. The first part, the *central nervous system* (CNS), contains the brain and the spinal cord. It processes sensory information and controls the activity of the muscles and internal organs of the body. The second part, the *peripheral nervous system* (PNS), contains sensors that continuously monitor the body's state in terms of movement, internal and external environmental changes. Furthermore, the PNS contains nerves that provide for the communication between the CNS and rest of the body. This communication includes sensory information (from the sensors in the PNS) and motor control information (to regulate movements) [47].

The PNS consists of *nerves*, acting as 'information highways' between different parts of the human body. A nerve is composed of axons that are slender projections originating from *neurons*. Neurons are nerve cells that communicate with each other via electrical signals. Different types of neurons can be identified; e.g. *sensory neurons* (respond to external or internal stimuli and transmit their information to the CNS), *motor neurons* (transmit signals from the CNS to the muscles), and *interneurons* (connect different types of neurons in the same region, such that these neurons can communicate with each other) [47].

Figure 2.1a shows the structure of a neuron, the building blocks of nerves. It consists of a cell body, an axon and dendrites. The axon (also called 'fiber') transmits signals away from the neuron cell body and ends at another cell, e.g., another neuron or muscle cell. The axon can be as long as 1 meter, such as the axons that communicate with the muscles in the foot. While axons transmit signals away from the cell body, dendrites conduct signals towards the cell body.

The structure of a nerve is shown in Figure 2.1b. The endoneurium is a connective tissue layer around an individual axon, with several axons combined forming a nerve fascicle. The connective tissue layer around a fascicle is called the perineurium. A nerve can consist of several fascicles, finally surrounded by a connective tissue layer labeled as the epineurium [48]. The different connective tissue layers separate the axons electrically, protect the axons, and help to reduce potential pulling forces on the axons.

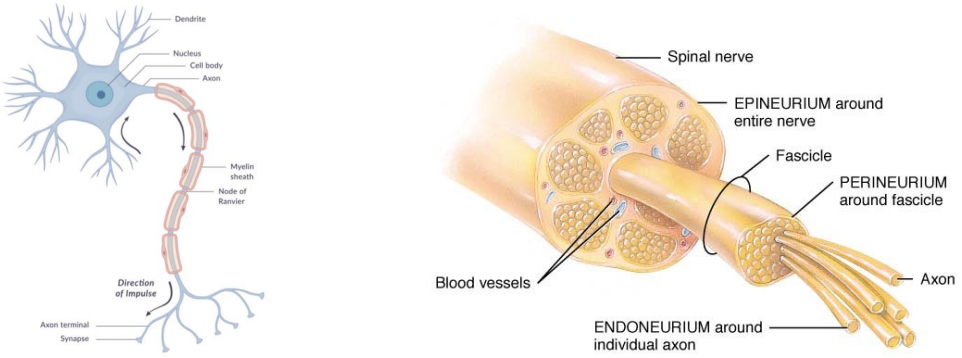

(a) Structure of a single sensory neuron including cell body, axon and dendrites [49].

(b) Structure of a nerve, including the different tissue layers around the axon, fascicle and entire nerve [48].

Figure 2.1: Structure of a neuron and a nerve.

Action potentials (AP) are signals that play a major role in the communication between neurons. An AP is a steep depolarization, repolarization and hyperpolarization of the membrane potential, caused by the disturbance of equilibrium at the cell membrane. We discussed the different ion channels responsible for this equilibrium in Section 1.2.1. The AP can be divided into five phases [50] as we show in Figure 2.2. 1) *Stimulation*: A small stimulus leads to a small depolarization, sodium ions can flow (down the concentration gradient) into the cell. If the membrane potential passes the cell's threshold (often around $-55\,\mathrm{mV}$), the cell will depolarize further. Otherwise, it will fall back to the equilibrium potential. 2) *Rising depolarization*: This increase of membrane potential will further activate other voltage-gated sodium channels, resulting in faster cell depolarization. 3) *Repolarization*: At a specific membrane potential, the voltage-gated sodium channels will close, and potassium voltage-gated ion channels open and potassium ions flow outwards. As a result, the membrane potential will decrease. 4) *Hyperpolarization*: The voltage-gated potassium channels are time delayed and will not close immediately if

the equilibrium membrane reaches the equilibrium potential of −70 mV, causing a hyperpolarization. Sodium channels open to restore equilibrium. 5) *Resting state*: The cell membrane potential is close to the equilibrium potential.

The AP's phases take place at a specific spot at the axon; however, the AP is conducted along an axon. The conductance speed (in m/s) along an axon depends on the degree of myelinization of the axon and its thickness. We can differentiate the axons into two groups: *myelinated* and *unmyelinated* axons [51]. *Schwann cells* cover both nerve axons; however, only on the myelinated axons, the Schwann cells produce a myelin sheath. Myelin is a fatty substance and has a high conductance. The myelin sheath is a noncontinuous isolation sheath around the nerve, which contains gaps (called *nodes of Ranvier*) between parts of sheaths [51]. In a myelinated axon, the AP jumps from node to node, increasing the conduction speed. E.g., unmyelinated C axons are thin (radius 0.5 to 2 µm) and have a conductivity speed of 0.5 to 2 m/s. These axons often carry nociceptive, temperature, and mechanoreception information. In contrast, myelinated $A\delta$ axons are also thin (2 to 5 µm), but have an increased conductivity velocity of 12 to 30 m/s and often carry nociceptive, cold, and touch information. Finally, myelinated $A\beta$ axons are thicker (radius 5 to 12 µm), resulting in a conductance velocity of 30 to 70 m/s. The latter captures touch and pressure information [51], although the involved axon for many types of senses is still unknown. For a complete overview of different axons, see Appendix A.5.

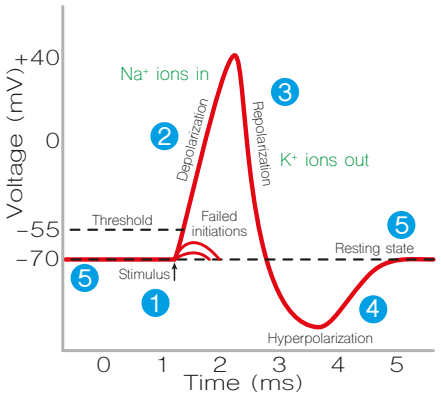

Figure 2.2: The action potential distinguished in several steps [50].

Nerves are built out of various axon types (myelinated, unmyelinated, thick and thin), conducting a mixture of information. Revealing the traffic inside nerves could yield additional information about how the CNS communicates with the different parts of the body. On a single axon level, *patch-clamp techniques* are used to study this traffic [52]. Using these techniques, the intracellular potential of an individual neuron is measured *ex-vivo* or *in-vitro* (for further details see Appendix A.6). However, to expose the nerve activity of single or multiple axons, these techniques are inappropriate. Alternatively, *microneurography* can be used to study *in-vivo* recordings of signals transduced by the axons.

2.1.2 Microneurography

Instead of measuring inside a neuron, nerve activity can be measured near the neuron using an electrode. Depending on the effective electrode area, the electrode will capture the activity (or APs) at the axon transferring sensory or motor information to or from one neuron (*single-unit*) or multiple neurons (*multiple-unit*). The simultaneous activation of many axons in a small space results in *local field potentials* (LFP) [53].

During a microneurographic recording, a physician inserts a small needle of 200 microns (µm) into a nerve bundle, as shown in Figure 2.3a. Figures 2.3b shows the cross-section of a nerve, including the electrode. The electrode is epoxy resin coated to isolate it from surrounding tissue – except the non-isolated part at the tip (the top 30 µm). This way, single-unit measurements of a large fiber, or multiple-unit measurements of multiple smaller fibers are performed. One could also use a non-isolated electrode to record multiple-unit activity from all the axons in the vicinity of the electrode.

Microneurography is performed with respect to surrounding (non-neuron) tissue. For that purpose, a reference electrode (which is a non-isolated electrode) is placed just outside the nerve bundle [55]. By doing so, LFPs fluctuations in the order of 10 µV can be measured. These (bio)potentials are much smaller than the intracellular AP membrane voltages measured by patch-clamp since microneurography is performed outside the neuron. The LFPs cover a large diversity of frequencies, often between 500 and 5000 Hz [56].

Microneurography can be applied to participants that are fully awake. These participants can then be exposed to different sensory stimuli like touch, pin-prick, heat or cold and asked for their sensory experience (e.g., painful, non-painful, cold, warm, touch, and pricking). Depending on the exact electrode location in the nerve, activity from different types of fibers can be recorded. Figure 2.4 shows the different recordings of a myelinated and an unmyelinated axon, where the AP shape differs to a large

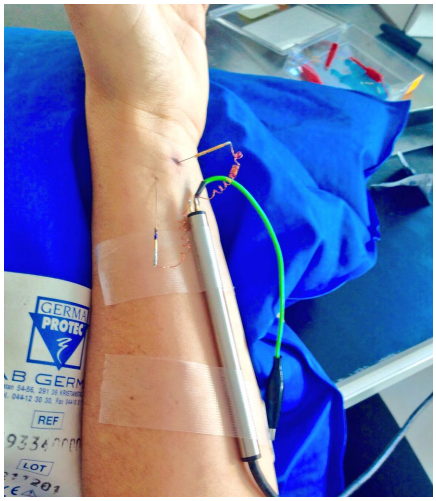

(a) Setup for microneurography with two electrodes, one in the median nerve, the other outside the nerve. The green wire is connected to the skin [54].

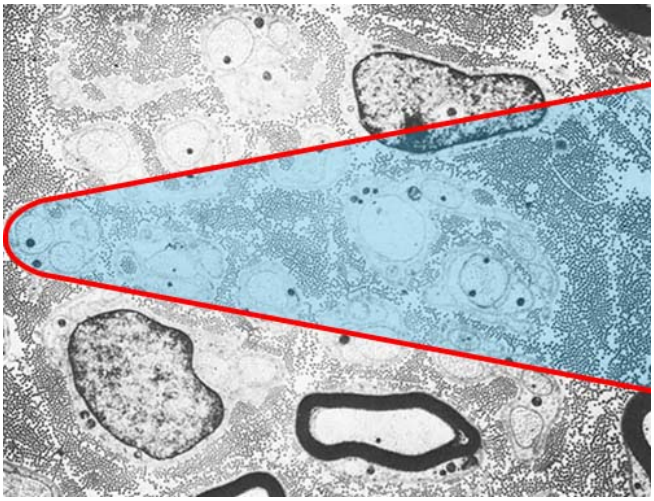

(b) Cross section of human sural nerve. The red cone represents the non-isolated tungsten area of the microneurography electrode, that exceeds 30 µm from the tip. The large cell on the top and bottom left represents a Schwann cell nucleus. The cell with the black edge on the bottom is a small myelinated axon. In between these large structures, a number of unmyelinated axons can be seen [55].

Figure 2.3: Microneurography.

extent. However, the shape of the recorded AP heavily depends on the electrode location in respect to the axon(s). We elaborate on this further in the discussion of this chapter (Section 2.5).

Motor control information and sensory information signals can both be captured using microneurography. Neural activity can however be generated by different sources as well. In Section 1.2.2, we discussed the formation of a neuroma after peripheral nerve injury. This can also generate neural activity that is interpreted by the brain as painful. Capturing these signals yields additional information to improve the treatment of a neuroma. Our goal is to capture signals coming from painful sources, such as neuroma tissue, and compare this to the electrical signals of healthy nervous tissue.

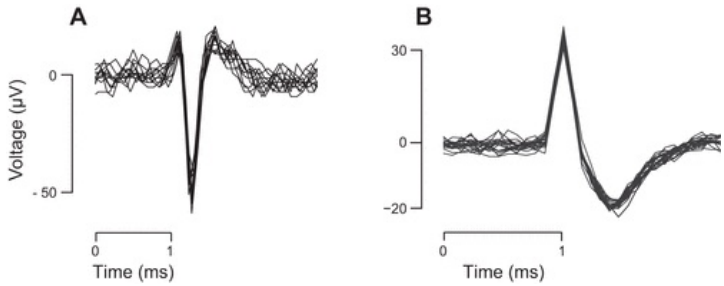

Figure 2.4: Typical contours of nerve impulses in unmyelinated C axons (shown in **A**) and myelinated $A\beta$ axons (shown in **B**) [57].

2.1.3 Interference

When measuring biopotentials, an adequate handling of interferences (a disturbance caused by external sources) is expected. If not handled appropriately, LFPs can not be measured adequately. In the field of bioamplifier designs, electromagnetic inferences are mainly considered.

Electromagnetic interference (EMI) can be generated through man-made (e.g. from electronics) or natural (e.g. lightning) sources. *Powerline interference* (PLI) is an electromagnetic-type interference caused by the powerlines, and is characterized (in Europe) by a 50 Hz signal together with its harmonics. PLI and EMI play a major role in the field of biopotential amplifiers, and have to be taken into account [58].

Disturbances enter the system through a coupling path, e.g., through conductive, capacitive, and inductive coupling. In the case of PLI, a capacitive coupling exists from the powerlines to the electrode leads and the body [59]. Figure 2.5 illustrates these couplings: PLI causes a small current that travels

through the body. This current leads (due to the patient's impedance) to voltages that have different values at different location on the body. Therefore, these couplings result in a voltage difference between the patient and the amplifier common and in an inter-electrode voltage difference. These voltage differences – including the biopotential of interest – appears at the input of the amplifier. Any voltage difference caused by PLI should be ignored by the amplifier to successfully amplify the biopotentials.

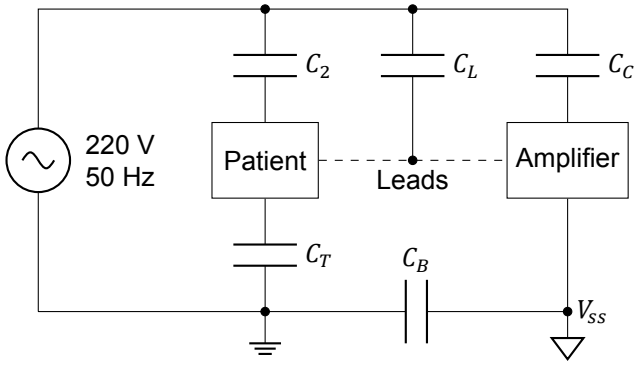

Figure 2.5: EMI is coupled to the system through coupling capacitors C_2 and C_T. It can also be coupled to the leads by capacitor C_L and through the power coupling capacitor C_C. Capacitor C_B is coupled between AC ground and the amplifier's ground. Adapted from [59].

For instance, in case of a differential amplifier, PLI may result in a voltage that appears simultaneously at the inputs, also called *common-mode* (CM) voltage (V_{cm}). Furthermore, a *differential-mode* (DM) voltage (V_{dm}) is present that originates from biopotentials (e.g., neural activity), or at worst, from PLI coupled to the leads. In Figure 2.6 we show a schematic representation of a differential amplifier used to record biopotentials (V_{dm}) through microneurography, where PLI is present (V_{cm}). An ideal amplifier would only amplify the V_{dm} signals (originating from neural activity), without amplifying V_{cm} or V_{dm} caused by PLI. However, in reality, the output of the amplifier is described by

$$V_{out} = A_{dm}(V_+ - V_-) + \frac{1}{2}A_{cm}(V_+ - V_-), \tag{2.1}$$

where A_{dm} represents the DM gain and A_{cm} the CM gain. For an ideal amplifier $A_{dm} \gg A_{cm}$. To quantify this, the *common-mode rejection ratio* (CMRR) is defined as

$$CMRR = 20\log_{10}\left(\frac{A_{cm}}{|A_{cm}|}\right), \tag{2.2}$$

and indicates how much of the common-mode signal will appear on the output. One of the goals in amplifier designs is to maximize the CMRR [58].

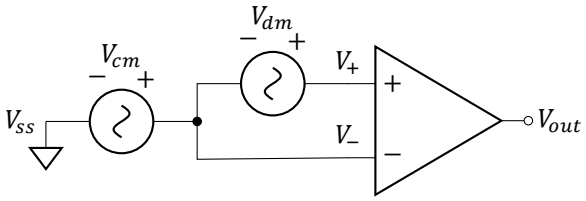

Figure 2.6: Differential mode amplifier setup: V_{dm} represents the biopotential and V_{cm} a voltage offset caused by, e.g., PLI.

Several possibilities are available to limit the effect of EMI on the output of the amplifier. 1) Increase the CMRR of the amplifier, 2) decrease the amplitude of the CM signals V_{cm}, 3) using analog filters, or 4) application of data post-processing techniques such as (digital) filtering. We will elaborate on these techniques more extensively in the system design, Section 2.2.2.

2.1.4 Available hardware for microneurography

Commercially available hardware can be used to perform microneurographic recordings. Figure 2.7 shows the setup supplied by *ADInstruments*, consisting of a neural amplifier (*Neuro Amp EX*), a high

impedance headstage (*Neuro Amp EX Headstage*), and the software for data acquisition and analysis (*LabChart*) [60]. The neural amplifier is a low noise and high gain amplifier, with a bandwidth of 100 Hz to 5 kHz. The headstage has a gain of $A_v = 100\,\mathrm{V/V}$, with a 10 Hz high pass filter, and uses shielding and a *driven right leg* (DRL) circuit to minimize the common mode interference [58]. This will be discussed further in Section 2.2.3.

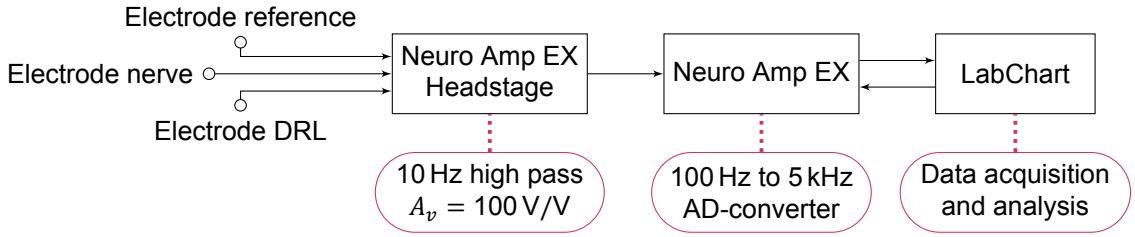

Figure 2.7: *ADInstruments* recording stages for microneurography [60].

This setup is used and recommended in recent microneurographic studies [61, 62]. But although this setup can record neural signals, it cannot be extended with additional hardware, e.g., a neural stimulator or an additional headstage to record at two locations simultaneously. Furthermore, this setup does not contain any embedded processing power that can be used to deploy custom algorithms, e.g., to control the stimulator. These shortcomings emphasize the need for improvement by a dedicated setup, capable of measuring this nerve activity, while embedding processing power and extensions for simultaneous stimulation.

2.1.5 Hardware proposal and requirements for microneurography

Our goal is to design an open-source and low-cost neural signal amplifier platform for microneurography. The amplifier should enable multiple channel recording, while embedding processing power and extensions for simultaneous stimulation. The design includes software at a host that can control our amplifier. We call our proposed design *the extended neural signal amplifier*.

The design meets several requirements to record neural activity while including the extensions for multiple channel recording and simultaneous stimulation. We branched the requirements into hardware and software requirements:

- *Hardware*: Amplify low-level neural signals of 10 µV with a gain of $A_v \approx 20\,000\,\mathrm{V/V}$.
- *Hardware*, *software*: Frequency range of interest is between 500 and 5000 Hz. Filter out other frequencies.
- *Hardware*: Rejection of the 50 Hz harmonic PLI and other EMI.
- *Hardware*, *software*: An analog-to-digital resolution of at least 14-bit.
- *Hardware*, *software*: Digital communication with a host that supports at least 20 000 samples per second.
- *Software*: Real-time data visualization on the host, with hardware control options to adjust the amplifier's gain.
- *Software*: Real-time data processing; store and export recorded data.

2.1.6 Chapter structure

We will discuss the design of the extended neural signal amplifier in several steps. 1) We introduce the global system design, whereafter the different modules will be elucidated in more detail. 2) The system is validated using artificial signals; we compare the validation results with the design specifications. 3) To validate our amplifier on living tissue, we set up *in-vivo* experiments with worms and rats to perform microneurographic recordings. 4) We conclude this chapter with a discussion on our design and future recommendations.

2.2 System design

In the following section, we discuss the design of the extended neural signal amplifier into more detail. First, we show the global system setup and provide some background on filter design. Next, we elaborate on the different modules step-by-step.

2.2.1 Global system design

Similar to the setup of *ADInstruments* for microneurography [60], we will split our design into several modules. Figure 2.8 shows our proposed design, consisting of a preamplifier, main amplifier, and host software.

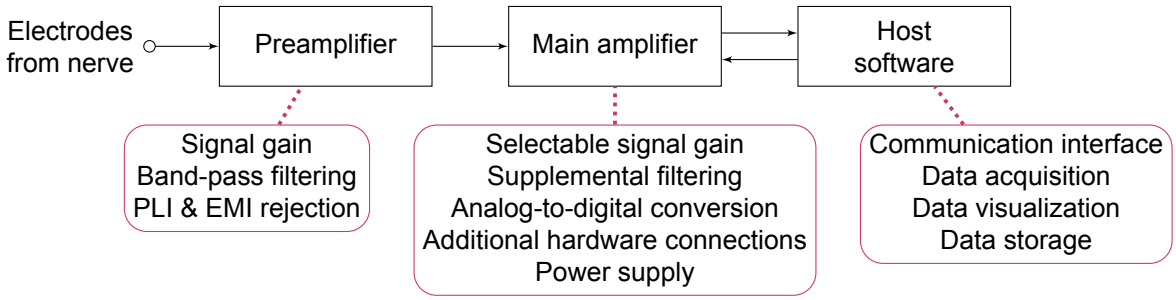

Figure 2.8: Extended neural amplifier, consisting of a preamplifier, main amplifier, and host software.

The preamplifier is the first amplification stage after the nerve electrodes. This amplifier will be situated close to the source (the nerve) to limit external interference. Besides amplification of the frequency range of interest, the preamplifier should limit PLI and EMI. The main amplifier performs further amplification in selectable steps. Besides additional gain, the main amplifier should contain supplemental filtering, an *analog-to-digital converter* (ADC), and include connections for future additional hardware, such as a stimulator. Apart from signal processing, the main amplifier should also generate the supply voltages for the different modules, using the voltage from an external power supply. We complete the setup with a host software that provides a communication interface between the main amplifier and the host. This software will visualize recordings in real-time and control the setup features to improve the user-friendliness.

2.2.2 Filter design background

In our setup, the amplification of signals within a certain frequency range is crucial. To accomplish this, we first need to address the background theory of the main building blocks of our design: the *filters*. Filter examples include the *low-pass filter* (LPF), the *high-pass filter* (HPF), the *band-pass filter* (BPF), and the *notch filter* (NF). Filters can be *passive* or *active*; passive filters are made from passive components and do not require an external power supply. Active filters are implemented by using active components, and, therefore, require an external power supply. Furthermore, the active filter can amplify the signal, where the passive filter cannot. First, we discuss the passive filter.

Passive filters are filters that are built up of passive components like resistors, capacitors, and inductors. An example is the *Half L section* topology, as shown in Figure 2.9. In this figure, the Z_1 and Z_2 represent the passive components.

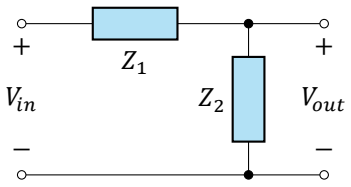

Figure 2.9: *Half L* passive filter topology.

The generalized transfer function of this circuit is given by

$$V_{in}\left(\frac{1}{Z_1}\right) = V_{out}\left(\frac{1}{Z_1} + \frac{1}{Z_2}\right), \tag{2.3}$$

$$\rightarrow \frac{V_{out}}{V_{in}} = \frac{1/Z_1}{1/Z_1 + 1/Z_2} = \frac{1}{1 + \frac{Z_1}{Z_2}}. \tag{2.4}$$

If we assume that Z_1 is a resistor ($Z_{resistor} = R$) and Z_2 a capacitor ($Z_{capacitor} = \frac{1}{sC}$), a LPF is created with transfer function

$$\frac{V_{out}}{V_{in}} = H(s) = \frac{1}{1 + sRC}, \tag{2.5}$$

and the cutoff frequency can be determined by

$$f_c = \frac{1}{2\pi RC}. \tag{2.6}$$

BPF are often designed by cascading a LPF and a HPF; however, the frequency response of two cascaded *resistor-capacitor* (RC) circuits is not simply the product of the two first-order transfer functions. The input and output impedance of consecutive RC circuits could result in deviated filter behavior. Furthermore, the gain of a passive filter is always less than or equal to 1. In other words, signals cannot be amplified using passive filters. Therefore, we need to consider an active filter topology [63]. This topology has many advantages that are essential for our design, which we will discuss next.

In this thesis, we designed the active LPF and HPF, using the *Sallen-Key* topology as illustrated in Figure 2.10. This topology has several advantages: 1) Simple design, 2) a non-inverting amplifier is used to increase the voltage gain, 3) the filter has a high input impedance and a low output impedance, 4) it is a second-order filter (40 dB/decade roll-off), and 5) the damping factor ζ can be determined to shape the filter's behavior [64]. These advantages are important for our design since we deal with low-voltage signals that should be amplified and band-pass filtered using several cascaded filter stages. Furthermore, our overall amplifier design should be straightforward.

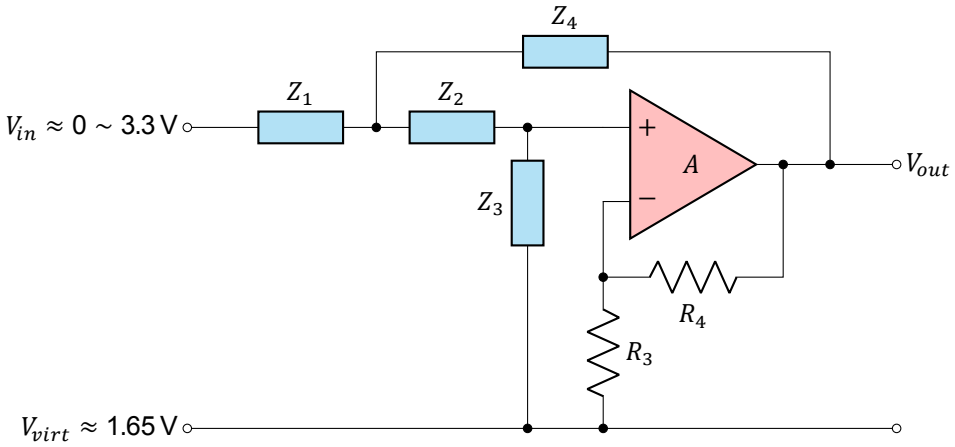

Figure 2.10: Generalized Sallen-Key circuit.

The ideal transfer function of this Sallen-Key filter is given by

$$\frac{V_{out}}{V_{in}} = \frac{K}{\frac{Z_1 Z_2}{Z_3 Z_4} + \frac{Z_1}{Z_3} + \frac{Z_2}{Z_3} + \frac{Z_1(1-K)}{Z_4} + 1}, \tag{2.7}$$

where $K = 1 + \frac{R_4}{R_3}$. We configured a second-order LPF by selecting $Z_1 = R_1$, $Z_2 = R_2$, $Z_3 = \frac{1}{sC_1}$, and $Z_4 = \frac{1}{sC_2}$. The second-order HPF was created by selecting $Z_1 = \frac{1}{sC_1}$, $Z_2 = \frac{1}{sC_2}$, $Z_3 = R_1$, and $Z_4 = R_2$. We will later refer to these LPF and HPF designs during the elaboration on the design of the different modules as presented in Figure 2.8.

2.2.3 Driven right leg circuit background

EMI and PLI (Section 2.1.3) become dominant when measuring neurophysiological signals in the order of tens of µV. The capacitive coupling – resulting in a common-mode voltage V_{cm} on the inputs of the amplifier – impairs the output of the amplifier V_{out}.

To limit the effect of PLI on the output, the voltage difference between the patient and the amplifier reference can be actively reduced. The common-mode is monitored constantly and mirrored around the reference voltage (in this case V_{virt}) and driven back to the body [65]. In other words, we force the common-mode voltage V_{cm} to become equal to the reference voltage $V_{virt} \approx 1.65\,\text{V}$, by actively driving a current to cancel any voltage deviation between the patient and the reference. This method is called *driven right leg* (DRL) and is designed around an (inverting) *operational amplifier* (or *opamp*) integrator with *direct current* (DC) gain control, as seen in Figure 2.11. The DC voltage gain A_{v_0} and corner frequency f_0 of the opamp integrator with DC gain control are defined by

$$A_{v_0} = \frac{R_2}{R_1}\text{, and} \quad f_0 = \frac{1}{2\pi C R_2}. \tag{2.8}$$

We will refer to this DRL circuit during the design of the preampliers.

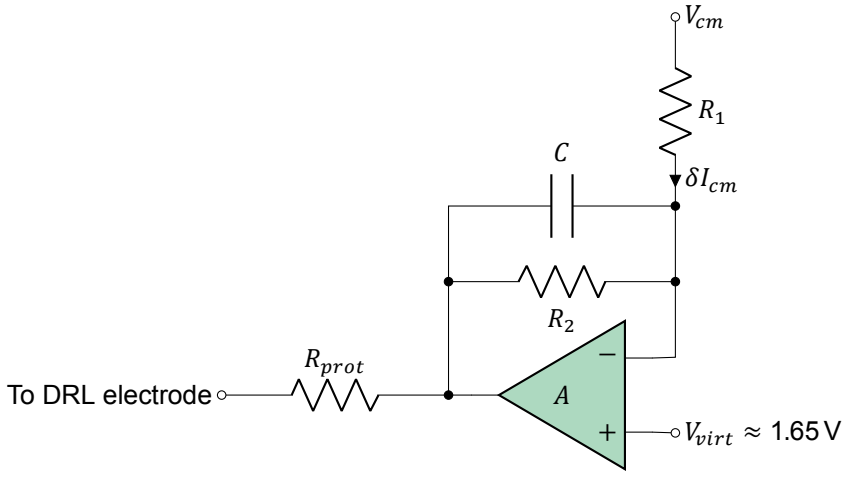

Figure 2.11: DRL circuit to actively steer the common-mode voltage towards V_{virt}. The circuit consists of an (inverting) opamp integrator with DC gain control. The patient protection resistor R_{prot} limits the current δI_{cm} – to cancel the voltage deviation – up to a maximum of 10 µA. Adapted from [59].

2.2.4 Preamplifier v1.0

The preamplifier is the first filter and amplification stage of our setup. Signals in the order of a few tens of µV are magnified to mV. Figure 2.12 shows the inputs and outputs of the preamplifier. The *inputs* of this module include the power supply, the nerve lead L_{nerve}, and the reference lead L_{ref}. The *output* consists of the driven right leg lead L_{DRL} to reject PLI, the amplified signal V_{signal}, the reference voltage V_{ref}, and the leads-off detection lines $LOD+$ and $LOD-$.

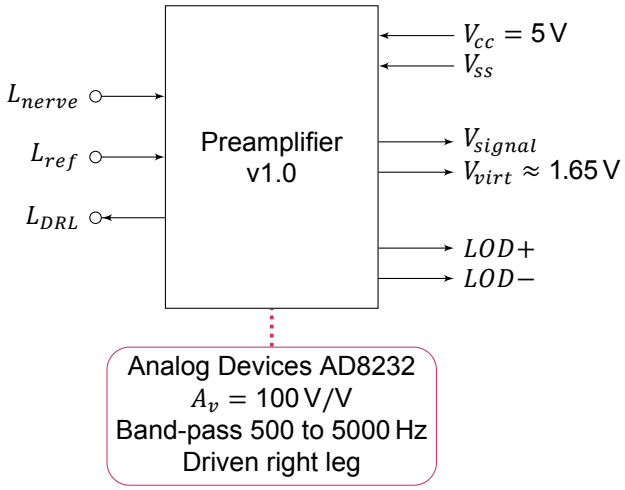

Figure 2.12: Inputs and outputs of preamplifier v1.0.

2.2.4.1 Circuit design

AD8232 To ensure reproducibility and to simplify the design, the system utilizes commercially available *integrated circuits* (IC). *Analog Devices* supplies a single-lead heart rate monitor front end, the AD8232. Although this device is designed for (wearable) fitness and activity heart rate monitors, it contains an *instrumentation amplifier* (IA), multiple LPFs and HPFs, a DRL circuitry, an *operational amplifier* (opamp) for additional gain, and EMI filters. The frequency cutoff (f_c) of all filters, additional gain, and DRL specifications are user selectable, making it a suitable IC for our preamplifier.

Power supply The AD8232 requires a clean power supply. We used an *low-dropout* (LDO) regulator to regulate the voltage $V_{cc} = 5\,V$ down to $V_{supply} = 3.3\,V$. A *light-emitting diode* (LED) was included for visual feedback.

Band-pass filter and biopotential amplifier We designed our band-pass filter and amplifier around the AD8232. Using the various opamps, we designed an second-order high-pass filter at $f_c = 500\,Hz$, and a first-order low-pass at $f_c = 5000\,Hz$. The internal gain of $A_v = 100\,V/V$ was used without additional gain. The biopotential between L_{nerve} and L_{ref} is amplified in respect to the voltage reference V_{virt}, also called 'virtual ground', which is $\approx 1.65\,V$. As an example, a biopotential (within the bandwidth's cutoff frequencies) between $-100, \ldots, 100\,\mu V$ will be amplified such that $V_{signal} = 1.64, \ldots, 1.66\,V$. Without a virtual ground, the amplifier will saturate, resulting in improper output voltages.

Interference rejection The *AD8232* embeds a DRL circuit (Section 2.2.3) that we used to suppress PLI. Besides the PLI, other frequency ranges of EMI are essential to consider. The radio frequency is the range between several tens of kHz and hundredths of GHz, with the inference caused by these frequencies called *radio frequency interference* (RFI), and can be canceled by a passive low-pass filter. The AD8232 includes two 1 MHz passive low-pass filters on the inputs of the instrumentation amplifier.

Patient safety To avoid safety hazards, no hardware fault may result in large currents through the patient. Therefore, a protection resistor R_{prot} is added in series with the different electrodes. The maximum leakage current for medical equipment is defined at 10 µV resulting in $R_{prot} = 330\,k\Omega$ (assuming a supply voltage of 3.3 V).

Leads-off detection The AD8232 includes a number of smart features, including a leads-off detection. Using the DRL electrode, the common-mode voltage will be in the range of $V_{virt} \approx 1.65\,\text{V}$. By connecting a pull-up resistor between the amplifier input and the power supply, the device can detect deviations and indicate which lead is probably not connected using the $LOD+$ and $LOD-$ outputs.

2.2.4.2 Board design

We designed a small two-layer *printed circuit board* (PCB), that can easily be shielded using a case. Figure 2.13 and 2.14 show the design of the 20 mm × 30 mm PCB. The wire to the main amplifier is soldered directly onto the board $(1, \ldots, 6)$ to limit the interference and to create a robust connection. Finally, the leads are connected to the PCB using a pluggable terminal block to simplify the (dis)connecting of the leads. In Figure A.15 of Appendix A.11, we show the different steps of the assembling process.

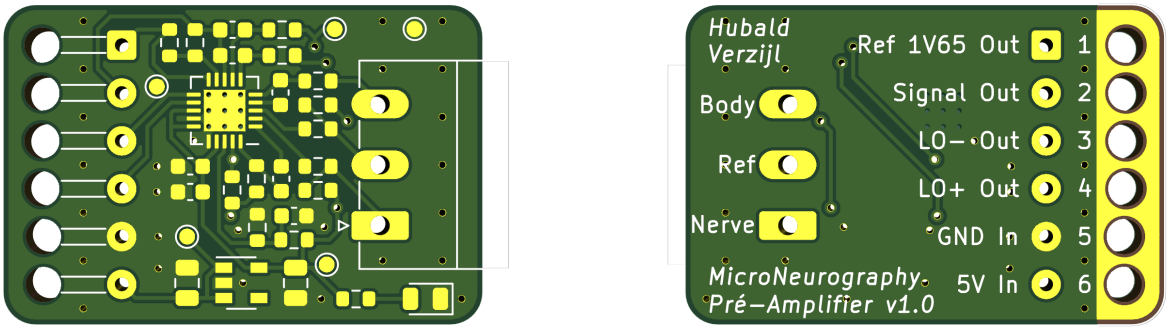

(a) Preamplifier v1.0 front.

(b) Preamplifier v1.0 back.

Figure 2.13: Preamplifier v1.0 board design.

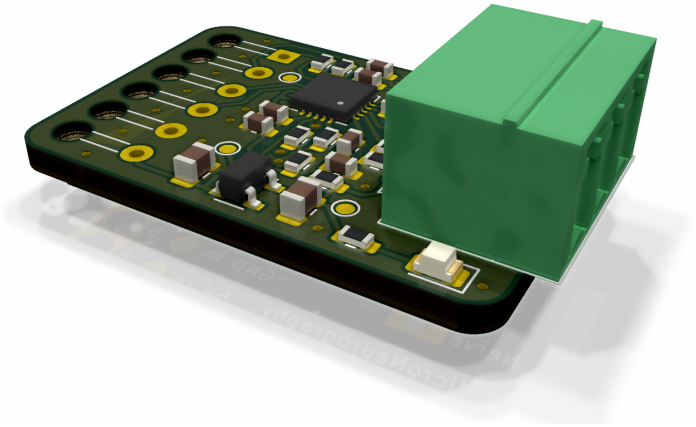

Figure 2.14: 3D render of preamplifier v1.0 board design including components.

2.2.4.3 Prior validation

Prior to the first validation of the system, it became clear that preamplifier v1.0 (based on the AD8232) contained an advanced feature that hampered the preamplifier's performance. Furthermore, some clipping of the input signals was observed. In the following paragraphs, we first discuss these phenomena before we examine the design of the improved preamplifier v2.0.

Too much intelligence The AD8232 was originally designed for activity heart rate monitors, which uses conductive pads attached to the body as electrodes to perform an *electrocardiogram* (ECG). In this situation, the electrode-skin impedance is around several tens of kΩ [66]. We connected microneurography electrodes (which have a non-isolated tip, as discussed in Section 2.1.2) to the amplifier input. These electrodes resulted in an impedance in the order of GΩ that activated the leads-off detection.

Subsequently, the output of the amplifier was blocked. Therefore, our preamplifier could not measure any biopotentials using the microneurography electrodes, which led to a re-evaluation and re-design of the hardware, which will be discussed in Section 2.2.5.

Clipping Without connecting any electrodes, the preamplifier v1.0 mainly amplified the PLI of 50 Hz. However, the frequency domain of the output signal also showed large magnitudes at the harmonic frequencies of 50 Hz. This phenomenon could be explained by the fact that the amplifier became saturated; namely, the input signal amplitude multiplied by the amplifier's gain exceeded the output voltage range. In this case, the output voltage was clipped and had the appearance of a square wave. In the frequency domain, this resulted in odd-integer harmonic components [67].

If a signal is symmetrically clipped with respect to the waveform, the frequency domain shows large magnitudes at the components of odd-integer harmonics ($f, 3f, 5f, 7f, ...$ Hz). However, if the signal is not symmetrically clipped, the frequency domain shows large magnitudes at only the components of integer harmonics ($f, 2f, 3f, 4f, ...$ Hz). The latter was observed in our preamplifier v1.0.

PLI rejection In case of PLI presence, a 50 Hz notch filter must be included after a high gain amplification stage to suppress the PLI. However, in the case of amplifier saturation (as discussed above), the amplifier induces harmonic signals that the subsequent notch filter will not suppress. Therefore, the output signal still contains a lot of noise.

The preamplifier v1.0, based on the AD8232, contains a DRL circuit (Section 2.2.3) to suppress the PLI. However, it includes a single (high-gain) instrumentation amplifier without any notch filter. An inadequate working DRL circuit will result in clipping inside the instrumental amplifier and, therefore, a lot of noise at the output.

Therefore, a better solution would be implementing a multi-stage amplifier. The first stage amplifies the signal with a small gain, and the output signal will not clip. Furthermore, this stage also has a large output impedance. After this stage, the 50 Hz signals are suppressed using a notch filter. The subsequent stages amplify the signal even further, and now clipping does not occur since the 50 Hz is absent. A DRL could potentially improve the PLI rejection even further. This multi-stage design was implemented in the preamplifier v2.0 (Section 2.2.5).

2.2.5 Preamplifier v2.0

The first preamplifier design (based on the AD8232) was not able to measure any biopotentials using microneurography electrodes. We re-designed the hardware, leaving out all unnecessary features, such as the leads-off detection. We focused on a system that has sufficient gain, proper filtering, and interference rejection. At this point, we have already designed and built the main amplifier (Section 2.2.6). For a system compatible with the main amplifier, we defined the same inputs and outputs as for preamplifier v1.0, except for the leads-off detection lines (as shown in Figure 2.15).

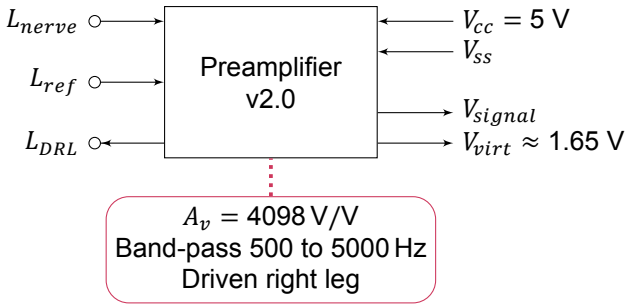

Figure 2.15: Inputs and outputs of preamplifier v2.0.

2.2.5.1 Circuit design

Recording nerve activity is performed by (neuro)-scientists all over the world. Today, even children can experiment with electrophysiology using the setup shown in Figure 2.16: the *Neuron SpikerBox* built by *Backyard Brains* [68]. This kit contains an amplifier and recording electrodes (ball pins) to record APs in a cockroach's leg and visualize the results on a smartphone. The electronic design of SpikerBox is open source, making it a good starting point for the design of our preamplifier to record neural activity using microneurography electrodes.

The design of our preamplifier v2.0 consists of several amplification and filter stages based on SpikerBox's design. Figure 2.17 shows our adapted global system design after including additional filtering stages and a DRL circuit to reject interferences. Next, we elaborate on the different stages. The complete schematic can be found in Appendix A.8.

Figure 2.16: Neuron SpikerBox to record neural signals from cockroach nerves [68].

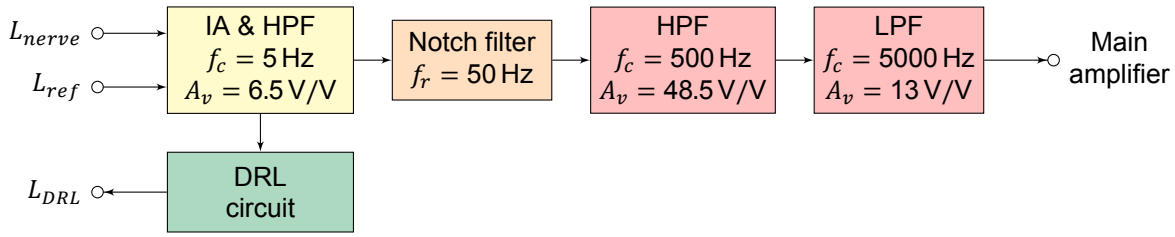

Figure 2.17: Global system design of preamplifier v2.0. The *instrumentation amplifier* is indicated by IA. HPF and LPF represent the *high- and low-pass filters*.

Instrumentation amplifier & high-pass filter circuit The first stage (after the protection resistors R_{prot}) is shown in Figure 2.18. This stage amplifies the potential difference between L_{nerve} and L_{ref}, and attenuates the lower frequencies. To suppress any common-mode on the input V_{in}, an *instrumentation amplifier* (IA) with a sufficiently large CMRR is required. We selected the *INA826*, an IA with a CMRR of 100 dB (at 5 kHz and gain $A_v = 5$ V/V). The INA826 supports a common-mode range that extends to below single-supply ground, and this allowed us to ground L_{ref} in a future stage while persevering the possibility to amplify potential differences.

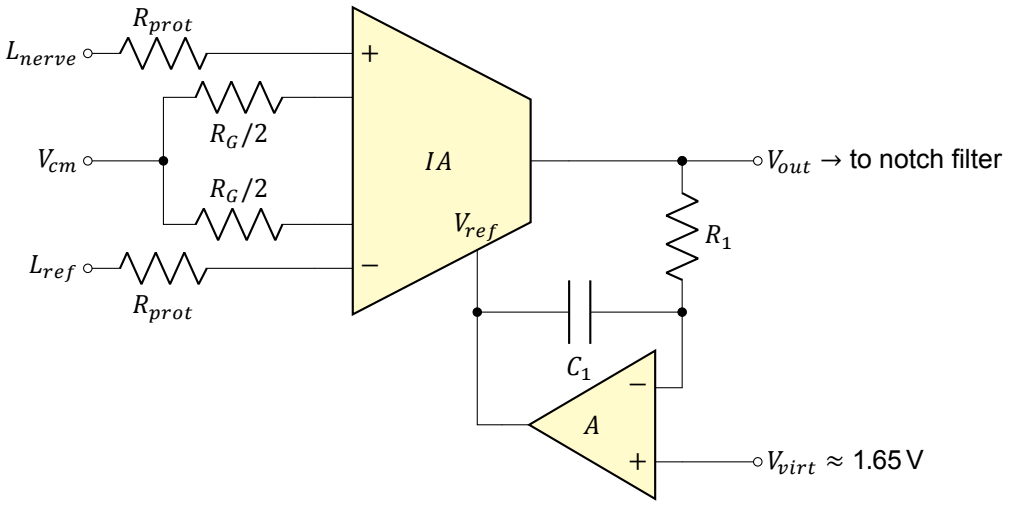

Figure 2.18: IA and HPF stage. The potential difference between L_{nerve} and L_{ref} is amplified and shifted by 1.65 V. A HPF at $f_c \approx 5$ Hz removes any DC offset.

We created a voltage level midway between the ground (0 V) and V_{ss} (3.3 V). This voltage is called the *virtual ground* V_{virt} and is created by a voltage divider followed by an opamp buffer resulting in $V_{virt} = 1.65$ V. We use V_{virt} throughout the different stages.

After the amplification, we shifted the output of the IA by the virtual ground level (1.65 V) using V_{ref} as input of the IA. Hence, $V_{out} < V_{virt}$ if $L_{nerve} < L_{ref}$ and $V_{out} > V_{virt}$ if $L_{nerve} > L_{ref}$. By doing so, we are able to amplify the potential difference correctly (without saturating the IA) while using a single (or only positive) power supply.

To complete this stage, we designed a (first-order) HPF to remove any DC offset. For this, we selected $f_c \approx 5$ Hz, using the equations presented in Section 2.2.2. To satisfy the design requirements, we selected the passive components as shown in Table 2.1.

IA and HPF circuit
$A_v = 6.5$ V/V, $f_c = 5$ Hz

Component	*Value*
R_G	9.4 kΩ
R_1	300 kΩ
C_1	0.1 µF

Table 2.1: Passive component values of the IA and HPF stage, shown in Figure 2.18.

Driven right leg circuit We used the DRL circuit (Section 2.2.3) from Figure 2.11 (including an opamp buffered V_{virt}) to steer V_{cm} to potential level of the virtual ground V_{virt}. Using Equation (2.8), we selected the passive components (Table 2.2) such that the opamp integrator with DC gain control has a gain of $-19.5\,\mathrm{V/V}$ and a cutoff frequency of $f_c = 400\,\mathrm{Hz}$.

DRL circuit
$A_v = -19.5\,\mathrm{V/V}$, $f_c = 400\,\mathrm{Hz}$

Component	*Value*
R_1	20 kΩ
R_2	390 kΩ
C	39 pF

Table 2.2: Passive component values of the DRL circuit, shown in Figure 2.11.

Notch filter circuit Although the DRL circuit and a high CMRR of the IA will suppress the CM voltages (caused by the PLI), the DM voltage (caused by, e.g., PLI on the leads) may still be amplified by the IA. Therefore, we applied additional filtering after the IA stage. By parallelizing a HPF and a LPF, a band-stop filter can be designed. A band-pass filter that rejects a tiny band of frequencies is called a *notch filter*. We used a *Twin-T notch filter* (as shown in Figure 2.19) to filter out any PLI interference around 50 Hz after the IA stage. To obtain a low impedance filter output, we applied an opamp buffer.

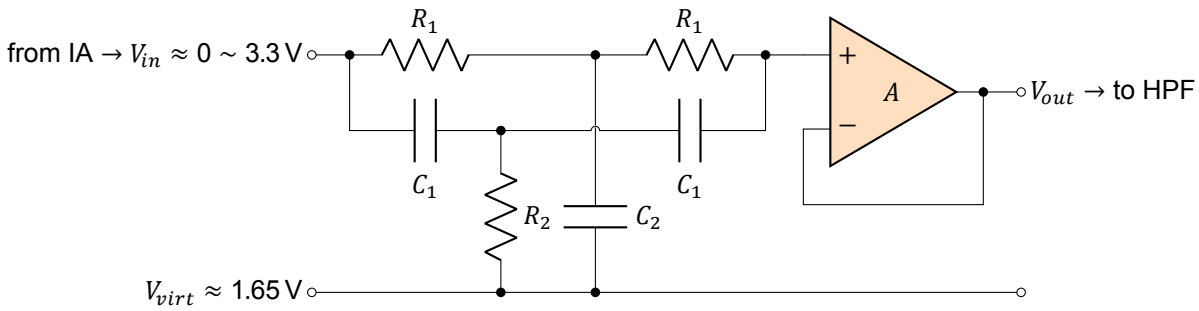

Figure 2.19: Twin-T notch filter including opamp buffer.

A transfer function of this circuit can be obtained with help from [69]. The required passive component values to suppress frequencies in the range of 50 Hz are shown in Table 2.3. The corresponding Bode plot is shown on Figure A.13a of Appendix A.7, where we observe that the 50 Hz PLI is suppressed with an additional 50 dB.

Notch filter circuit
$f_c = 50\,\mathrm{Hz}$, $A_v = 1\,\mathrm{V/V}$

Component	*Value*
R_1	300 kΩ
R_2	33 kΩ
C_1	22 nF
C_1	10 nF

Table 2.3: Passive component values of the notch filter, shown in Figure 2.19.

Band-pass filter and amplification circuit We designed our HPF and LPF (including signal gain) based on the Sallen-Key topology (which is an active filter, see Section 2.2.2). The cascaded HPF and LPF were created by the passive components as defined in Table 2.4. The resulting Bode plot for the HPF, LPF, and cascaded filters are shown in Figure A.13b, A.13c, and A.13d of Appendix A.7. Component tolerances may influence the behavior as we illustrate in Figure A.13c of Appendix A.7.

HPF circuit $f_c = 500\,\text{Hz}$, $\zeta \approx 0.707$ $A_v = 48.5\,\text{V/V}$		**LPF circuit** $f_c = 5000\,\text{Hz}$, $\zeta \approx 0.707$ $A_v = 13\,\text{V/V}$	
Impedance	*Value*	*Impedance*	*Value*
$Z_1 = \frac{1}{sC_1}$	$C_1 = 1\,\mu\text{F}$	$Z_1 = R_1$	$R_1 = 412\,\Omega$
$Z_2 = \frac{1}{sC_2}$	$C_2 = 0.1\,\mu\text{F}$	$Z_2 = R_2$	$R_2 = 1.1\,\text{k}\Omega$
$Z_3 = R_1$	$R_1 = 680\,\Omega$	$Z_3 = \frac{1}{sC_1}$	$C_1 = 0.1\,\mu\text{F}$
$Z_4 = R_2$	$R_2 = 4.7\,\text{k}\Omega$	$Z_4 = \frac{1}{sC_2}$	$C_2 = 22\,\text{nF}$

Table 2.4: Impedances of Z_1, Z_2, Z_3, and Z_4 to create a HPF and LPF that satisfy our design requirements. The damping factor is indicated by ζ.

2.2.5.2 Board design

We designed again a small two-layer PCB as shown in Figure 2.20 and 2.21. Since the board contains more components compared to preamplifier v1.0, the dimensions have increased to 50 mm × 15 mm. The connections are comparable to preamplifier v1.0: the wire to the main amplifier is directly soldered onto the board, and the leads are connected through the pluggable terminal block. This board is assembled in a similar way as shown in Appendix A.11.

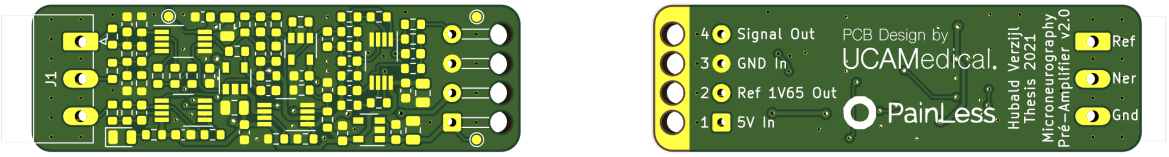

(a) Preamplifier v2.0 front.

(b) Preamplifier v2.0 back.

Figure 2.20: Preamplifier v2.0 board design.

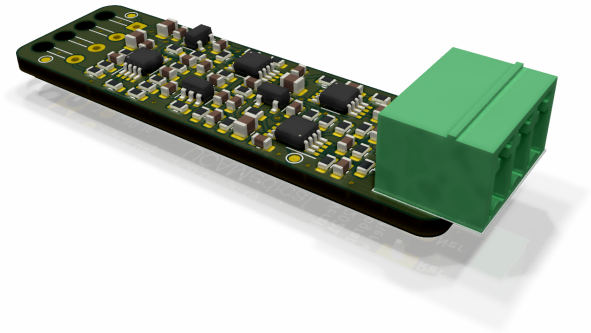

Figure 2.21: 3D render of preamplifier v2.0 board design including components.

Overall theoretical performance We presented the different amplification and filtering stages of preamplifier v2.0. Cascading the different stages should lead to a successful biopotential amplifier. To illustrate the frequency response of the cascaded stages, we performed an analysis of the cascaded system as shown in Figure A.13d of Appendix A.7. From this figure, it is evident that the amplifier has a steep roll-off for frequencies below 500 Hz and above 5000 Hz. Furthermore, the notch filter frequency is visible.

2.2.6 Main amplifier

The main amplifier is the final hardware stage before the host software, with Figure 2.22 showing its different inputs and outputs. This stage digitizes the signals from the preamplifiers, contains computational power, implements communication interfaces, and creates supply voltages for the different hardware units. The communication interfaces include a *universal serial bus* (USB), *serial peripheral interface* (SPI), and *universal asynchronous receiver-transmitter* (UART) bus, which we will discuss in more detail in the following sections.

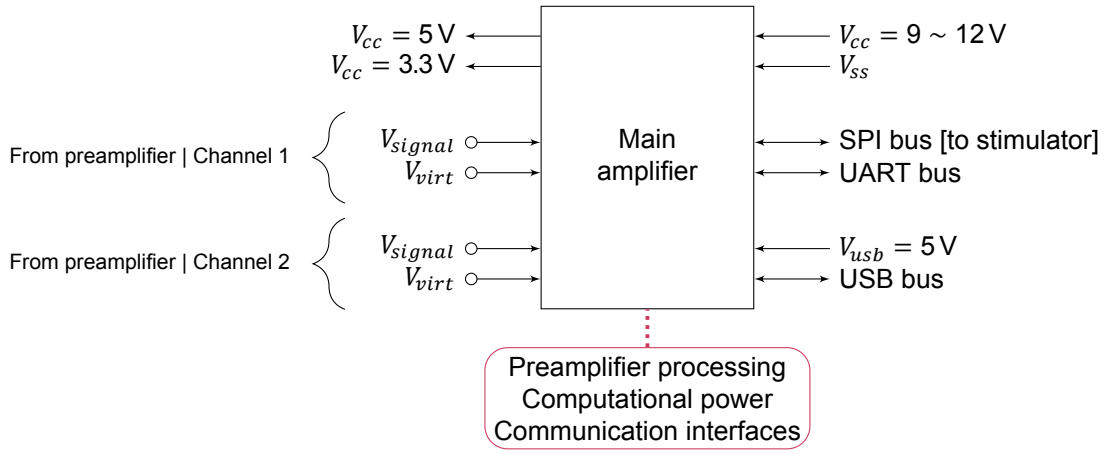

Figure 2.22: Inputs and outputs of the main amplifier.

2.2.6.1 Circuit design

In this part we go into detail on several essential elements of the main amplifier. We refer for the complete schematic of the main amplifier to Appendix A.9.

Microcontroller The heart of the main amplifier is the *STM32F446RE*, a *microcontroller unit* (MCU) with an Arm Cortex-M4 32-bit *central processing unit* (CPU). The Cortex-M4 CPU can run up to a frequency of 180 MHz and provides a *floating point unit* (FPU) single precision coprocessor core. The STM32F446RE contains, among other things, flash memory of up to 512 *kilobytes* (kB), several 12-bit ADCs, and (advanced) communication interfaces like USB and SPI. This MCU complies with the computational power and communication interfaces requirements.

Power supply A 9 V battery is used as the primary energy source to create an isolated system. To prevent any additional noise, an LDO regulator lowers the supply voltage to 5 V. Next, two LDO regulators are applied to create a supply voltage of 3.3 V for the analog domain (containing the preamplifier input processing parts), and a separate supply for the digital parts (e.g., MCU, digital communication interfaces). Cascading multiple LDO regulators is an inefficient way to lower the supply voltage from 9 V to 3.3 V; however, this method produces less additional noise compared to a *switched-mode power supply* (SMPS). Given our design requirements, efficiency is not essential.

Similar to the preamplifier, we created a virtual ground by using a voltage divider and an opamp buffer. We generated a separate virtual ground for each preamplifier channel, and we will refer to this voltage as V_{offset}.

Preamplifier input processing One of the essential tasks of the main amplifier is the digitization of the preamplifier signals. Before these signals enter the ADC, the signal goes through several stages, as we show in Figure 2.23. Firstly, the input signals from the preamplifier (V_{signal} and V_{virt}) are subtracted using an IA, and the output is shifted by the virtual ground level V_{offset}. This stage ensures that the input signal is referenced to V_{offset} instead of V_{virt} and buffers the input signal. Subsequently, the signal passes through a notch filter, as we introduced in Figure 2.19. This filter can be enabled or disabled by the user. In Section 2.2.2 we introduced the design of a HPF and a LPF. These filters are applied in the filtering stages for $\zeta \approx 0.707$. The user can enable the filters and select the cutoff frequency of the

HPF (f_c =50 Hz or 500 Hz) and the LPF (f_c = 2500 Hz or 5000 Hz), or can disable the filters. We refer to Appendix A.9 for exact circuit layout and component selection. The final stage before the ADC is the *programmable-gain amplifier* (PGA) that adds additional gain (between A_v = 1 V/V and A_v = 200 V/V) to increase the signal's amplitude towards the ADC full scale (the minimum and maximum voltages that the ADC can measure). Finally, we use the internal ADC of the MCU, preceded by a passive LPF that serves as an anti-aliasing filter at f_c = 1 MHz.

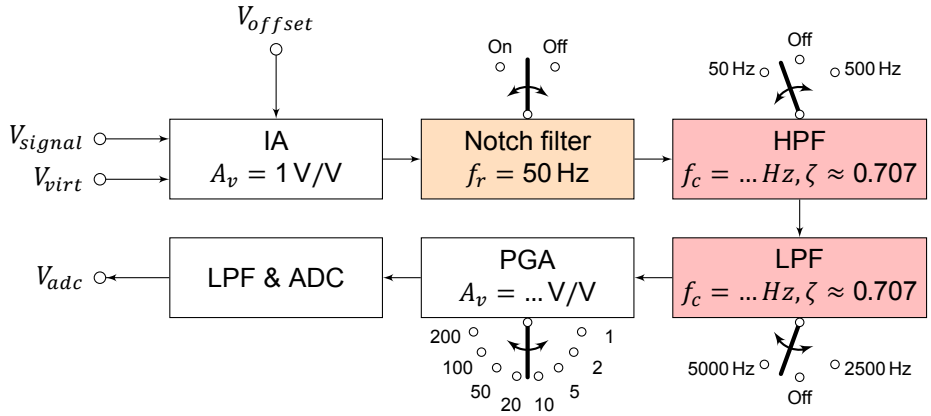

Figure 2.23: Global system design of preamplifier input processing stage on the main amplifier. The *instrumentation amplifier* is indicated by IA. HPF and LPF represent the *high- and low-pass filters*, the *programmable-gain amplifier* is identified as PGA, and the *analog-to-digital conversion* stage as ADC.

Discretizing using ADC We used the internal ADCs of the MCU to sample the signal after the PGA and the virtual ground level V_{offset} simultaneously. We defined the channel voltage as

$$V_{ch} = V_{adc} - V_{offset}. \tag{2.9}$$

In the design requirements (Section 2.1.5), we specified an ADC resolution of at least 14-bits, while the frequency range of interest is between 500 Hz and 5000 Hz. However, the MCU's ADC has a resolution of only 12-bit. Therefore, we will use a technique called *oversampling* to increase the ADC's solution [70].

According to *Nyquist's theorem*, the sampling frequency f_s of an ADC is determined by the highest frequency component f_{max} in the signal, i.e.:

$$f_s > 2f_{max}. \tag{2.10}$$

In our design, f_{max} is equal to the highest frequency component after the LPF. In other words, f_{max} = 5000 Hz, being the highest frequency within the frequency range of interest. Thus, we defined f_s = 20 kHz. Nevertheless, using the MCU's ADC, the resolution is still 12-bit.

Increasing f_s can be used to increase measurement resolution and the *signal-to-noise ratio* (SNR), if we assume that *white Gaussian noise* (WGN) is present on the input. For each additional bit of resolution, we need to oversample the signal by a factor of four

$$f_{os} = 4^w f_s, \tag{2.11}$$

where f_{os} is the oversampling frequency, and w the number of additional bits of resolution. In our situation – we require 2 additional bits – this results in an oversampling frequency of f_{os} = 320 kHz [70]. After taking 16 (12-bit) samples at f_{os} = 320 kHz, the data is averaged to obtain 14-bit samples at 20 kHz. Besides the additional number of bits, oversampling also improves the SNR [70].

However, the cost of oversampling is an increased CPU utilization. The *direct memory access* (DMA) controller can move data from the ADC direct to the *random-access memory* (RAM), independently of the CPU. We set up a DMA stream that continuously fills a buffer of size 16. An interrupt at 20 kHz averages the buffer to obtain a 14-bit sample. The ADC stage is illustrated in Figure 2.24.

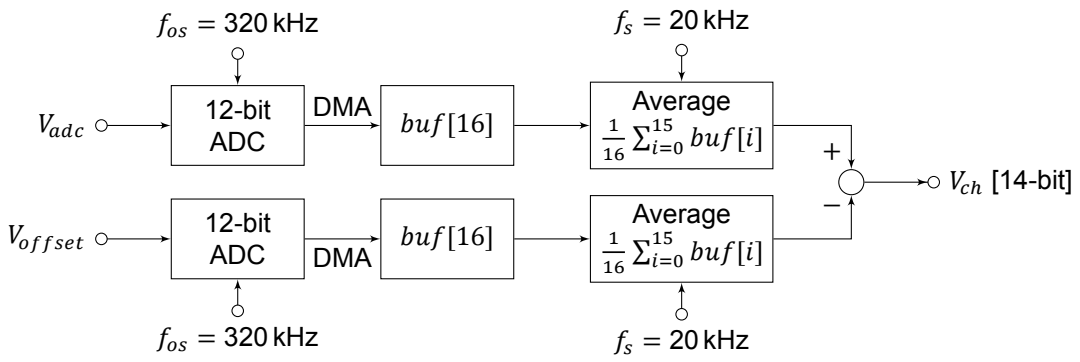

Figure 2.24: ADC with oversampling procedure graphically represented. The buffer of size 16 – containing the 12-bit ADC data – is indicated by buf.

2.2.6.2 Board design

The board design is shown in Figure 2.25 and 2.26. The top part contains the analog circuits, including the preamplifier input processing from Figure 2.23. The different headers can be used in combination with jumpers to select certain cutoff frequencies f_c. The MCU is placed in the bottom left part, together with an USB-C connector and the *serial wire debug* (SWD) header to program the MCU. A connector is placed on the bottom of the PCB; this connector contains the supply voltages and digital communication (SPI) bus for the stimulator (Chapter 3). The bottom right of the PCB is organized as a supply voltage generation area, where the input of the 9 V battery is lowered to several voltage levels. A heat sink can be placed close to the LDO regulator to eliminate the LDO regulator's excess heat. For future use, a star ground is created in the center of the PCB. In Figure A.14 of Appendix A.10 we illustrate the different parts of the board in more detail, and in Appendix A.11 we show the different steps of the assembling process.

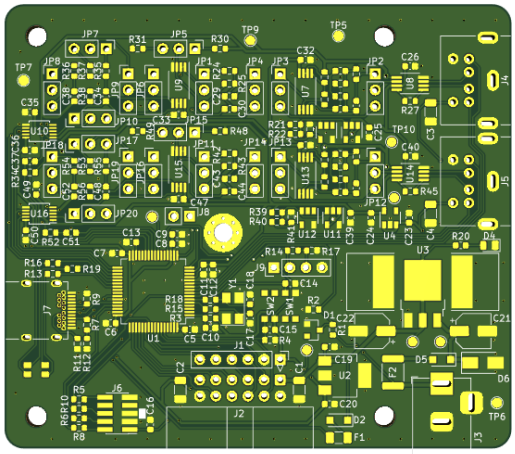

(a) Main amplifier front.

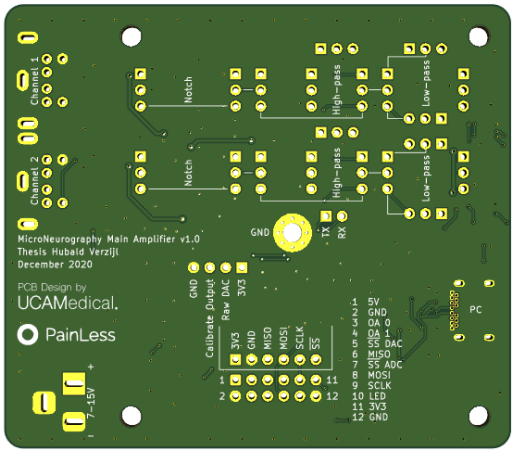

(b) Main amplifier back.

Figure 2.25: Main amplifier board design.

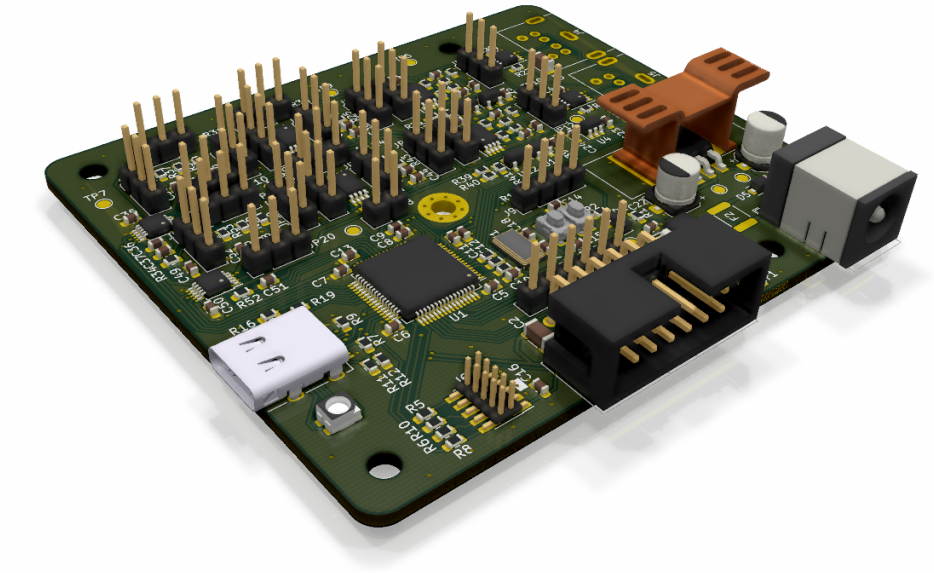

Figure 2.26: 3D render of main amplifier board design including components, without the connectors to the preamplifier.

2.2.7 Software

In the previous sections, we discussed the design of the preamplifier and the main amplifier. Microneurographic signals from the nerve are amplified and digitized in several stages. These data needs to be transferred to a host (e.g., a PC) and visualized there, as a final processing stage. The host is in control of the hardware such that specific settings of the peripherals can be adapted. In Figure 2.27, we show the global design of the software, divided into embedded and host-side software. In the following sections, we will discuss the different aspects of this global design.

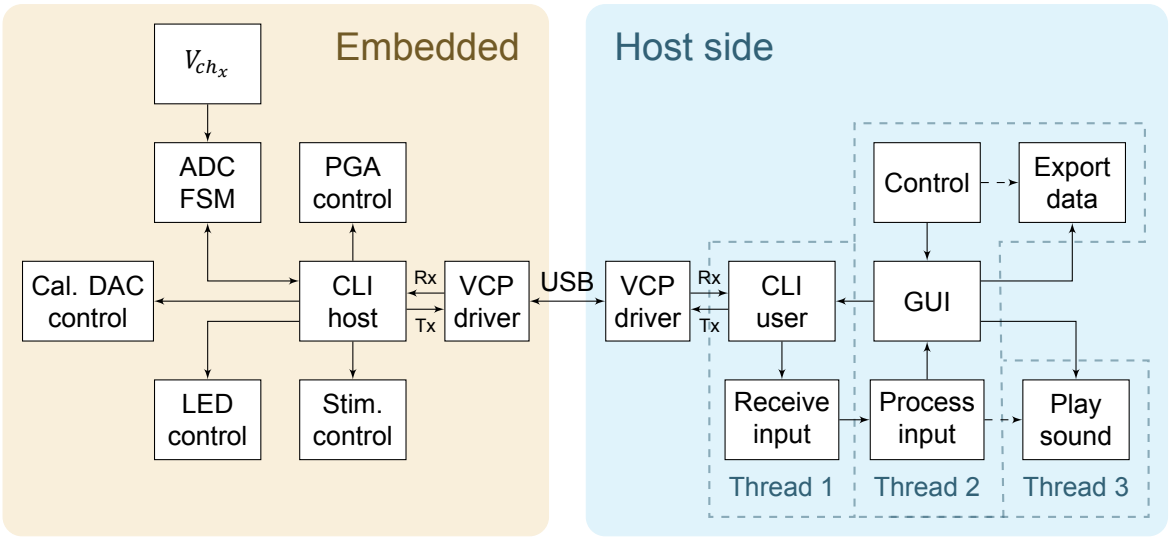

Figure 2.27: Global design of the software, separated in an embedded and a host side. A *virtual COM port* (VCP) is deployed over USB. We use this port for the *command-line interface* (CLI) to control the gain of the *programmable-gain amplifier* (PGA), the *analog-to-digital conversion finite-state machine* (ADC FSM), the *calibration digital-to-analog* (cal. DAC), and the *stimulator* (stim. control). The host entails a *graphical user interface* (GUI) to visualize the recordings and control the hardware.

2.2.7.1 Embedded software

The embedded software (or often called 'firmware') is written in the programming language C by using the *common microcontroller software interface standard* (CMSIS) tools provided by *Arm Ltd.*, for the Cortex-M4 core. The peripherals are set up using the *STM32CubeMX* framework, a graphical tool that allows for a straightforward configuration of STM32 microcontrollers and microprocessors. We compiled and debugged the firmware using the *GNU Arm Embedded toolchain* for the STM32F446RE MCU. To avoid any usage of delay functions, our firmware is interrupt-driven.

Command line interface The firmware on the MCU is in control of the different peripherals of the main amplifier. To read out analog values from the ADC, or adjust the gain of the PGA, we need a communication interface between the MCU and the host. For this purpose, we created a *command line interface* (CLI) over a serial port. We used a *virtual COM (communication) port* (VCP) driver to establish a serial connection (through the build-in USB of the MCU and the build-in USB of the host) to *transmit* (Tx) and *receive* (Rx) messages.

These *American Standard Code for Information Interchange* (ASCII) encoded messages contain commands to control the different peripherals of the hardware but could also contain the digitized signal values of the preamplifier, obtained in the ADC stage. We implemented a CLI to control a variety of functions, which we will discuss next. Using a serial port terminal emulator (e.g., `CoolTerm`), transmitting the command `help` revealed the available *commands* (cmd), as we show in Figure 2.28.

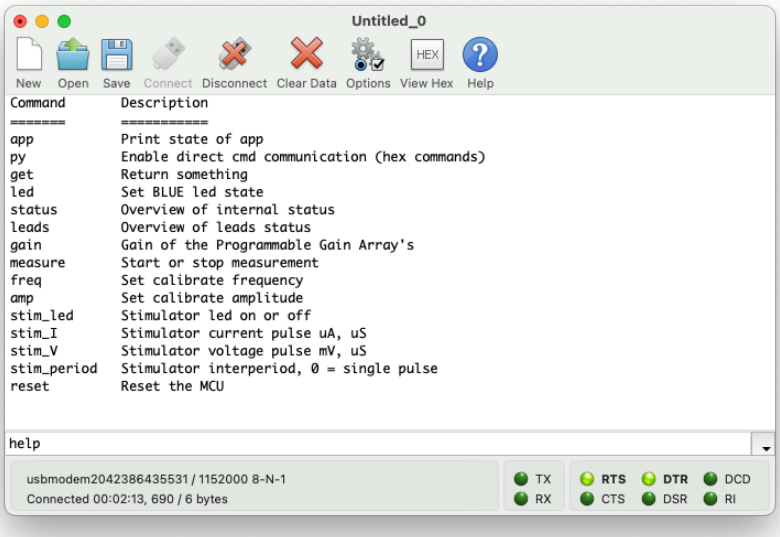

Figure 2.28: *Command line interface* (CLI) over the serial port terminal emulator called `CoolTerm`. Transmitting `help` revealed the available commands.

Analog-to-digital conversion finite-state machine A simple *finite-state machine* (FSM) is implemented to transmit the data from the ADCs through the CLI as shown in Figure 2.29. After a measure

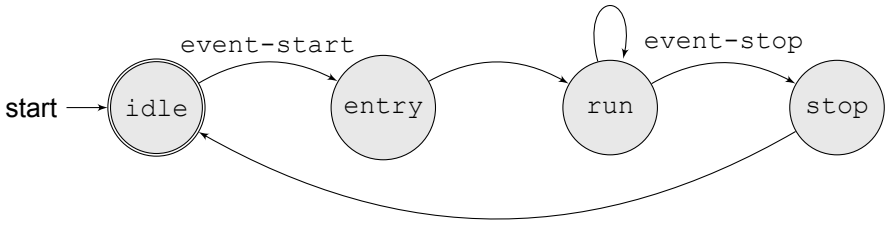

Figure 2.29: Analog-to-digital conversion finite-state machine.

start event (`event-start`), the main amplifier will initialize the correct peripherals (timers, interrupt, ADC, LED) during the `entry` state, and will enter the `run` state. During this stage, the main amplifier generates a stream at 20 kHz, containing the voltages V_{ch} of preamplifier channel 1 and 2. We would like to receive each new sample comma-separated on a new line. For example, it is assumed that we measure a voltage of 1.2345 V on channel A, and a voltage of 0.5678 V on channel B (14-bit resolution). Since our serial port terminal is ASCII encoded, we need to transmit

```
1.2345,0.5678\r\n
```

where `\r` and `\n` represent ASCII 'return' and 'new line' characters. Expressed in data size, this message is 15 bytes, or 120 bits long. Assuming a data-rate of 20 000 samples per second, this results in 2.4 Mbit/s. Although this is within the USB 1.1 requirements of the STM32F446RE (*FullSpeed*, 12 Mbit/s), we can improve this message further to reduce the complexity of the host driver. This method is called the *enhanced communication protocol* and is discussed in the next paragraph.

After an `event-stop` command, the main amplifier will stop the datastream and it will wait in the `idle` state for a future `event-start` command.

Enhanced communication protocol The CLI is ideal for debugging purposes; it is an easy way to test the peripherals of the hardware, in particular, the ASCII encoded messages are human interpretable. However, if the CLI is mainly used by the host side GUI, the messages do not need to be ASCII encoded anymore and can thus be simplified to improve the performance of the CLI. Furthermore, using simplified messages, the performance requirements on the host driver (Section 2.2.7.2) become less important.

To transmit commands from the host to the main amplifier, the ASCII CLI commands are encoded into 32-bit numbers as shown in Table 2.5. This table shows the commands as a hexadecimal number. Additional bytes after the command might be used to pass additional information, e.g., PGA gain for a specific channel number. After the main amplifier receives the command, it will respond with an *acknowledge* command.

Enhanced CLI commands

Command	*Hexadecimal*	*Consecutive data*	*Encoding*
`CliCMDLedOn`	`0x3F3F3F3F`	`None`	
`CliCMDLedOff`	`0x3F3F3F3A`	`None`	
`CliCMDGain`	`0x66667777`	`0xVVWW`	`VV[1:0] = PGA chan [1,2]` `WW[7:0] = PGA gain [1,2, 5,10,20,50,100,200]`
`CLICMDMeasureStart`	`0x88889999`	`None`	
`CLICMDMeasureStop`	`0x99998888`	`None`	
`CliCMDStimV`	`0x22223333`	`0xVVVVVVVV`	`V...V[31:0] = mV [32-bit]`
		`0xWWWWWWWW`	`W...W[31:0] = uS [32-bit]`
`CliCMDStimI`	`0x22223333`	`0xVVVVVVVV`	`V...V[31:0] = uA [32-bit]`
		`0xWWWWWWWW`	`W...W[31:0] = uS [32-bit]`
`CliCMDStimInterPulse`	`0x22223333`	`0xVVVVVVVV`	`V...V[31:0] = uS [32-bit]`

Table 2.5: Commands of the enhanced communication protocol.

Every byte that is transmitted from embedded to the host side is build up using a certain structure, as we show in Figure 2.30. The 6 *most significant bits* (MSB) contain the bits of a 16-bit number $D = D_{15}, \ldots, D_0$, the *least significant bit* (LSB) defines which channel is represented by number D. The second LSB indicates whether the data byte contains control parameters. In case an acknowledgement should be sent by the main amplifier, an *OK-command* is send, which is defined as `0b00000011` (the command bit and the channel bit are set to 1).

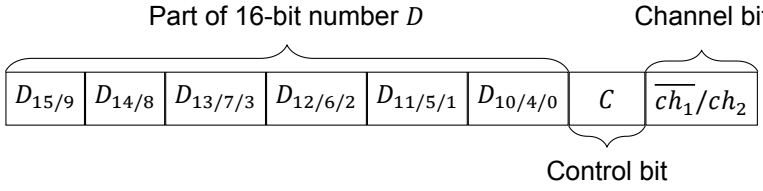

Figure 2.30: Encoded data byte, transmitted from the embedded to the host side. The 6 MSBs contain parts of a 16-bit number D. The LSB is used to link the number D to the ADC channel. The second LSB is used for control byte encodings.

We devised a method to transmit V_{ch} (14-bit resolution stored in a 16-bit integer) of both channels within a 6-byte message `buf[]`, by encoding the data in the byte structure as shown in Figure 2.30. First, the 16-bit number V_{ch} of channel 1 is split in a two 6-bit numbers and one 4-bit number. These parts of the 16-bit number are placed into the 6 MSBs of `buf[0]`, `buf[1]`, and `buf[2]`. Furthermore, the LSB of these bytes is set to 0 (indicating that the number represents the first channel. We did the same for the second channel (V_{ch} of channel 2 splitted into three parts and placed into the 6 MSBs of `buf[3]`, `buf[4]`, and `buf[5]`), however, the LSB is set to 1 (represents V_{ch} of second channel). In Listing 2.1, we show the bitwise operations to create the 6-byte buffer using the channel voltages. Using logical shifts, the message `buf[]` is constructed.

Listing 2.1: Bitwise operations to create the 6-byte buffer using the channel voltages

```
buf[0] = ((ch_1 >> 8) & 0xFC) | 0x00;
buf[1] = ((ch_1 >> 2) & 0xFC) | 0x00;
buf[2] = ((ch_1 << 2) & 0x3C) | 0x00;
buf[3] = ((ch_2 >> 8) & 0xFC) | 0x01;
buf[4] = ((ch_2 >> 2) & 0xFC) | 0x01;
buf[5] = ((ch_2 << 2) & 0x3C) | 0x01;
```

Additional features Some commands of the human interpretable CLI, as seen on Figure 2.28 are briefly presented here. When, using the command `leads`, the leads-off detection status of preamplifier v1.0 can be accessed. The command `gain` controls the gain of the PGA, the command `led` the blue LED, and the commands `amp` and `freq` the amplitude and frequency of the validation *digital-to-analog converter* (DAC). The measurements are started with `measure` and the stimulator is controlled by `stim_*`. The latter will be discussed in Chapter 3. All these commands have an equivalent hexadecimal command for the enhanced communication protocol.

2.2.7.2 Host side software

For the host side-software, we used `Python` as a programming language to implement the different elements of Figure 2.27. `Python` is a rudimental programming language, for which many libraries are available to extend its functionality. However, since `Python` is an interpreted language, it might introduce delays compared to compiled languages such as C. Therefore, we created several threads that run in parallel. A thread is a separate flow of execution. In other words, using threads, the software can perform multiple tasks simultaneously. Without these multiple threads, we may miss out on preamplifier data and may have to deal with frozen software.

Thread 1 - Command-line interface The first thread uses the CLI over the serial port by implementing a VCP driver in `Python`. This thread is in charge of the serial port and is constantly checking for incoming data, e.g., checking for potential control bytes (control bit set to 1) and processing the data stream that contains a 6-byte buffer at 20 kHz encoding the V_{ch} voltages. These encoded voltages are real-time processed, and the data is passed to a `Numpy` array. Since this thread is constantly running, using the standard (interpreted) `Python` functions would introduce a huge delay. Therefore, we used the `Numba` library that translates Python functions to optimized machine code at runtime [71]. During the first run, the software runs slower, since it needs to compile the code. However, the compiled code after the first run can be reused, resulting in significant time savings.

Besides receiving data, this thread is also responsible for transmitting commands. In the embedded software part, we presented that the CLI was implemented using ASCII encoded commands. To reduce the message length, we encoded the commands in hexadecimal numbers, as provided by Table 2.5.

Since the incoming data rate is high (around 960 kbit/s), adding more tasks to this thread may result in losing samples. Two different threads will perform the other tasks of the host software.

Thread 2 - Graphical user interface The ease of use is essential during complicated microneurographic recordings. Therefore, we created a *graphical user interface* (GUI) that permits users to use graphic items (e.g., buttons) to control the functionalities of the main amplifier. Under the hood, the GUI sends specific CLI commands (of the enhanced communication protocol) if, e.g., a button is pressed.

We used the `Qt` framework to create the GUI, with the `PySide` package providing the bindings for `Python`. Figure 2.31 shows the implemented functionality of the GUI. Here we discuss the various elements in more detail.

- *Start/stop button* [top left]: start the 20 kHz data stream containing voltages of both preamplifier channels.
- *Graphs* [bottom]:
  1. *mV ADC*: real-time ADC voltage, one channel is plotted. The x-axis is 2 seconds.
  2. *uV*: real-time microneurography value, gain of amplifier is used to determine electrode voltages. The x-axis is 2 seconds.

3. *mV*: as 1), but with a smaller timescale of 0.1 second. If the *mV ADC* exceeds the threshold defined by the *dial button* [top left], the result is shown in this graph.
4. *Magnitude*: Magnitude Bode plot of the mV ADC signal.

- *Record checkbox* [top]: used to export data to a `.mat` file, containing measurement data and GUI settings. After unchecking, the data is saved under the name given in the text inputbox.
- *Sound checkbox* [top]: enable/disable sound.
- *Gain* [top]: adapt gain of PGA (1,2,5,10,20,50,100,200).
- *Labels*:
  - *Data rate*: input data stream in samples per second.
  - *Total gain*: preamplifier gain multiplied by PGA gain.
  - *Measure range*: ADC saturation levels ($0 \sim 3.3\,\mathrm{V}$) divided by the total gain.
- *Enable BP checkbox*: Enable software band-pass filter, result plotted in first graph.
- *Event checkbox*: The checking and unchecking times will be saved and included in the exported `.mat` file. Can be used to mark certain events.
- *Stimulator control*: See Chapter 3.
  - *Radio buttons*: V or mA stimulation mode.
  - *Amplitude*: Specify total V or mA.
  - *PW [uS]*: Applied pulse width in µs.
  - *Inter [uS]*: Interval between two consecutive pulses in µs.
  - *STIM button*: Apply stimulus.

Thread 3 - Playing sound The last thread of the host software is responsible for the sound. The received input of the data stream is copied to the sound buffer at 20 kHz and played. Commercial amplifiers have similar features, which are helpful during microneurographic recordings to verify correct electrode placement. If noise is present, a characteristic 50 Hz tone can be heard. If APs are recorded, every single AP produces a ticking sound (an AP contains relative high frequencies). The latter would imply that the electrode is placed close to an axon.

Figure 2.31: *Graphical user interface* (GUI) created using the `Qt` framework. The GUI communicates using the enhanced communication protocol over the VCP. Here, no (microneurography) electrodes are connected to the preamplifier; the setup is measuring noise.

2.3 System validation

Before we performed *in-vivo* microneurographic recordings, we validated the different components of our setup. Since the frequency-versus-gain plot and the CMRR are crucial for a working setup for microneurography, we focused on these aspects during the validation. For this purpose, we made use of artificial (amplitude- and frequency-varying) sinusoids that could be generated by the main amplifier.

Although we started the design phase with the preamplifier, we first validated the main amplifier. To successfully verify the performance of the preamplifier, a well-understood and correct performing main amplifier was required. The validation of the preamplifier v1.0 will not be addressed any further, since in Section 2.2.4.3 we included a prior validation and its limitations.

2.3.1 Main amplifier

The preamplifier input processing stage is the most crucial element of the main amplifier. We powered the main amplifier – without the preamplifier attached – and created a voltage divider (as shown in Figure 2.32 and 2.33) that was connected to the main amplifier's validation DAC and one of the input channels. Using this circuit, $V_{virt} > 0\,\text{V}$; which is a requirement for the proper functioning of the main amplifier's IA.

In this divider, $V_{signal} > V_{virt}$ if $V_{in} \neq 0\,\text{V}$. In other words, V_{out} (after the IA stage of Figure 2.23) will always be above the V_{offset} voltage for a non-negative DC V_{vin} voltage. The main amplifier's HPF removes the DC voltage, such that V_{out} was centered around V_{offset}.

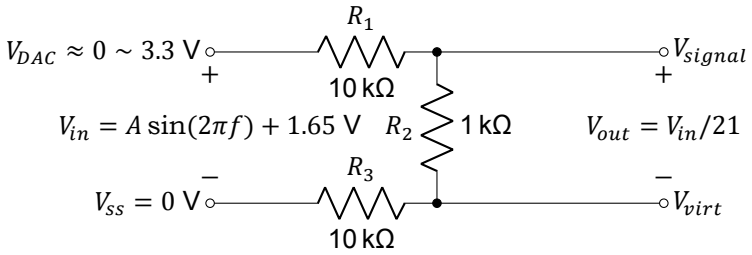

Figure 2.32: Voltage divider used for the main amplifier validation, where amplitude $A \in (-1.65\,\text{V}, 1.65\,\text{V})$ and f the frequency in Hz.

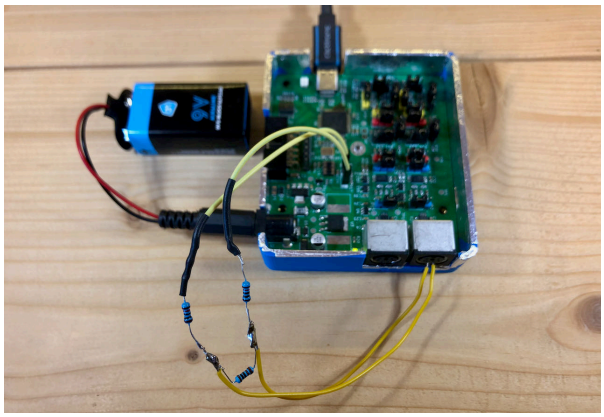

Figure 2.33: Setup including the voltage divider from Figure 2.32. This setup was used to validate the main amplifier's input processing stage. The input of the voltage divider was connected to the main amplifier's DAC. The output of divider to the V_{signal} and V_{virt} terminals of the IA.

We implemented a frequency sweep (consisting of 100 logarithmically divided frequencies) between 10 Hz and 10 kHz, using the main amplifier's internal 12-bit DAC with an amplitude of 500 mV. Each frequency was applied for $50 \cdot 1/freq$ seconds, or 50 periods. The voltage divider from Figure 2.32 reduced this amplitude by 21 V/V. We set the cutoff frequency f_c of the HPF at 50 Hz and of the LPF at 5000 Hz. We set the PGA gain at 50 V/V. After sampling, we obtained the ADC voltages as we show in Figure 2.34. From this figure, it is clear that specific frequencies were amplified.

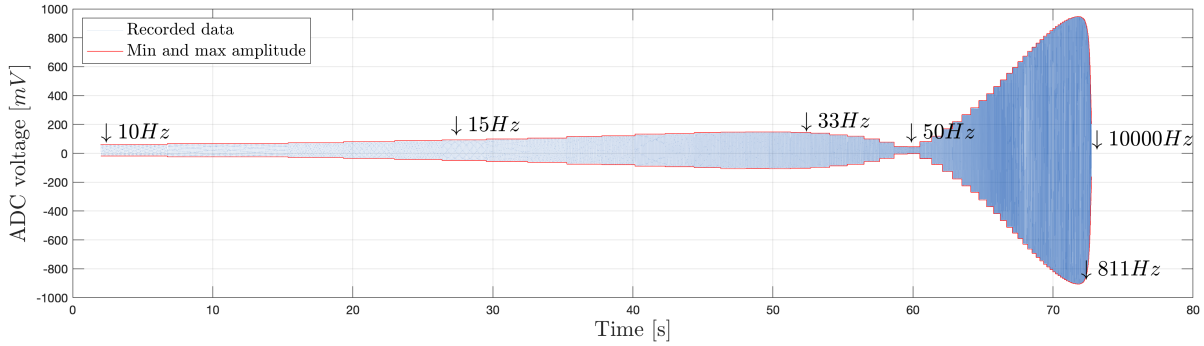

Figure 2.34: ADC readings for a frequency sweep validation signal between 10 Hz and 10 kHz.

Theoretical versus realized Bode plot Using the frequency sweep as shown in Figure 2.34, we were able to determine the magnitude Bode plot of the realized main amplifier hardware. We divided the observed ADC voltage amplitude for a specific frequency by the applied validation amplitude after the voltage divider.

We theoretically implemented the main amplifier input processing filter (Figure 2.23) to obtain a Bode plot as shown in Figure 2.35. The theoretical results show a second-order roll-off (−40 dB/decade) above cutoff frequencies f_c of the HPF and the LPF. Furthermore, the effect of the notch filter was visible around 50 Hz. The PGA gain was set at 50 V/V. In this figure, the observed gain using the frequency sweep is shown for both HPF cutoff frequencies (50 Hz and 500 Hz) and both LPF cutoff frequencies (500 Hz and 2500 Hz). These results correspond to the theoretical filter design. Notice three things: 1) The gain around 1 kHz in Figure 2.35a was around 33.75 dB ≈ 50 V/V, which corresponds to the selected gain of PGA. 2) The observed notch filter cutoff frequency seemed to be > 50 Hz (to be addressed at a later point). 3) In Figure 2.35a, the gain below 100 Hz saturated at ≈ -10 dB. At these frequencies, the maximum and minimum of the observed ADC voltage were at the level of the main amplifier's (background) noise. In other words, in this region, the noise level was larger than the amplified validation input signal.

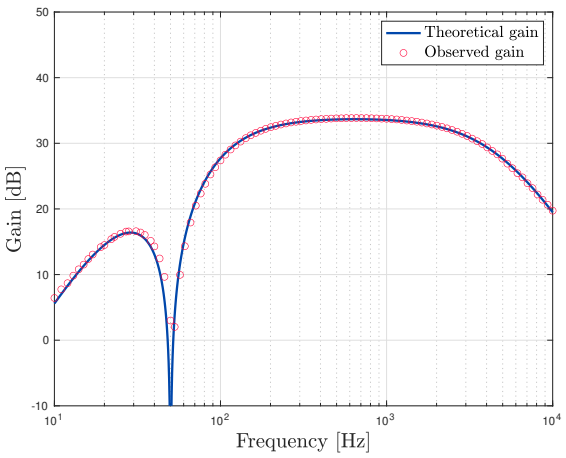

(a) HPF cutoff at 50 Hz and LPF cutoff at 5000 Hz.

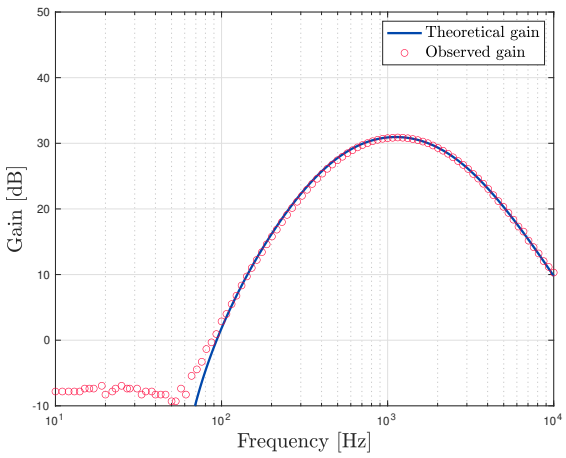

(b) HPF cutoff at 500 Hz and LPF cutoff at 2500 Hz.

Figure 2.35: Theoretical versus realized Bode plots of the main amplifier including a notch filter (cutoff at 50 Hz).

Noise caused by USB The main amplifier was connected to the PC by an USB cable. Therefore, the ground of the main amplifier was connected to the ground of the PC – introducing additional noise to the main amplifier's ground. To prevent ground loops, we added a USB isolator between the PC and the main amplifier. The results showed a decrease in noise.

2.3.2 Preamplifier v2.0

We validated the preamplifier using similar methods as for the main amplifier's validation. The setup is shown in Figure 2.36.

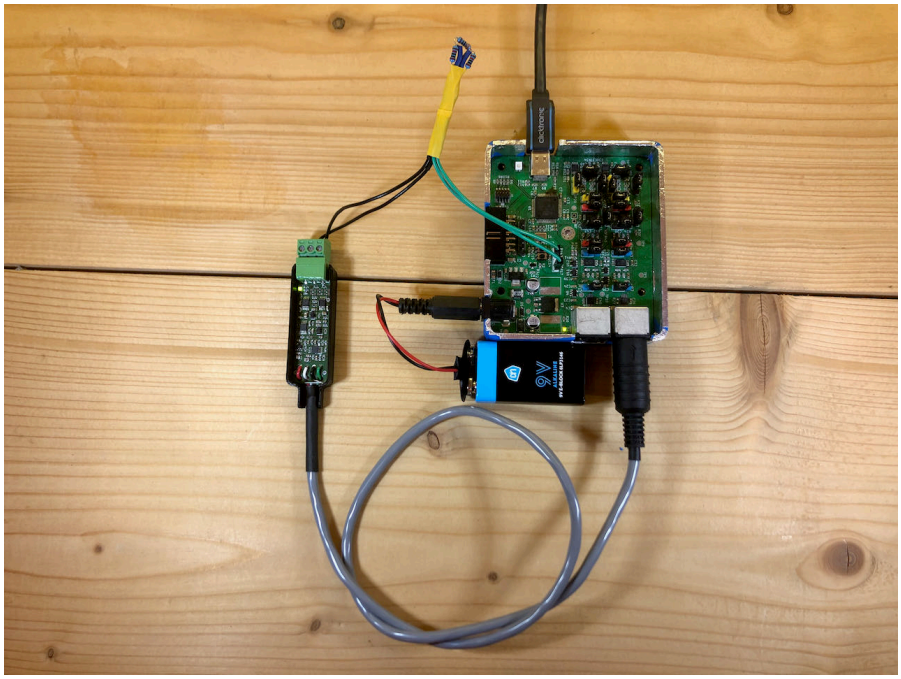

Figure 2.36: Setup including the voltage divider from Figure 2.32 using $R_1 = R_3 = 20\,\text{k}\Omega$ and $R_2 = 330\,\text{k}\Omega$. The divider was connected to the main amplifier's DAC (shown on the right) and to the input terminals of the preamplifier (shown on the left). This setup was used to validate the preamplifier.

Theoretical versus realized Bode plot We performed a similar frequency sweep as we did for the main amplifier to validate the preamplifier. We connected the preamplifier to the main amplifier, disabled the main amplifier's HPF and LPF, set the PGA gain at 1 V/V and set the validation signal's amplitude to 50 mV. We adapted the resistors of the voltage divider from Figure 2.32 to $R_1 = R_3 = 20\,\text{k}\Omega$ and $R_2 = 330\,\text{k}\Omega$, resulting in a 1:122 ratio. Figure 2.37 shows the observed gain between 10 Hz and 10 kHz, which corresponded to the theoretical design. Around 2.5 kHz, the gain was 71.5 dB $\approx$ 3750 V/V. However, for frequencies below 100 Hz, it seemed that the gain was around 40 dB $\approx$ 100 V/V. Again, this was a result of the noise that causes non-zero maximum and minimum amplitudes (values of 50 mV are observed) of the ADC readings. In other words, the level of the noise was again larger than the amplified validation input signal.

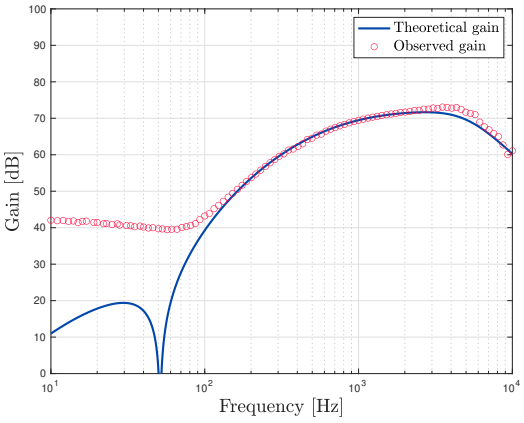

Figure 2.37: Theoretical versus realized Bode plot of the preamplifier. HPF cutoff at 500 Hz, LPF cutoff at 5000 Hz, and notch filter cutoff at 50 Hz.

Driven right leg circuit To minimize the effect of PLI on our setup, we included a driven right leg circuit in the design. The common-mode voltage was monitored and mirrored around the reference voltage and driven back to the body. To validate this circuit, we placed the L_{nerve} and L_{ref} leads in gelatin, as illustrated in Figure 2.38.

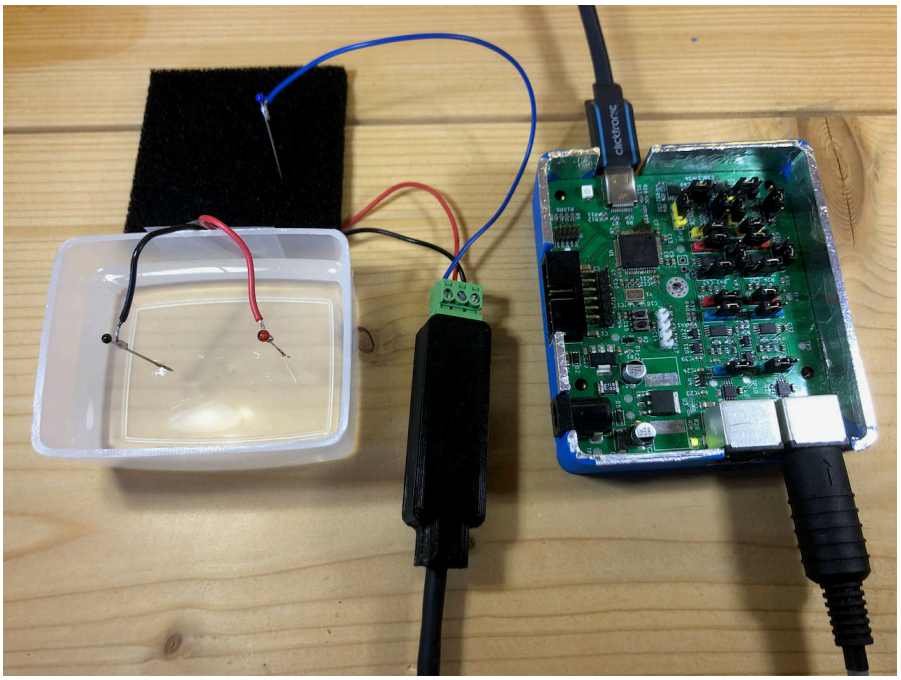

Figure 2.38: Setup to test performance of the DRL circuit. On the left, the plastic container was filled with gelatin. The red and black wires represent the L_{nerve} and L_{ref} leads. The blue wire can be placed in the gelatin, activating the DRL circuit. In this picture, the DRL circuit was not activated, resulting in the ADC voltages shown in Figure 2.39a. The preamplifier (v2.0) is shown in the middle, on the right is the main amplifier.

The recordings without and with the connected DRL electrode are shown in Figures 2.39a and 2.39b respectively, while the frequency amplitude spectrum plots are shown in Figure 2.40. These results reveal that the PLI of 50 Hz, including its harmonics, were suppressed after using the DRL circuit. Furthermore, Figure 2.40b shows that the 50 Hz was inhibited, while its harmonics were present. This can be explained by the preamplifier's notch filter of 50 Hz.

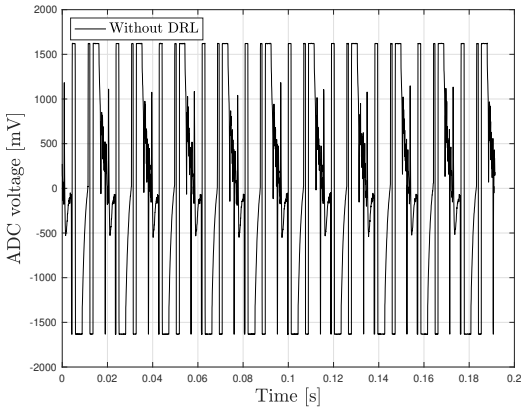

(a) Without DRL lead attached.

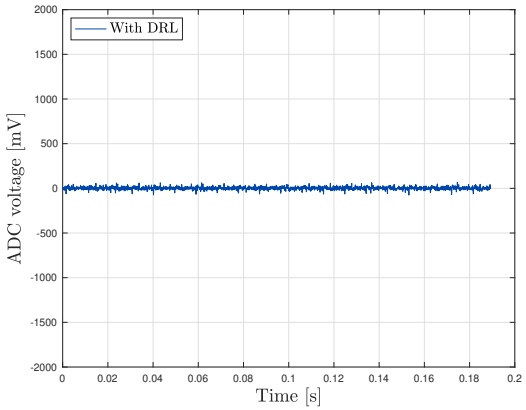

(b) With DRL lead attached.

Figure 2.39: Raw ADC voltages for the setup shown in Figure 2.38. The gain of the PGA was set at 1 V/V. These figures show an amplitude decrease from ≈ 1500 mV to 50 mV using the DRL electrode.

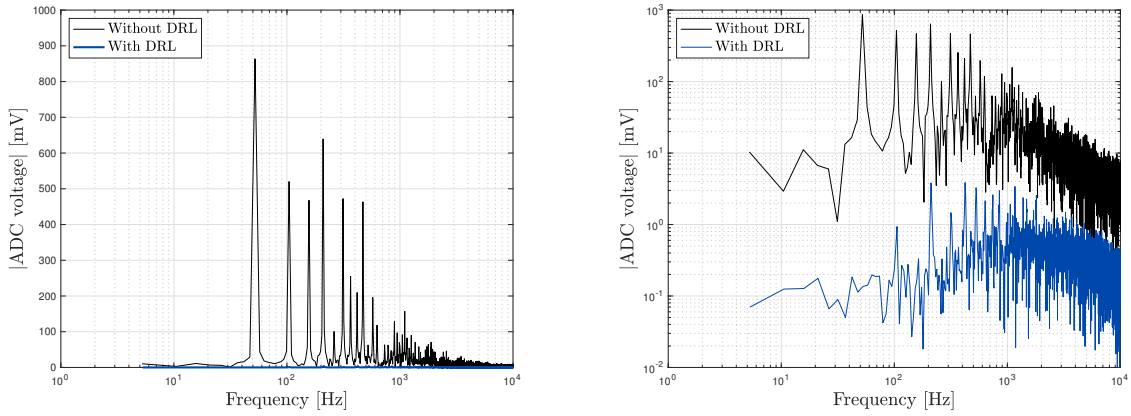

(a) Amplitude spectrum on a linear y-scale.

(b) Amplitude spectrum on a logarithmic y-scale.

Figure 2.40: Amplitude spectrum of the signals from Figure 2.39. These results show that the PLI of 50 Hz and its harmonics are minimized.

Faraday cage During trials for measurement of neural signals in the axon of a lugworm (will be discussed further in Section 2.4), we still measured some 50 Hz harmonics, although the DRL method was performing well to reject PLI. Therefore, as shown in Figure 2.41, we have built a Faraday cage that should block all electromagnetic fields in order to increase the EMI rejection performance. We grounded the cage by connecting it to the main amplifier's (isolated) ground. Small animals can fit in this cage to validate the setup during *in-vivo* experiments. Figure 2.42 shows the reduced measured noise; the Faraday cage without using the DRL method shows the best performance in terms of EMI rejection.

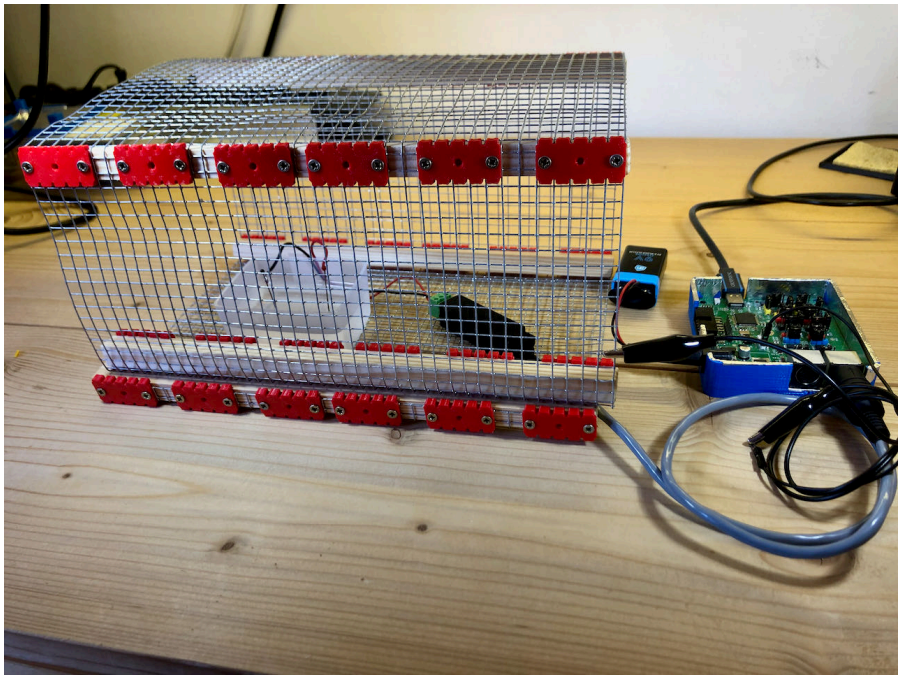

Figure 2.41: Setup including the Faraday cage. The container with gelatin was placed inside the cage and the cage was connected to the (isolated) main amplifier's ground.

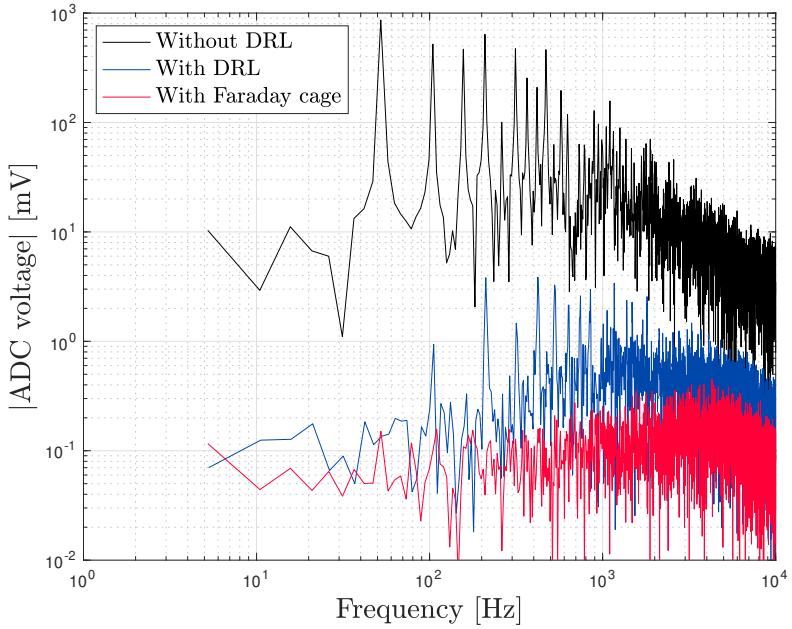

Figure 2.42: Amplitude spectrum of the signals from Figure 2.39 and also using the setup including the Faraday cage, as shown in Figure 2.41.

2.4 In-vivo experiments

In this section, we have used our neural signal amplifier for microneurographic recordings *in-vivo*. We performed several *in-vivo* experiments on lugworms and rats, as illustrated by the timeline in Figure 2.43. First, we tested the preamplifier v1.0 using an anesthetized rat. Due to the leads-off detection, this amplifier was unusable for microneurographic recordings; therefore, we will not discuss this experiment in further detail. For the first rat experiment, we used the updated preamplifier v2.0 and observed a stimulus artifact. Before performing the second rat experiment, we applied our setup to a lugworm, including the Faraday cage. These results were promising, and finally, we were able to measure APs during the second rat experiment.

In the following sections, we will discuss the experiments performed on lugworms to capture neural behavior. After that, we will discuss the experiments that were performed using rats.

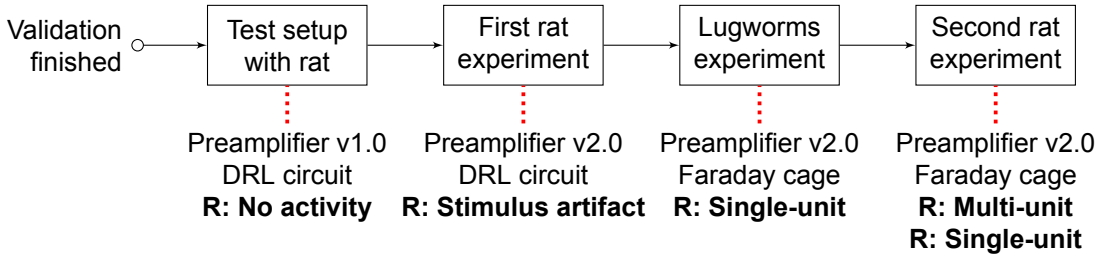

Figure 2.43: *In-vivo* experiments timeline.

2.4.1 Measurements in lugworms

2.4.1.1 Anatomy

Lugworms are large marine organisms (Figure 2.44a) and are often used as bait for sport fishing. In Figure 2.44b, we show their anatomy: lugworms have a ventral nerve cord that runs along the length of their body.

(a) A lugworm in its natural habitat [72].

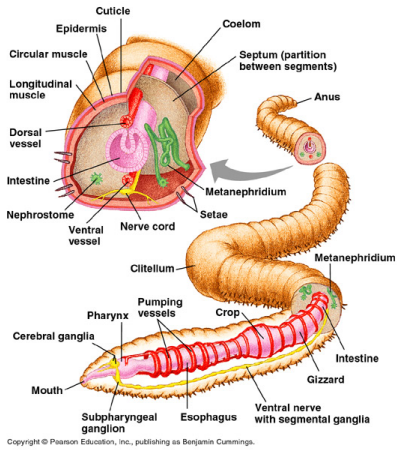

(b) The anatomy of a lugworm, notice the ventral nerve cord that runs along the length of the body [73].

Figure 2.44: Lugworm.

2.4.1.2 Setup overview

We punctured the ventral nerve cord of a lugworm using two needles and placed the lugworm inside the Faraday cage. Then, we used a (wooden, non-conductive) chopstick to touch the worm to provoke APs. To limit any environmental noise, a Faraday cage (without using the DRL circuit) was used. According to Figure 2.42, this setup was optimal to limit noise from EMI. The gain of the main amplifier was set at 20 V/V, resulting in an overall gain (main amplifier and preamplifier) of $\approx 82\,000$ V/V or ≈ 98.3 dB. We

sampled at 20 kHz and used the setup's sound output to help placing the needles correctly. Figure 2.45 shows this setup, including the lugworm, the preamplifier, and the Faraday cage.

Figure 2.45: Setup overview to measure APs in a lugworm. The needles were placed inside the ventral nerve cord and connected to the preamplifier. The lugworm was placed inside the Faraday cage. A wooden chopstick to provoke APs is shown on the left.

2.4.1.3 Results

Background activity After placing the needles, we recorded neural background activity in the ventral nerve cord of the lugworm. During these measurements, we were not touching the lugworm. Figure 2.46a shows the recorded background activity, where many spontaneous individual APs can be observed. The amplitudes of the APs are not equal; some smaller and larger spikes can be identified.

To validate the size and shape of single APs, we attempted to create an averaged AP. To do so, we select all spikes that are above 5 µV. Sometimes APs are measured in rapid succession, which are difficult to compare to a single AP. We ignored all APs that have another AP within an interval of 10 ms. This resulted in 89 selected APs, as shown in Figure 2.46a.

We show the overlay of these spikes in Figure 2.46c. The averaged AP is around 1 ms in duration and has an amplitude between −10 and 10 µV. These values are comparable to literature findings [55].

Chopstick evoked activity We pressed gently on the lugworm using the wooden chopstick shown in Figure 2.45, with a frequency of ≈ 1 Hz. The raw data recording is shown in Figure 2.46b. By comparing these data to the neural background activity (Figure 2.46a), it can be seen that a neural AP train is repeated with a frequency of 1 Hz.

Again, we selected spikes above 5 µV and not followed by another spike within 10 ms, to determine the averaged AP. The result is shown in Figure 2.46d. Although the averaged AP differs from the background activity spike (Figure 2.46c), a clear pattern can be identified.

2.4.1.4 Remarks

Despite the fact that the overlay plots of the background activity and chopstick evoked activity are different, the raw data plots clearly show the individual spikes. However, placing the needles at random in the lugworms was often not successful. Careful needle placement (close to the ventral nerve cord) was required to record APs.

We used non-isolated needles, which record the activity from many (smaller) axons simultaneously (see Section 2.1.2). However, we were able to discriminate single APs easily, a topic that we address further in the discussion.

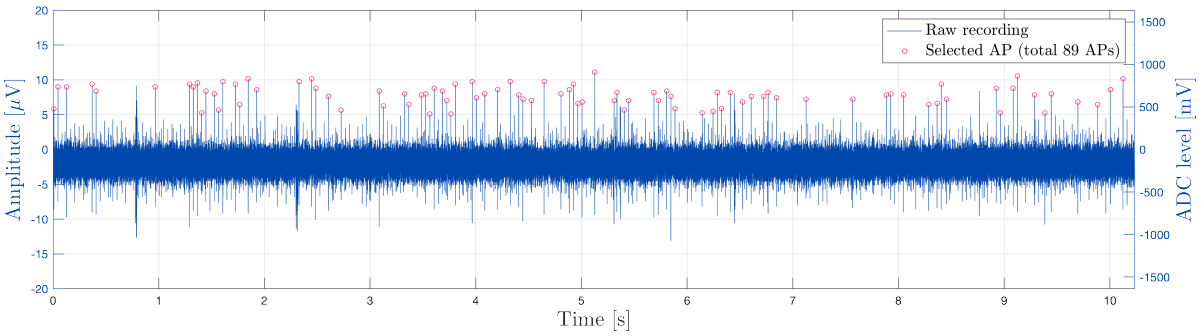

(a) Raw microneurographic recordings in a ventral nerve cord of a lugworm. The measurements were performed for 10 s, with the measured potential shown on the left axis in µV. The axis on the right indicates the sampled ADC voltage. The ADC-stage saturates at −1650 and 1650 mV.

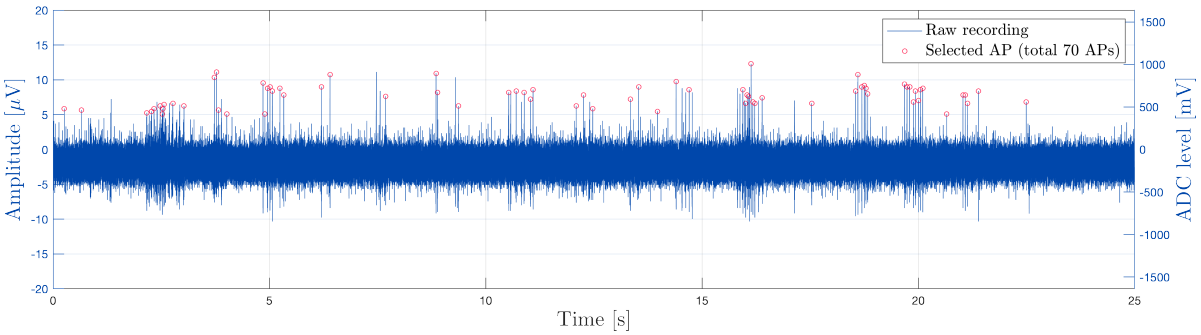

(b) Raw microneurographic recordings in a ventral nerve cord of a lugworm during gentle touches with a chopstick at 1 Hz. The measurements were performed for 10 s, with the measured potential shown on the left axis in µV. The axis on the right indicates the sampled ADC voltage. The ADC-stage saturates at −1650 and 1650 mV.

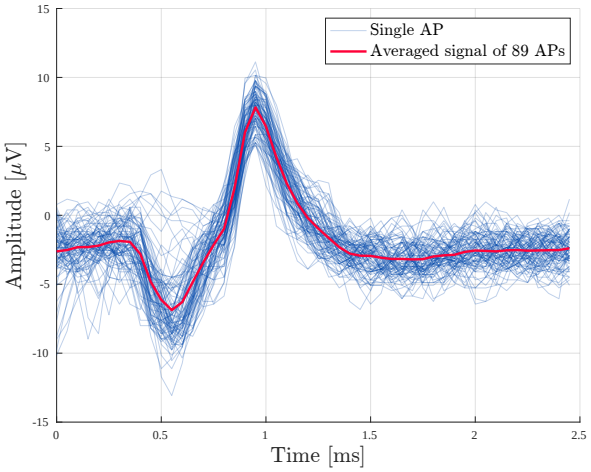

(c) The averaged AP of the single APs in Figure 2.46a.

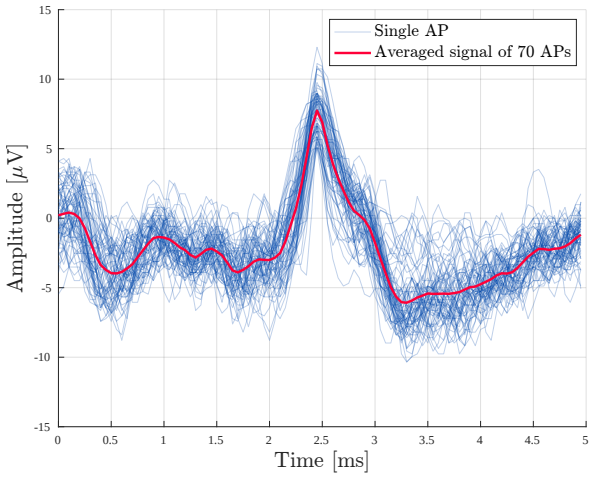

(d) The averaged AP of the single APs – evoked with a chopstick – in Figure 2.46b.

Figure 2.46: Results of microneurographic recordings in the ventral nerve cord of a lugworm.

2.4.2 Measurements in rats

We performed two experiments on rats, a few weeks apart. The results from the first rat experiment were studied and used to improve the setup for the second rat experiment.

All recordings on rats were conducted at the LUMC animal facility, in a controlled laboratory environment. The experiments were conducted on anesthetized (Temgesic + Isoflurane; 0.05 mg/kg buprenorphine/ 5% induction, 2% maintenance isoflurane) adult *Sprague-Dawley rats* (female or male, 10-12 weeks old) in accordance with national- and EU regulations regarding animal care (*LUMC*, `AVD1160020171627`). Animals were housed in a temperature- and humidity-controlled environment with a light/ dark cycle of 12 h:12 h, and free access to food and water. Every attempt was made to minimize the number of animals used, as well as their pain and discomfort.

2.4.2.1 Anatomy

The *Sprague-Dawley rats* were anesthetized and the sciatic nerve was exposed, which is frequently used for microneurographic recordings [74]. The sciatic nerve runs down the lower part of the leg, and is the longest and widest nerve of a rat. It connects the spinal cord and brain with the skin and muscles of the thigh and leg, and is therefore responsible for the innervation and control of the skin and musculature of the lower leg and foot. Vice versa, it transfers sensory information from the skin of the foot and lower leg musculature to the spinal cord and brain. Figure 2.47 shows the rat in experimental setup during our experiments, with the sciatic nerve exposed.

(a) Anesthetized rat, sciatic nerve of right leg is exposed.

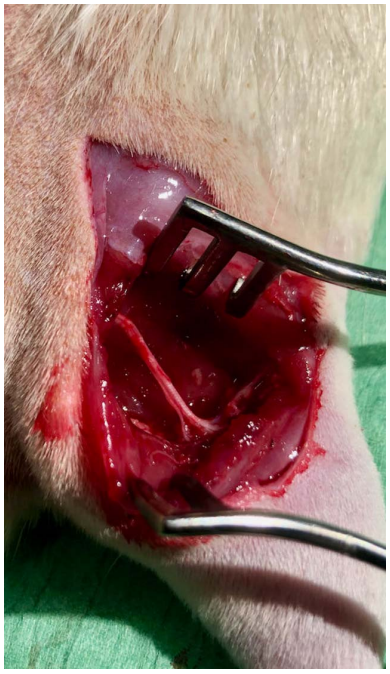

(b) Sciatic nerve including shaved skin.

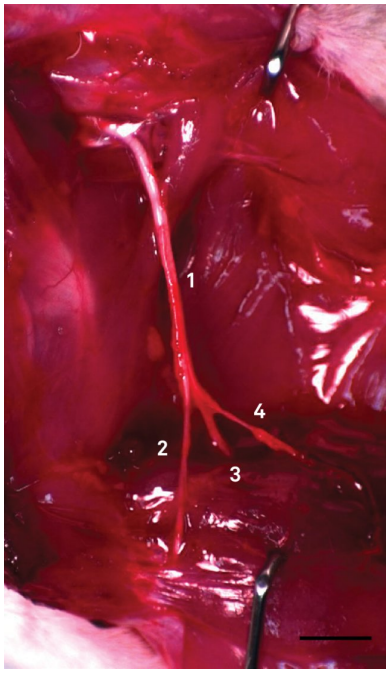

(c) Sciatic nerve in detail. 1, sciatic nerve; 2, common fibular nerve; 3, tibial nerve; 4, sural nerve. Bar = 8 mm [75].

Figure 2.47: Sciatic nerve anatomy of a Sprague-Dawley rat.

The entire sciatic nerve at midthigh is composed of about 27 000 axons. Of these axons, 6% are myelinated motor axons, 23% myelinated and 48% unmyelinated sensory axons, and 23% unmyelinated sympathetic axons [76]. Hence, the sciatic nerve contains a large number of unmyelinated axons, which are thinner than myelinated axons (Section 2.1.1).

2.4.2.2 Setup overview - first experiment

For the first experiment, we used two reference electrodes, namely, electrodes that do not have an isolated shield. By doing so, we increased the probability of picking up any activity from axons in the vicinity of the electrode. We placed one (isolated) microneurography electrode into the sciatic nerve, and the second (non-isolated) electrode into the surrounding tissue, such as connective tissue, as we show in Figure 2.49. To improve the CMRR, the DRL circuit was used. The DRL electrode was connected using a disposable electrode. Figure 2.48 shows an isolated (single-unit) and non-isolated (multi-unit) electrode.

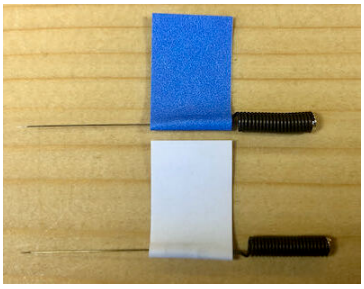

Figure 2.48: Microneurography electrodes. White tab: isolated (single-unit), blue tab: non-isolated (multi-unit).

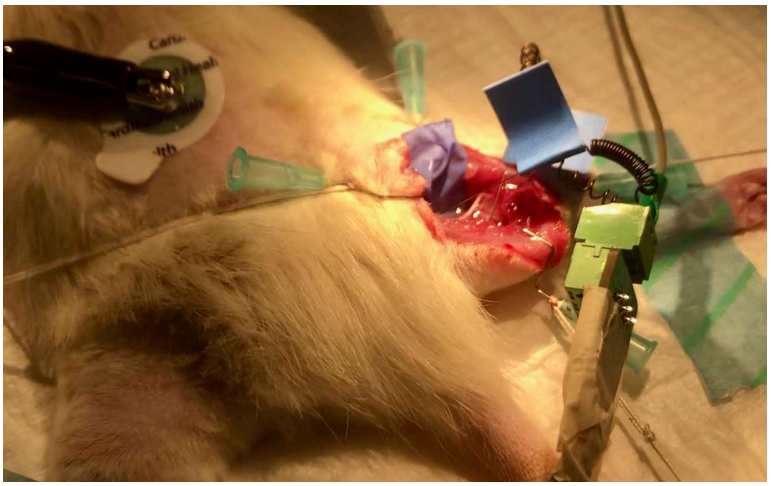

(a) The disposable DRL electrode is shown on the top left and the preamplifier on the bottom right.

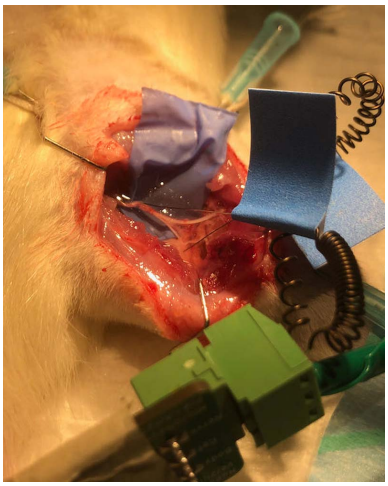

(b) Two reference electrodes: one placed in the sciatic nerve and one in the surrounding tissue.

Figure 2.49: Overview of the setup of the first rat experiment.

2.4.2.3 Results - first experiment

During these experiments, no background neural activity was observed. To provoke APs, we stimulated the right leg by slightly scratching the skin with the terminals of a 9 V battery. Figure 2.50 shows the results of the provoked APs. We selected APs above 50 µV and with a minimal spacing of 10 ms to create an overlay as shown in Figure 2.51.

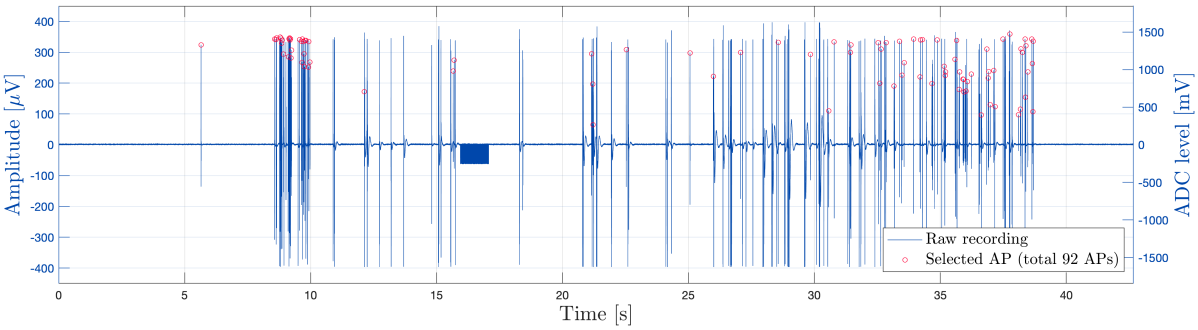

Figure 2.50: Raw microneurographic recordings. The measurements were performed for 40 s, with the measured potential shown on the left axis in µV. The axis on the right indicates the sampled ADC voltage. The ADC-stage saturates at −1650 and 1650 mV.

2.4.2.4 Remarks - first experiment

Although the results from Figure 2.50 looked promising, the averaged spike from Figure 2.51 shows some extraordinary characteristics. Firstly, the amplitude is in the order of 300 µV, which was much bigger than an expected AP measured using microneurography (0-10 µV). Secondly, the spikes can only be initiated by using a 9 V battery; no spontaneous AP detection was present. Third, the observed spikes were also provoked by stimulation of other parts of the rat, e.g., left leg or back using the 9 V battery terminals. As such, these spikes were classified as stimulus artifacts, which is often seen during experiments where an electrical stimulus is used to evoke APs [77]. Furthermore, the recordings within the −25 µV to 25 µV range were dominated by background noise caused by EMI. This led to an improved setup to reject this interference further.

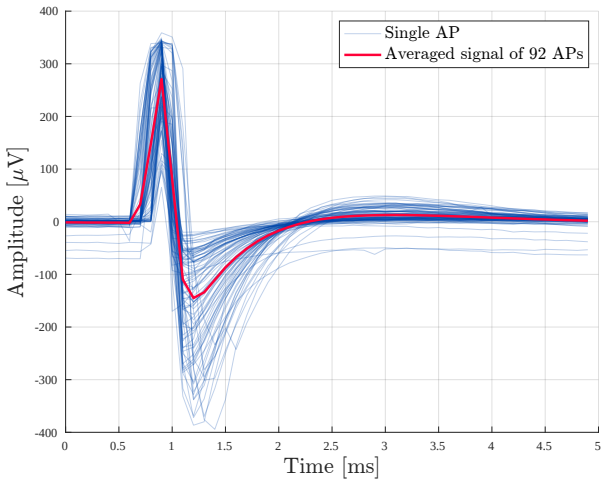

Figure 2.51: The averaged of the single spikes in Figure 2.50.

2.4.2.5 Setup overview - second experiment

Sufficient noise reduction is essential for successful microneurography. Therefore, we applied a Faraday cage (see noise levels in Figure 2.42) for the second experiment. Using this setup, we could focus on the −20 to 20 µV interval; this is the range where we expected to measure APs using microneurography (see Section 2.4.1.3 for APs in worms).

In Figure 2.52, the setup for the second experiment is shown. As mentioned, the anesthetized rat was placed inside the Faraday cage. Like in the previous experiment, to increase the chance of picking up nerve activity, two reference electrodes were used. These electrodes can pick up any activity from an axon in the vicinity of the entire electrode.

Figure 2.52: Setup overview for the second experiment. The rat was placed inside the Faraday cage. Two reference electrodes were used: one is placed in the sciatic nerve and one inside the surrounding tissue.

We performed background neural activity measurements in both legs (in Figure 2.52, the right sciatic nerve is exposed). Furthermore, the activity was recorded while the leg was slightly touched with a cotton swab with a frequency of ≈ 1 Hz, as shown in Figure 2.53. The electrodes were readjusted repeatedly until a signal was picked up by the electrodes.

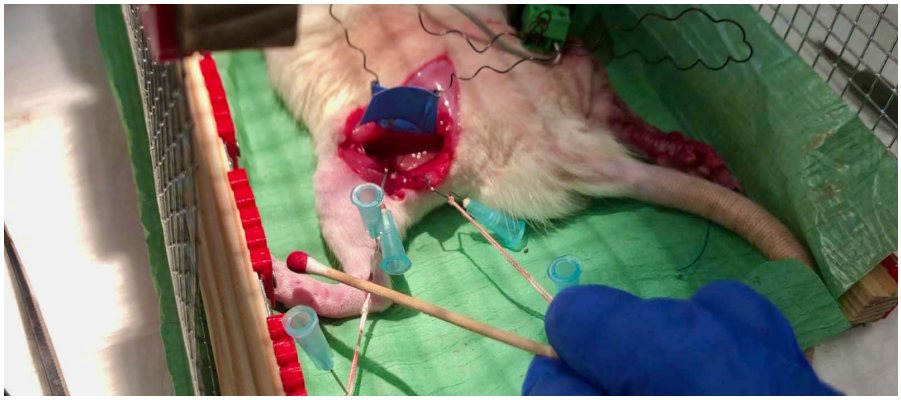

Figure 2.53: Recording of neural activity using microneurography in the left sciatic nerve of a rat. The left leg was slightly touched with a cotton swab at ≈ 1 Hz.

2.4.2.6 Results - second experiment (multi-unit recording)

The comparison of Figure 2.54a to Figure 2.54b shows that we were able to record activity of multiple axons. In Figure 2.54a the rat was not stimulated: The signal mainly consisted of noise, with many smaller spikes superimposed to the noise level. In Figure 2.54b, the paw of the rat was pressed multiple times with a cotton swap. This repetitive pattern resulted in an alternating level of the multiple axon's (multi-unit) activity, which was clearly visible by repetitive blocks of spikes occurring in the frequency of stimulation.

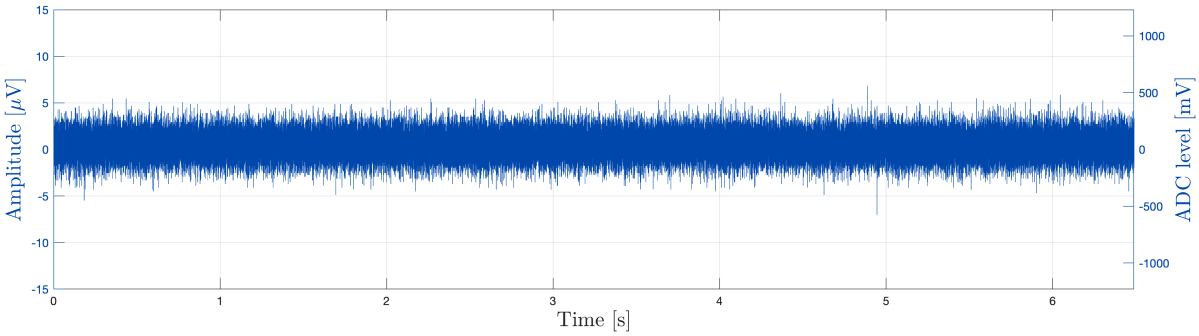

(a) Background activity. Although the majority looks like noise, many (smaller) sharp spikes can be seen. In contrast to the noise level, this is difficult to discriminate.

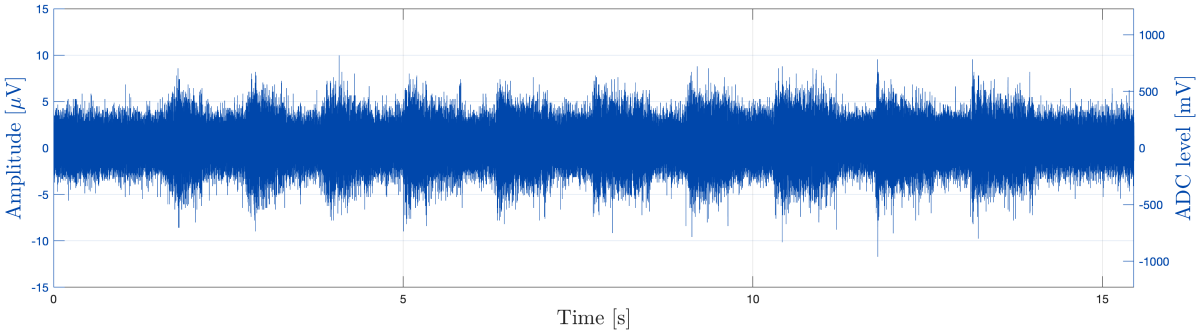

(b) Cotton swab evoked activity (Figure 2.53). A repetitive pattern at 1 Hz can be observed.

Figure 2.54: Raw recordings of the second experiment. The rat was placed in the Faraday cage and two reference electrodes were used for the recordings. The measured potential is shown on the left axis in µV. The axis on the right indicates the sampled ADC voltage, the ADC-stage saturates at −1650 and 1650 mV.

2.4.2.7 Results - second experiment (single-unit recording)

For the final experiment, we used a single-unit microneurography electrode (discussed in Section 2.1.2). Even though it was challenging to record activity with this electrode (since the non-isolated tip was extremely small and only measures very local potentials, the success of these recordings was highly depending on correct needle placement) a few APs were obtained. The needle was replaced multiple times in the sciatic nerve (Figure 2.55b), and after some trials, successful recordings were obtained as shown in Figure 2.55a. The average of the spikes (Figure 2.55c) looks like an AP from an unmyelinated C axon [57].

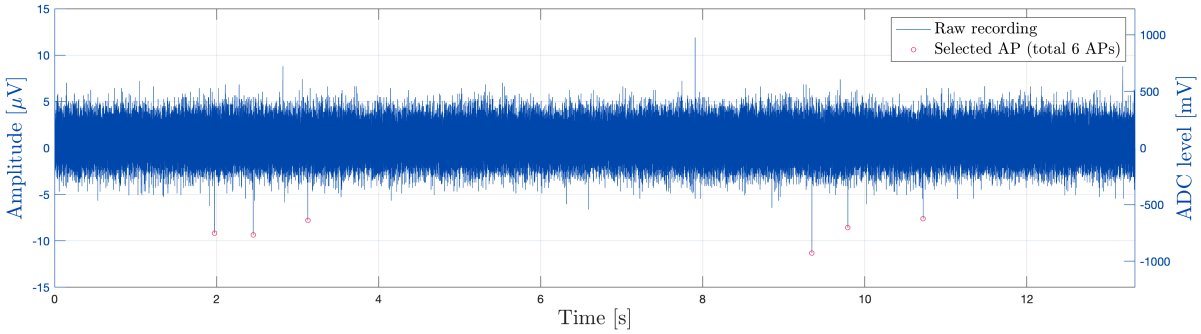

(a) Raw recordings of the second experiment. The measured potential is shown on the left axis in µV. The axis on the right indicates the sampled ADC voltage, the ADC-stage saturates at −1650 and 1650 mV.

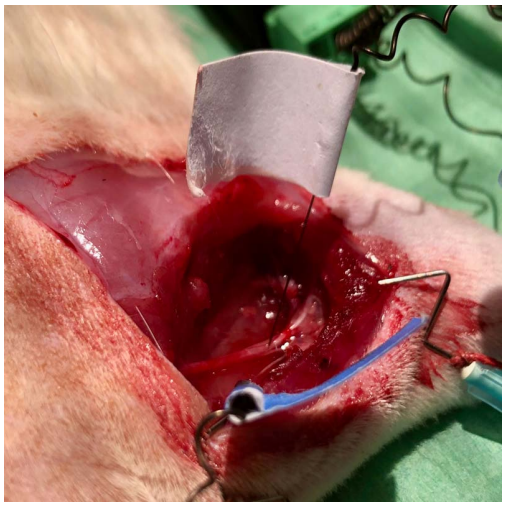

(b) Placement of the single-unit microneurography electrode in the sciatic nerve.

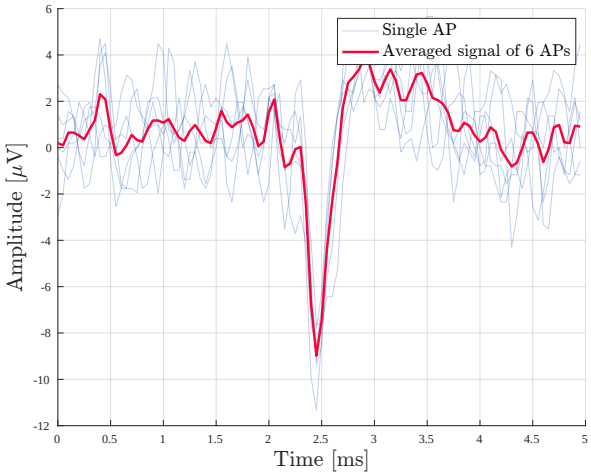

(c) Mean AP of the APs shown in Figure 2.55a.

Figure 2.55: Results of microneurographic recordings in the sciatic nerve of a rat using a single-unit electrode. The Faraday cage was used to limit the interference.

2.5 Discussion

Here we introduced the design requirements for a successful neural amplifier for microneurography. Additionally, we elaborated on the design of our hardware step-by-step. The system was validated *in-vivo* on lugworms and in rats, APs were recorded. The design requirements, validation, and results of the *in-vivo* study are discussed here. We conclude with recommendations for (future) hardware improvements.

2.5.1 Amplifier's gain

Microneurographic signals are in the order of tens of µV. To amplify these signals to the hundredths of mV range, a large gain of $A_v \approx 20\,000\,\mathrm{V/V}$ is required. Using the preamplifier's gain and the main amplifier's PGA gain, we were capable of creating a gain ranging between 4098 V/V and 819 650 V/V, which was (software) selectable in several steps. Using these different gains, the neural signal could be amplified such that the maximum range of ADC stage was used. The maximum gain exceeds the necessary requirements for microneurographic purposes.

2.5.2 Too much bandwidth

In Section 2.1.5, we defined the design requirement for the bandwidth of our neural signal amplifier: 500 Hz to 5000 Hz. In this frequency range, microneurographic signals are present. In our first designs, we implemented a HPF on the preamplifier with a cutoff frequency of 5 Hz instead of 500 Hz. Using this wide bandwidth, all available information was amplified. Potential bandwidth narrowing methods (additional filtering) could be implemented using analog filters (on the main amplifier), or in the digital domain. In this enlarge bandwidth range, however, movement (artifacts) and other (non-neural) activities were observed. We observed that the amplifier became saturated which resulted in unsuccessful microneurographic recordings. Therefore, we adapted the HPF's cutoff frequency to 500 Hz. This is an indication that a larger bandwidth does not necessarily lead to better results. According to the results, a bandwidth between 500 Hz and 5000 Hz seems appropriate for microneurographic recordings.

2.5.3 Interference rejection

We elaborated on several EMI rejection techniques. Firstly, we implemented a DRL circuit that actively steers the common-mode voltage towards a specified level. This technique resulted in suppression of the 50 Hz PLI (and its harmonics), as we showed in Figure 2.39. Without a DRL circuit, the noise (after amplification) saturated the ADC stage. Including the DRL circuit, the noise level at the ADC stage decreased to several mV. We could even further improve these results by using a Faraday cage (Figure 2.42); which shielded the interior from external EMI.

A combination of the Faraday cage and the DRL circuit did not lower the noise levels further, to the contrary. The combination of both techniques resulted in similar EMI reduction levels as when only the DRL circuit was used. We hypothesize that a DRL lead can also pick up environmental noise. Additionally, the DRL circuit potentially introduced additional noise to the Faraday cage. Therefore, we did not use the DRL circuit in combination with the Faraday cage. However, this is a crucial assessment in the situation that the microneurography target (e.g., a human) does not fit within the Faraday cage. The DRL method by itself may not be sufficient to suppress interference to perform microneurography successfully.

2.5.4 Digitization and real-time data visualization

The 14-bit ADC resolution design requirement appeared to be more than sufficient for microneurographic recordings. Sampling data at high frequency rates (including oversampling to increase resolution), and implementing an embedded driver and a host driver to communicate the digitized values at 20 000 samples per second, was challenging. Although, by making use of the `Python` package `Numba`, the host side driver was optimized. Moreover, the use of different threads (for specific tasks) resulted in a smooth operating GUI that visualizes the recorded data real-time. Large amounts of data could be produced by the setup; e.g., a microneurographic recording of one minute could yield a `.mat` file of several hundredths of megabytes.

2.5.5 Recorded action potential shape

The AP's shape as recorded in unmyelinated C and myelinated $A\beta$ axons in humans are shown in Figure 2.4. By comparing these shapes to the observed APs in the ventral nerve cord of the lugworm (Figure 2.46c and Figure 2.46d), we saw several differences.

Firstly, our background recorded AP (Figure 2.46c) looks similar to the myelinated AP from Figure 2.4. However, in the lugworm, the AP is negative-going first, while the AP in a myelinated $A\beta$ axon is positive-going first. In literature, this is explained as the microelectrode tip being close to a node of Ranvier [78].

Secondly, the amplitude (in µV) of the recordings performed in lugworms (presented in Figure 2.46c and Figure 2.46d) compared to human recordings (Figure 2.4) showed amplitude differences. These differences may be explained by electrode placement (e.g., tip further away from nerve). Moreover, the gain of the preamplifier is not uniform within the bandwidth (Figure 2.35 and Figure 2.37). In software, the digitized value is converted to corresponding voltage levels at the tip of the electrode. A too large scaling factor may have been used in software that leads to a smaller electrode voltage than the actual voltage.

Thirdly, the APs evoked with a chopstick (Figure 2.46d, multiple axons were recorded after contact) showed that, besides the large peak (probably caused by some large axons, see next section), some smaller peaks were present. These smaller peaks may originate from many (smaller) axons that were not simultaneous active at the background, but were now activated simultaneously by the chopstick. Not all axons had the same conduction speed, and that may result in multiple peaks. Therefore, this activity could be classified as multi-unit activity. In this case, the observed activity looked like LFPs.

2.5.6 Lugworm's ventral nerve cord versus rat's sciatic nerve

We used lugworms and rats to test our setup and record microneurography *in-vivo*. During these experiments, we placed both isolated (single-unit) as non-isolated (multiple-unit) electrodes in (or close to) a nerve. Recordings from the lugworms using non-isolated electrodes showed clearly identifiable and separate APs (or single-unit activity), as shown in Figure 2.46. However, non-isolated electrodes used on a rat's sciatic nerve resulted in multi-unit activity (see Figure 2.54).

Looking at the cross-sectional view of the lugworm's ventral nerve (Figure 2.56b) could yield additional information. Three large axons (giant fibers) are present which play a crucial role in the worm's rapid escape responses [79] to explain this difference. These axons have a thick myelinated sheet. Placing an electrode in (or close to) the ventral nerve cord results in recording the activity mainly from these giant axons. The activity from many other smaller axons (shown below the giant axons in Figure 2.56b) is presented less prominent in the recording. Smaller axons have a smaller total transmembrane ionic current flow, and therefore, the resulting extracellular potentials differences (that can be measured using microneurography) are smaller.

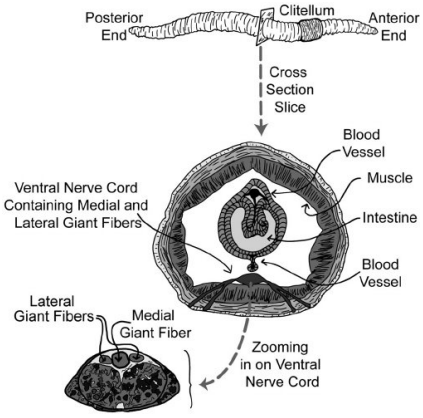

(a) Top and middle: cross-section of a worm, bottom: cross-section of the ventral nerve cord [80].

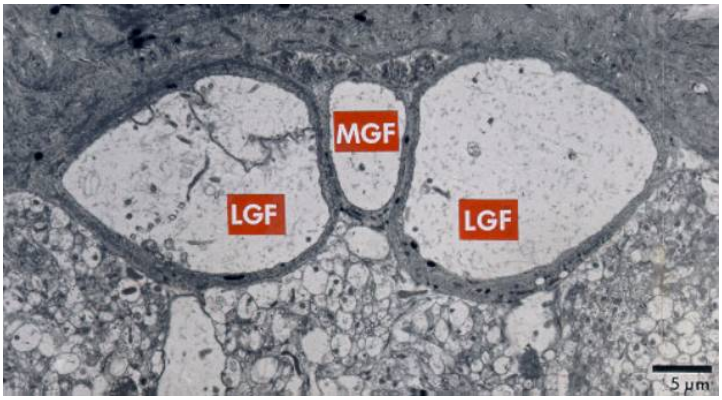

(b) Cross-sectional view of the upper part of the ventral nerve. Three giant axons are shown: two lateral giant fibers (LGF) and one medial giant fiber (MGF) [79].

Figure 2.56: Ventral nerve cord of a lugworm.

The sciatic nerve of a rat does not contain giant axons and contains relatively many unmyelinated axons (see Section 2.4.2.1). Placing a non-isolated electrode results in a recording of many signals

derived from varying types of axons (see Figure 2.54). Based on the above, we could classify this activity as multi-unit activity. To pick up single-unit activity, an isolated electrode (placed very close to an axon) is required. However, very accurate placement of the isolated electrode becomes essential and challenging in these circumstances and requires multiple needle adjustments before finding the right position for recording. I.e., placing the tip of the electrode in one of the connective tissue layers (Section 2.1.1) may result in a recording without any neural activity.

2.5.7 Setup improvements

Our setup was capable of recording neural activity using microneurography. However, to further improve its performance, we provide some suggestions for future hardware and software improvements.

- The data rate was set at 20 000 samples per second; however, 1 or 2% was missed due to the `Python` driver at the host. In Section 2.3.1, we validated the performance of the main amplifier. We observed that the cutoff frequency of the notch filter is not exactly at 50 Hz; it is around 52 Hz. This could be due to component tolerances, but also due to missing samples leading to a higher observed frequency. The latter could be resolved by improving the `Python` driver, or by including timing information in the data stream (see Section 2.2.7.1).
- A Faraday cage improves the noise rejection significantly (see Section 2.42). Besides shielding the lugworm or rat during *in-vivo* experiments, we could also shield the preamplifier and main amplifier by placing these hardware components in (metal) enclosures.
- We designed the GUI using the `Qt` framework, where the `PySide` package provides the bindings for `Python`. This package utilizes the CPU for running the different threads and rendering the GUI; therefore, our software demands much processing power of the CPU. Additional features may reduce the performance of the software, hence, it may be required to use the *graphics processing unit* (GPU) or different compiled programming languages (such as C/C++) for future software versions.
- During our *in-vivo* experiments, the microneurography electrodes were placed by hand. Due to the elasticity of the connecting wire, the electrode was moving slightly after placement. Moreover, precise placement of the electrode in the sciatic nerve, such that the non-isolated tip was within the nerve tissue, was extremely challenging. Therefore, a micromanipulator could be very useful to place the electrodes accurately during *in-vivo* experiments.

2.6 Conclusion

Neurophysiological signals are electrical signals generated by the nervous system. Depending on the type of stimulus and in particular pathologies, these signals are sometimes interpreted by the brain as ‘pain’. To neutralize the painful signals, we require a setup that is capable of measuring neural activity, while embedding processing power and extensions for simultaneous stimulation. We successfully developed a functional signal amplifier for microneurography with a user-friendly setup that can be applied to measure the activity in nerves. With this setup, it is potentially possible to detect pain-related activity and discriminate subthreshold oscillations and ectopic discharges that are related to neuropathic pain. Additionally, this setup could implement closed-loop algorithms that require simultaneous neural recording and stimulation. It is a first step in tackling the limitations of existing hardware and shows promising results for future development and neutralizing activity that leads to generation of NP.

3

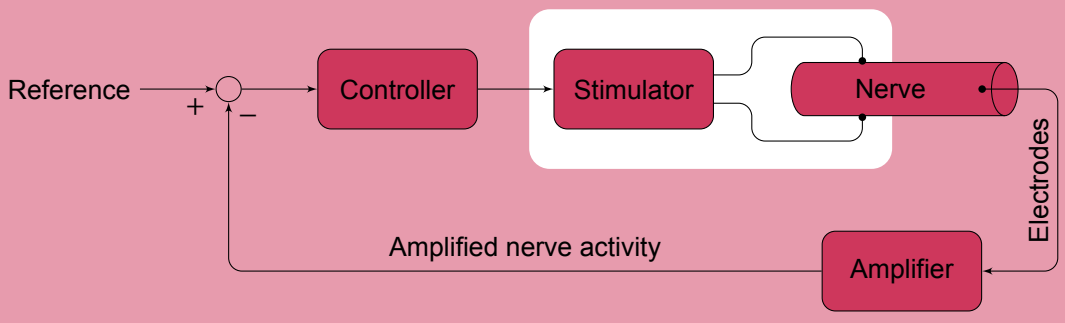
Reference
+
−
Controller
Stimulator
Nerve
Electrodes
Amplified nerve activity
Amplifier

3

A discussion on arbitrary waveform electrical neurostimulators

Objective: To review the application of arbitrary waveform to biological tissue.
Approach: An *electrical neurostimulator* (ENS) implements voltage-controlled, current-controlled, or charge-controlled stimulation pulses. These pulses are often biphasic to prevent electrolysis with electrode dissolution and tissue destruction. The pulse width, the amplitude, and the frequency can be adapted. However, most stimulators cannot implement arbitrary waves at the tissue level. We use the dielectric properties of gray matter of the brain using the Cole-Cole equation and discuss stimulator extensions that utilize the tissue's characteristics to implement arbitrary waveforms. We assume that the stimulator implements *pulse-width modulation* (PWM) signals.
Main results: The Cole-Cole equation of gray matter shows that it has a *low-pass filter* (LPF) behavior. Our simulation results suggest that arbitrary waves (using a PWM signal) can be implemented at the gray matter in two ways: with increased PWM frequency, or with LPF added to the stimulator's output.
Significance: Our results (using the dielectric properties of gray matter) provide a basis for further research on ENS designs for arbitrary waveform implementation.

3.1 Introduction

In this thesis, we neutralized SO and ED at single axon level in Chapter 1: we were able to meet our objective *in-silico*. One of the following steps is to validate these findings *in-vivo*. Therefore, an *electrical neurostimulator* (ENS) is required that is capable of implementing specific calculated and variating stimulation patterns.

The results from the *in-silico* experiment, using the extended HH model (Figure 1.7), suggest that electrical current pulses of 30 µs with varying amplitude are required to neutralize SO and ED. In this chapter, we elaborate on stimulator extensions to implement pulses of this magnitude.

Several methods can be used to activate neural tissue. A well-established method to stimulate a nerve is through direct application of electrical stimulation. Nevertheless, there are also other appropriate methods, e.g., magnetic, optogenetic, thermal, acoustic/mechanical, and chemical stimulation [29]. In this chapter, we focus on electrical stimulation.

3.1.1 Direct electrical stimulation

The application of an extracellular potential gradient across a neuron results in closely related intracellular potentials [29]. The change of intracellular voltages induce ionic current flows inside the cell, resulting in local hyperpolarizations and depolarizations [29]. The latter could influence the AP generation process related to pain (Section 1.2.1 and Section 2.1.1).

3.1.2 Stimulus mode

Three different stimulator modes are often used to generate the extracellular potential gradient: *voltage-controlled*, *current-controlled*, and *charge-controlled*. During voltage-controlled stimulation, the output of the stimulator is a voltage. The applied current depends on the inter-electrode impedance and follows Ohm's law [81]. The total amount of charge applied during a stimulus pulse is difficult to monitor due to the variations of the inter-electrode impedance [81]. During current-controlled stimulation, the stimulator applies a constant current to the tissue. The total applied charge to the tissue can more easily be determined than voltage-controlled stimulation; the applied current is constant. However, additional hardware is required to translate the voltage from a voltage source (e.g., a battery) to a constant current, which requires energy to operate [81]. Finally, during charge-controlled stimulation, internal capacitors in the stimulator are sequentially charged up to a particular value. While stimulating, the capacitors are discharged into the tissue. This circuit requires switches in the stimulator to be able to charge and discharge the capacitors sequentially [82].

3.1.3 Stimulus shape

Usually, the stimulation is applied as a pulse. A *monophasic pulse* consists of a cathodic or anodic phase. During a *biphasic pulse*, two monophasic pulses are applied subsequently; however, the polarity of the second pulse is reversed. This means that a cathodic phase is followed by an anodic phase, and an anodic phase is followed by a cathodic phase. The second pulse of a biphasic pulse is used to cancel the accumulated charge of the first pulse. After the first pulse, the accumulated charge can also be canceled by shortening the electrodes. In this situation, the discharge of the tissue is known as passive discharge [81]. The discharge phase is crucial for *long-term* implantable stimulators, as charge accumulation over time could result in electrolysis with electrode dissolution and tissue destruction [44].

3.1.4 Ultra-high frequency stimulation

The conventional stimulus modes apply pulses to the tissue at relatively low frequencies, up to 1200 Hz [83]. A different method to drive the right amount of charge to an electrode is by *ultra-high frequency* (UHF) stimulation [18]. During UHF stimulation, the cathodic and anodic phases are created using a sequence of current pulses at a high rate ($\approx$ 1 MHz) [84]. Figure 3.1 illustrates this stimulation pattern in comparison to the conventional constant-current stimulation biphasic pulse. UHF has great potential for reducing the power loss in the current driver during conventional current-controlled stimulations [84]. See Appendix A.12 for further details.

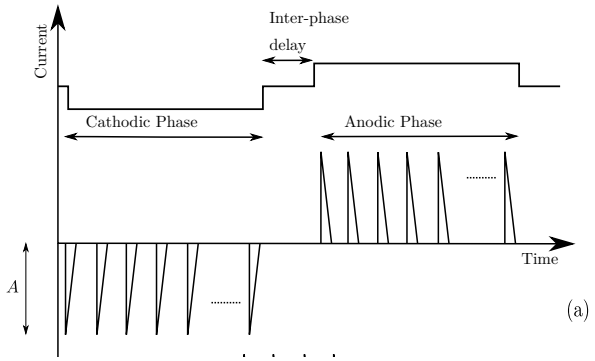

Figure 3.1: The top graph shows a conventional constant-current biphasic pulse, the bottom graph an UHF biphasic pulse. The cathodic and anodic phase are build up using a sequence of pulses. Figure from [84].

3.1.5 Chapter structure

In this chapter, we discuss a basic voltage-controlled and current-controlled ENS, and elaborate on future extensions to the system that are required to implement the stimulation patterns found in Chapter 1.

3.2 Basic stimulator

To better understand the basics of ENS systems, we designed a *voltage-controlled* and *current-controlled* ENS, based on the design of the open-source stimulator *Stimjim* [85]. We defined the design requirements for our stimulator as follows:

- *Voltage-controlled*: output between −15 V and 15 V;
- *Current-controlled*: output between −1 mA and 1 mA;
- High-impedance and low-impedance outputs.

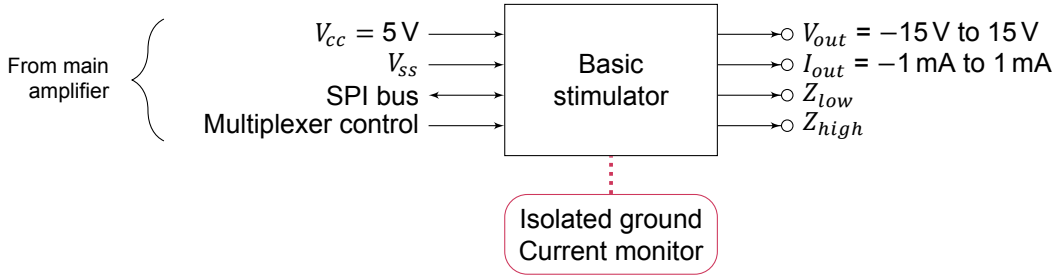

Figure 3.2: Inputs and outputs of the stimulator.

3.2.1 Circuit design

In the following sections, we discuss the critical points of the stimulator. Since the design is adapted from *Stimjim* [85], we will not focus on the the circuit design. We refer to Appendix A.13 for the stimulator's schematic.

3.2.1.1 Power supply

The power supply is based on an isolated DC-DC converter. Isolation is required to ensure that the stimulus return path is through the stimulation electrode and not through any grounding electrodes. The latter will result in a different electric field, and unintentional tissues may thereby be activated. We used the *IA0515S* from *XP Power* to transform a 5 V input to a positive output voltage up to 15 V and a negative output voltage down to −15 V.

3.2.1.2 Digital to voltage- and current-output

An 16-bit *digital-to-analog converter* (DAC) IC from *Texas Instruments* (TI) was selected to create a voltage between 0 V and 2.5 V. Next, an opamp shifts the *analog-to-digital converter* (ADC) output voltage towards voltages between 15 V and −15 V. These voltages are used to create voltage-controlled stimulation pulses. If the current-controlled mode was selected, the voltages between −15 V and 15 V were converted to currents between −1 mA and 1 mA, using a differential amplifier. To monitor the applied current, we added a shunt resistor of 100 Ω and amplified the voltage drop using an IA. A 12-bit ADC was applied to obtain a digital value of the applied current.

3.2.1.3 Digital communication

The DAC and ADC are controlled through an SPI bus. Since the ground of the stimulator is separated from the main amplifier's ground (due to the isolated DC-DC converter), digital isolators are required to transmit digital communication over the isolated barrier. Besides the SPI communication bus, several logic signals pass the isolation barrier. These signals include the output multiplexer's control signals and were used to connect the stimulation electrodes to the voltage-output driver, current-output driver, high-impedance, and low-impedance output.

3.2.1.4 Stimulator patterns

Monophasic and biphasic stimulation pulses were generated by controlling the DAC on the stimulator. The main amplifier used the SPI communication bus to control the stimulator. In addition, the stimulation patterns were be programmed with the help of the GUI (Section 2.2.7.2).

3.2.2 Board design

The board design is shown in Figure 3.3 and 3.4. The first thing that stands out is the separated ground plane; these planes divide the stimulator's ground from the main amplifier's ground. The DC-DC converter and the digital isolators were placed above this split. The large connector on the left side (Figure 3.4) was connected to the main amplifier by a cable. The stimulation probes can be connected on the right at the green terminal block or at the *Bayonet-Neill-Concelman* (BNC) connector (not visible in the 3D render). We showed the assembling process of the stimulator in Appendix A.11.

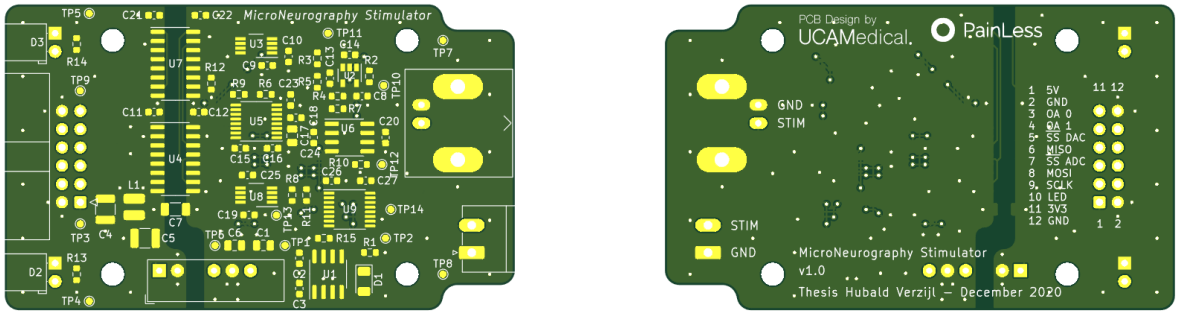

(a) Stimulator front.

(b) Stimulator back.

Figure 3.3: Stimulator board design.

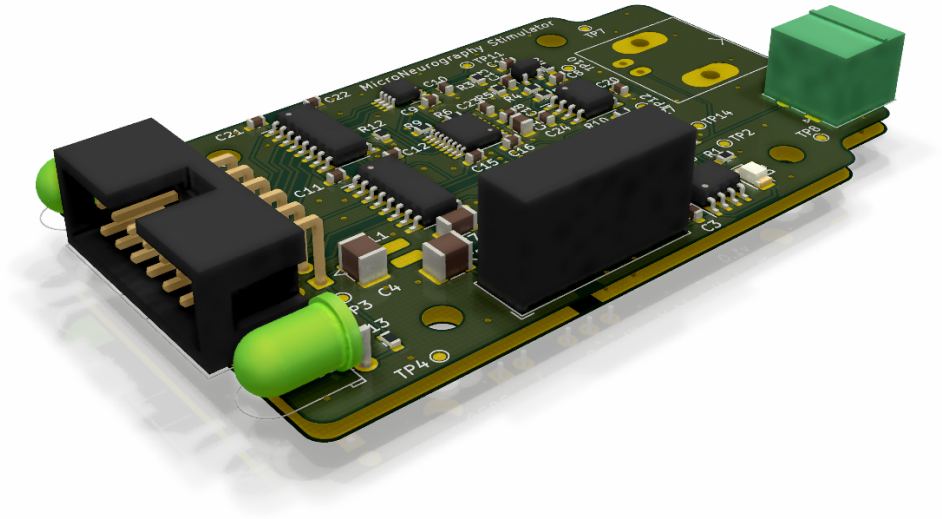

Figure 3.4: 3D render of stimulator board design including components, without the *Bayonet-Neill-Concelman* (BNC) connector.

3.2.3 Validation

We validated the stimulator *in-vitro* and *in-vivo*. For the *in-vitro* validation, the stimulator probes were shorted with a 10 kΩ resistor. An oscilloscope was used to verify the performance of the stimulator, monophasic and biphasic (current or voltage) pulses could be implemented successfully. We noticed that the stimulator had difficulties creating stimulation pulses that were shorter than 10 µs.

We validated the probe *in-vivo* on rats during the same experiments as discussed in Section 2.4. Figure 3.5 shows the applied stimulator electrodes. A stimulation pulse activated (visually) the muscles of the rat's leg. We also placed a microneurography electrode in the sciatic nerve. However, the stimulating and recording sites were too close to record any AP: the stimulation artifact dominated the recording.

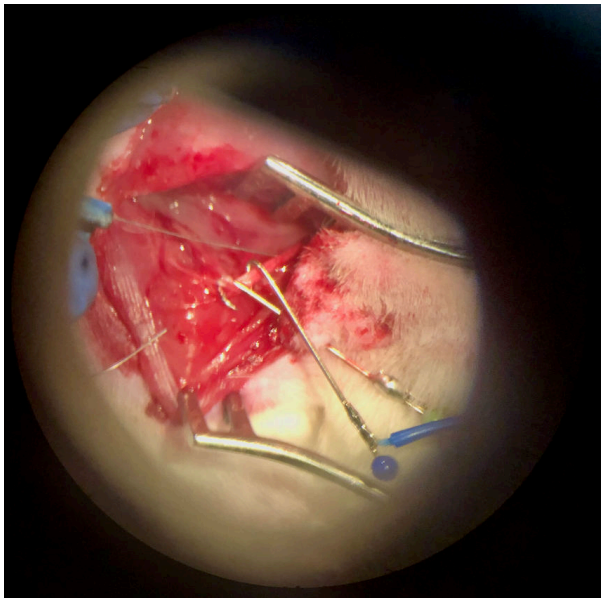

Figure 3.5: View through an operating microscope. Curved needles were used as stimulator electrodes and were placed around the sciatic nerve of the rat (Section 2.4.2.1).

3.3 Up-grade stimulator

With the presented standard stimulator is was not possible to implement arbitrary waves. In the following, we discuss methods to extend this design such that the stimulation pattern can be applied to the nerve.

3.3.1 Modeling biological tissue

The application of UHF current stimulation to the tissue results in an extracellular potential gradient across the neuron. However, this potential does not follow the applied stimulation curve [86]. In particular, the tissue's dynamics influence the stimulation-current-to-extracellular-potential behavior. Mathematical models are used to that describe the dynamics of biological tissue.

3.3.1.1 Dielectric properties

A well-known model is based on the dielectric properties of biological tissue [87], and uses the *Cole-Cole equation* to describe the dielectric behavior over the desired frequency range [88]. This model is given by

$$\hat{\epsilon}(\omega) = \epsilon_\infty + \sum_n \frac{\Delta\epsilon_n}{1 + (j\omega\tau_n)^{(1-\alpha_n)}} + \frac{\sigma_i}{j\omega\epsilon_0}, \tag{3.1}$$

where $\hat{\epsilon}$ represents the complex relative permittivity (relative to vacuum), also known as the 'dielectric constant'. ω represents the angular frequency, ϵ_∞ the dielectric constant at infinite frequency, σ_i the static ionic conductivity, and ϵ_0 the vacuum dielectric constant. To capture the dielectric behavior between 10 Hz and 100 GHz, this interval was divided in four ($n = 4$) dispersion regions [87]. For each region n, the parameters $\Delta\epsilon_n$, τ_n, and α_n describe the dynamics of that specific region. Following [86], the relative permittivity ϵ_r and the relative conductivity σ are specified as

$$\epsilon_r(\omega) = \Re\left[\hat{\epsilon}_r(j\omega)\right], \tag{3.2}$$

$$\sigma(\omega) = \Im\left[\hat{\epsilon}_r(j\omega)\right] \cdot -\epsilon_0\omega. \tag{3.3}$$

Given the dielectric constant $\hat{\epsilon}_r$, the impedance Z is given by

$$Z(\omega) = \frac{1}{\hat{\epsilon}_r j\omega C_0}, \tag{3.4}$$

where C_0 sets the absolute value of impedance and is dependent on, e.g., the electrode [86].

3.3.1.2 Frequency response of gray matter of the brain

The model that captures the dielectric properties is a fraction-order model, and should be implementable in `Matlab` using the `FOMCON` toolbox [89]. Unfortunately, we did not obtain good results with this toolbox due to rounding issues. Given that the fraction-order coefficients α_n of gray matter are between 0 and 0.22 [90], we set α_n equal to 0 for all n. This lead to obtaining a non-fraction-order model that can be implemented using the basic functionalities of `Matlab`. Figure 3.6a shows the relative permittivity ϵ_r and relative conductivity σ, and Figure 3.6b the resulting normalized impedance plot of Equation (3.4), using the parameters from [90]. Although we simplified the model by setting α_n to 0 for all n, the obtained frequency response looked similar to frequency response of gray matter obtained in prior research [86].

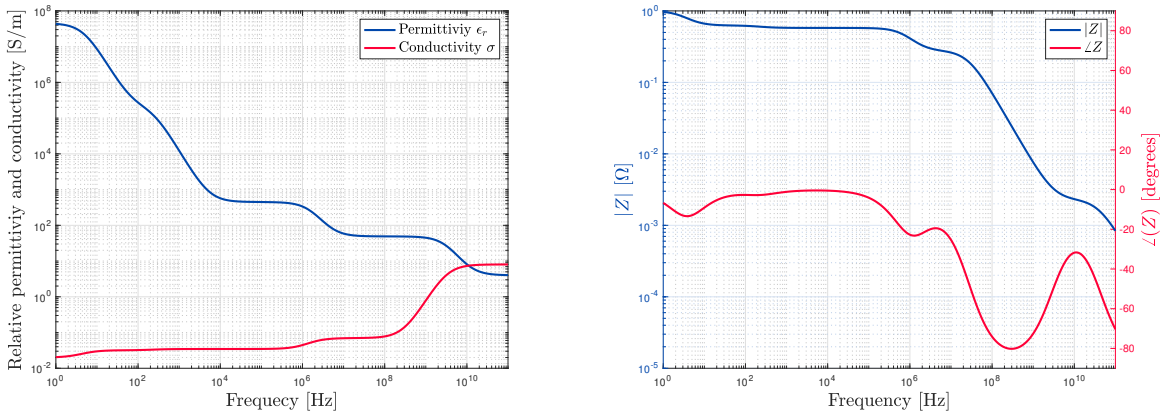

(a) Relative permittivity ϵ_r and relative conductivity σ.

(b) Normalized impedance Bode plot of Equation (3.4).

Figure 3.6: Frequency responses of gray matter, based on the parameters from [90]. These responses look similar to the responses obtained in [86].

3.3.2 Tissue potential following current stimulation

We used the frequency response of gray matter to determine the tissue's potential for constant current stimulation. For this purpose, we assumed an electrode impedance of $|Z| = 10\,\text{k}\Omega$ at 1 kHz. Next, we applied a constant current *pulse-width modulated* (PWM) signal at 200 kHz. Furthermore, we set the amplitude of this PWM signal at 200 µA (signal varies between 0 µA and 200 µA), and the duty cycle at 40%. These parameters were similar to parameters used in [86]. Figure 3.7 shows the tissue's potential for the applied PWM signal. These simulation results suggest that gray matter tissue acts as an *resistor-capacitor* (RC) *low-pass filter* (LPF). This property could be used to implement arbitrary waves.

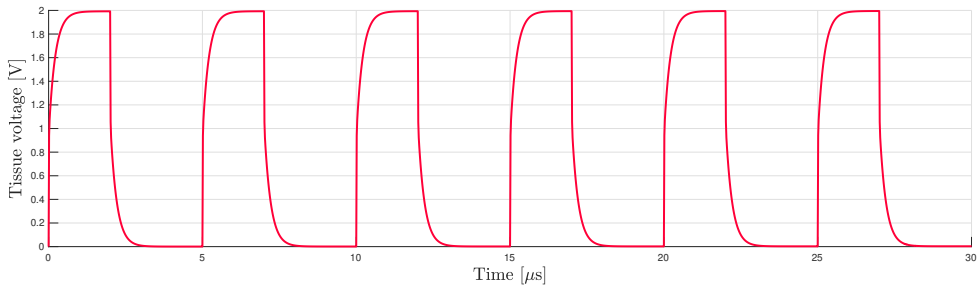

Figure 3.7: Voltage output of the gray matter model, when a PWM signal (amplitude 200 µA and duty cycle 40%) is applied.

3.3.3 Implementation of an arbitrary tissue voltage shape

UHF pulses may be used as the main building blocks to implement arbitrary waves. The LPF property of biological tissue can be used to steer the tissue's voltage towards a certain level. However, according to Figure 3.7, the time constant of the LPF is too small. In other words, the LPF has a high cutoff frequency, and its final (asymptotic) value is reached relatively fast. To benefit from this effect, the setup should be adapted in two ways: *(i)* by increasing the PWM frequency, *(ii)* by adding an LPF.

Therefore, we created an arbitrary wave in the form of a Gaussian curve. The wave starts at 0 µs and finishes at 30 µs. This waveform was based on the results of the *in-silico* experiments (Figure 1.7). The amplitude of this arbitrary wave was defined at 2 V. We will further refer to this curve as the reference. In addition, here we assume that PWM's duty cycle can be varied, while the amplitude is fixed at 200 µA. A 100% duty cycle results in a tissue voltage of 2 V.

3.3.3.1 Increasing the PWM frequency

In order to create a tissue voltage that is similar to the reference, the duty cycle of the PWM signal has to be varied. For each single PWM period, we determined the corresponding averaged reference. This averaged reference was used to vary the duty cycle of the PWM signal. E.g., an averaged reference of 0.5 V resulted in a duty cycle of 25%.

For this stimulation, we increased the PWM frequency to 50 MHz. In this way, we benefitted from the low-pass filtering effect of the tissue. Figure 3.8a shows the reference (Gaussian) curve and the obtained tissue's voltage, Figure 3.8b shows the PWM signal for the time interval around 10 s. These figures illustrate that by varying the duty cycle, arbitrary waves can be designed.

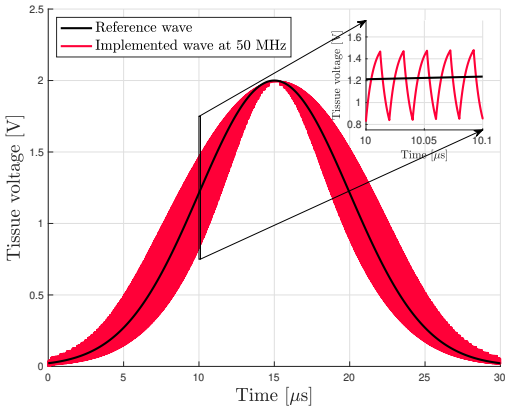

(a) Reference Gaussian curve and the obtained tissue's voltage.

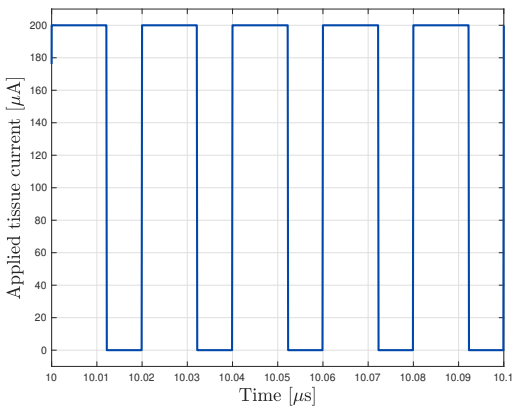

(b) Detailed view of the implemented (current) PWM signal (in Figure 3.8a) around 10 s.

Figure 3.8: The low-pass filtering behavior of the tissue is used to implement an arbitrary wave. To make use of this behavior, the PWM frequency is increased to 50 MHz.

3.3.3.2 Additional low-pass filter

In the following, we simulated an additional LPF at the stimulator's output. We created a first-order LPF and set the cutoff frequency f_c at 100 kHz. We lowered the PWM frequency to 0.5 MHz and used the same methodology as applied in Section 3.3.3.1 to find the 'optimal' duty cycles. Figure 3.9a shows the tissue's potential for this simulation, the corresponding implemented current PWM signal is shown in Figure 3.9b.

The results suggest that by using an additional LPF, an arbitrary wave can be generated. However, some time delay (equal to the time constant $\tau = 1/(2\pi f_c)$) was observed.

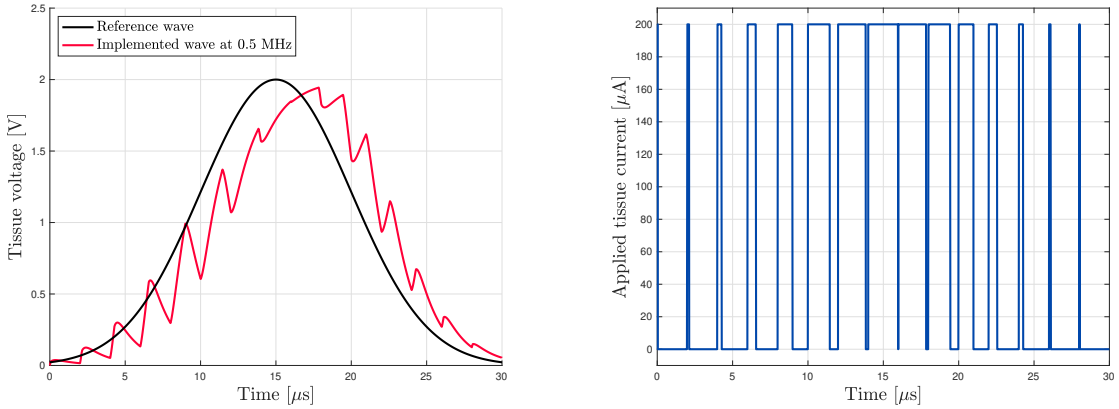

(a) Reference Gaussian curve and the obtained tissue's voltage.

(b) The implemented (current) PWM signal.

Figure 3.9: The low-pass filtering behavior of the tissue in combination with an additional LPF is used to implement an arbitrary wave. The PWM frequency is set at 0.5 MHz.

3.4 Discussion

3.4.1 Basic stimulator design limitations

We build a basic stimulator to explore the properties of *voltage-controlled* and *current-controlled* ENS circuits. The design of an ENS based on separate commercially available ICs requires many components to be implemented in order to be able to produce a stimulator that satisfies the design requirements. Biphasic pulses can be employed by controlling the stimulator's DAC. However, the DAC is controlled through an SPI bus, which has (in our case) a limited clock speed of 20 MHz. Setting a new value to the DAC's output requires 24 bits of data and takes at least 1.2 µs of communication time. This value can only be reached in an optimal hardware setting. Therefore, updating the DAC's output multiple times, during a stimulation pulse of 30 µs, is restricted and sensitive to errors due to the high communication speed.

Updating the duty cycle of the PWM signal and utilizing the gray matter's dielectric properties may be a solution to reduce the dependency on the digital communication bus. High-frequency (e.g., 5 MHz) PWM signals can easily be generated by a DMA steam in an MCU.

3.4.2 Stimulator extensions

In Section 3.3.1, we showed that gray matter tissue acts like an LPF for stimulation pulses. However, the results from Section 3.3.3 suggest that before we can benefit from this characteristic, the PWM frequency has to be increased significantly (from 200 kHz to 50 MHz), or an additional LPF should be added to the stimulator's output.

3.4.2.1 Increasing the PWM frequency

Increasing the PWM frequency demands strict requirements to the stimulation hardware; these high PWM frequencies can hardly be generated by basic hardware. Too much capacitance on the line will reduce the slew rate of the signal, and for 50 MHz PWM signals, the maximum and minimum voltages may not even be reached. Therefore, while implementing this extension, particular attention should be paid to this issue.

3.4.2.2 Additional low-pass filter

An additional LPF avoids the problem of generating high-frequency PWM signals. This filter may be added as passive RC LPF (Section 2.2.2) in the ENS itself or at the tip of the electrode. In addition to RC filters, the tip of the electrode may contain materials that act like an LPF with a similar cutoff frequency. Such an investigation fell out of the scope of this thesis.

Due to the averaging algorithm (as discussed in Section 3.3.3.1), the implemented tissue's voltages lag $\approx$1 µs behind the reference wave. This lag can be reduced by using the known time constant of the filter or advanced optimization algorithms that take the tissue dynamics and filter dynamics into account.

3.4.2.3 Computational requirements

Real-time calculations to determine the desired duty cycle values for a particular stimulus waveform can be computationally intensive. The *in-silico* results of Chapter 1 showed, however, that the shape of the stimulus is similar and only the amplitude varies. Therefore, predetermined duty cycle values which can be scaled may be sufficient to implement the required waveforms.

3.4.3 Arbitrary current waveforms

The dielectric properties of gray matter of the brain were used to determine the impedance Z relating the applied current to a tissue voltage. However, the results of Chapter 1 suggest stimulus patterns to neutralize SO and ED in µV. We consider this further in the general discussion.

3.4.4 Charge balancing

Charge balancing is required to prevent electrolysis with electrode dissolution and tissue destruction [44]. In our proposed up-grade ENS, we did not include hardware to monitor the applied charge. The applied charge can be estimated in software, based on the stimulus shape, and a neutralizing stimulus can be implemented subsequently. We refer to the general discussion for an elaboration on this topic.

3.5 Conclusion

Most electrical neurostimulators cannot implement arbitrary waves at the tissue level. We explored pros and cons of different methods to apply arbitrary waveforms using pulse-width modulated signals in relation to specifici tissue characteristics. We employed the Cole-Cole equation, which describes the tissue's dielectric properties. Our results suggest that arbitrary waves can be implemented by increasing the frequency of the pulse-width modulated signal or by adding a low-pass filter to the stimulator's output. Our results provide a basis for further research on electrical neurostimulator designs for arbitrary waveform implementation.

General discussion

Mitigating neuropathic pain

Neuropathic pain (NP) due to neuroma formation following a nerve lesion is regarded as being caused by the firing of neurons, which in turn lead to *subthreshold oscillations* (SO) and *ectopic discharges* (ED). Open-loop stimulation is currently used to treat patients, thereby applying a predefined *electrical neurostimulation* (ENS) pattern to the affected nerves. The downside of the technique is that during open-loop ENS, the ENS patterns are predefined and independent of the pain-provoking signals. Therefore, open-loop ENS is not effective at all moments of the pain experience caused by fluctuations in signal intensity. In addition, the side effect of open-loop ENS is the generation of a constant cumbersome sensation in an area that is larger than the original pain area. As the clinical results are disappointing, and in view of the high costs, the popularity of this technology is currently waning. Optimization of this potentially powerful technique is needed to improve the outcome and make this technology useful to implement in the treatment strategy of patients with intractable, otherwise difficult to treat pain syndromes. Theoretically, optimization of stimulation technology is possible by actually neutralizing SO and ED, which should lead to mitigating the generation of NP. We proposed a closed-loop strategy (Figure 3.10), where the ENS pattern is real-time adjusted to neutralize SO and ED. Our strategy consists of several steps. First, the activity in a peripheral nerve is measured. Next, these measurements are used by a controller to determine an electrical stimulus pattern. Subsequently, the generated stimulus pattern is applied to the nerve using an electrical neurostimulator. Therefore, our closed-loop ENS strategy stands out from the currently applied open-loop ENS strategies, by detecting and using the pain-provoking signals at the peripheral nerve level to adapt the applied ENS pattern.

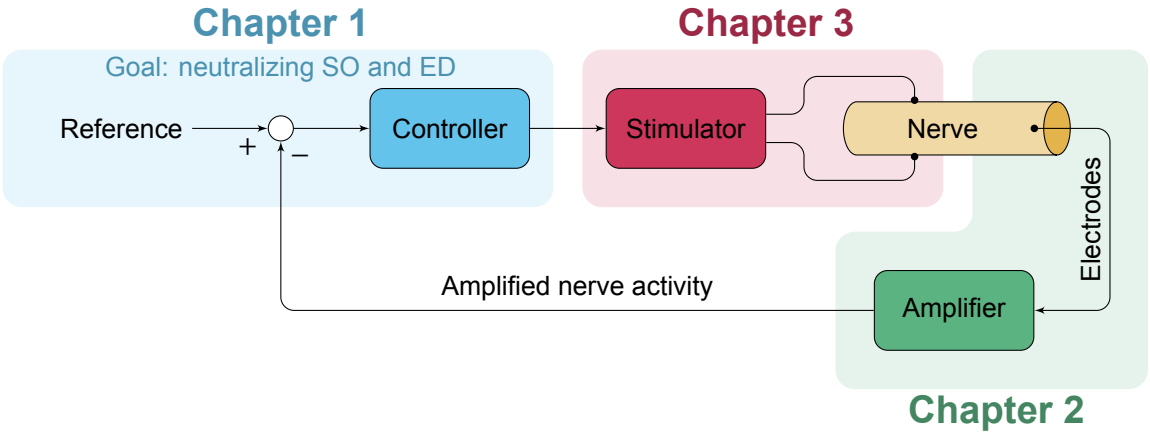

Figure 3.10: Proposed closed-loop methodology to neutralize SO and ED, and thereby mitigate the generation of NP.

In Chapter 1, we focused on the design of the controller. We set up a *model predictive controller* (MPC) that uses mathematical models to find an appropriate stimulus to neutralize SO and ED at the single axon level. In order to avoid the usage of a model of great complexities within the MPC framework, we captured the model's statistical properties in a *fractional-order system* (FOS), which was subsequently used within the MPC framework. Using our controller design, we showed *in-silico* that SO and ED were be neutralized in three well-known neuroma models by only using the statistical properties of these models. In all simulations, the obtained input to suppress SO and ED resembled (arbitrary) pulse-shaped patterns, which were as short as 30 µs.

Real-time neural activity measurements are required for the controller. In Chapter 2, we designed a dedicated setup, capable of measuring this nerve activity using microneurography, while embedding processing power and extensions for simultaneous stimulation. Adequate handling of interference was crucial. If not handled adequately, the neural activity could not be measured appropriately. We rejected

the interferences using several methods and made valuable recordings *in-vivo*, which showed APs in the lugworms' ventral nerve cord and the rat's sciatic nerve.

The final step of our proposed strategy was to implement the found generated stimulus pattern at the peripheral nerve. In Chapter 3, the implementation of (arbitrary) pulse-shaped patterns (as suggested in Chapter 1) to neutralize SO and ED is discussed. Currently, available stimulation techniques are not sufficient, and stimulator extensions are required. The results of this chapter suggest that the dielectric properties of biological tissue can be used (in combination with an additional low-pass filter) to apply arbitrary stimulus waveforms.

Chapter 1, Chapter 2, and Chapter 3 provide the essential information to eventually apply our theoretical proposed strategy *in-vivo*. However, before we arrive at that stage, additional research is required.

From theory to practice

The following sections discuss the next steps and the barriers and difficulties concerning the implementation of our proposed strategy in practice.

Modeling SO and ED

For the *in-silico* experiments, we implemented three well-known neuroma models which capture SO and ED. The extended *Hodgkin-Huxley* (HH) model and the *Morris-Lecar* (ML) model were based on the cell membrane modifications, as observed in neuromas. The *map-based* (MB) model was based on phenomenological characteristics. A pattern could be found that neutralizes SO and ED *in-silico*. However, these models do not exactly represent the real neuroma behavior and they all behave somewhat differently. To show that our strategy has the potential to reach promising results, these models are sufficient. An intrinsic long-term memory is a key feature for our strategy; the applied models and also the *in-vivo* neuroma behavior show this property. However, to simulate more complex cases, these models may result in unexpected behavior.

For example, charge balancing is essential during electrical neurostimulation to prevent electrolysis with electrode dissolution and tissue destruction [44]. We added charge balancing as a constraint to our MPC framework, but it did not result in neutralizing SO and ED. However, this does not necessarily imply that it does not work in a true neuroma. Injecting and removing the same amount of current in theoretical models does not lead to an altered response, while *in-vivo* this may be the case.

Our proposed strategy is successful in all three neuroma models. Therefore, the prospect of future *in-vivo* experiments is optimistic. Any mismatch between the model and the actual neuroma behavior may still lead to SO and ED neutralization *in-vivo*, as the statistical properties are similar. Our strategy of implementing a FOS could still be used.

Single-unit versus multi-unit activity

The *in-silico* results (Chapter 1) suggest that stimulus patterns can be derived such that they neutralize SO and ED. However, our controller design is based on neural activity measurements at the single axon level (or single-unit). *In-vivo* experiments to validate the neural amplifier on lugworms and rats (Chapter 2), showed that single-unit activity can be obtained if giant axons are present. If these axons are not present, multi-unit activity from many small axons will be recorded simultaneously. Relating this to *in-vivo* SO and ED neutralization, crucial information that is required by the controller (Chapter 1) must then be extracted from these multi-unit recordings. Certain frequency parameters, such as an increased magnitude of a certain frequency, may show to be sufficient to serve as an input to the controller in order to find appropriate stimulus patterns.

Success rate of recording neural activity

Adequate handling of interference was crucial to record neural activity using microneurography (Chapter 2). After microneurography electrode positioning, a Faraday cage showed indispensable to reject any interference. Future applications have to embed the electronics within a shielded enclosure while implanted into the body, close to the nerve. The level of interference may thereby be reduced, however, it will remain a fundamental point of attention in the design. Further improvement seems possible by embedding the preamplifier electronics in the electrode itself, close to the tip of the electrode.

Next to the issues related to the interference, the correct positioning of the electrode is crucial. Our

applied microneurography electrodes had a (single) non-isolated tip. Electrodes that contain multiple recording sites potentially increase the chance of effective positioning, which is close to individual axons. Furthermore, for optimal fixation of the electrodes, they should be placed longitudinally into the nerve instead of transversally.

Electric field distribution

In Chapter 1, electrical stimulation patterns were developed which neutralize SO and ED *in-silico*. These patterns were defined as the required current through the membrane. The extended HH and extended ML model defined this current as 'microamp' and the extended MB model as 'arbitrary'. The extended electrical neurostimulator proposed in Chapter 3 applies a potential gradient across the nerve defined as 'voltage'. Additional modeling is required to relate the applied electric field to the resulting current through the membrane. These models have been described before [91].

The electric field depends on the distance between the electrode and the axon, which raises the question of whether the applied electric field will neutralize SO and ED in all axons. SO and ED are observed in patch-clamp experiments and are, therefore, measured at the single axon level [23]. It is unknown whether multiple axons oscillate simultaneously in the same way. If so, the applied electric field may neutralize the SO in multiple axons. However, if each axon shows different SO and ED patterns, the applied stimulation pattern may adversely evoke SO and ED in specific axons. Clearly, an appropriate stimulus which is able to neutralize the effect of SO and ED of all axons should be implemented.

Neutralizing SO and ED

Throughout this thesis, we assumed that it should be possible to mitigate the generation of NP by our strategy: neutralizing SO and ED. However, minimizing the rate of ED (without neutralizing SO) may mitigate the generation of NP as well. Alternatively, limiting the EDs to a maximum per time period, e.g., one hour, could be sufficient. Furthermore, alternating these approaches may resolve issues with, e.g., habituation.

Regardless of our results, it remains to be proven that our strategy will indeed eventually mitigate the generation of NP. The generation of data (that reveals information regarding SO and ED activity contributing to the generation of NP) is of great importance in the development of a strategy that should ultimately mitigate the generation of NP.

To summarize, the goal of this project was to suppress SO and ED neural activity. Thereby, engineers need to keep the patient's demands in mind: the relief of NP is the ultimate goal, and every step that brings us closer to that goal is worth exploring. Even the smallest relief may change someone's life for the better.

A

Appendixes

A.1 Modeling subthreshold oscillations and ectopic discharge

A.1.1 Extended Hodgkin-Huxley model

We discussed the modifications that others [24] applied to the *Hodgkin-Huxley* (HH) model, such that the model describes *subthreshold oscillations* (SO) and *ectopic discharge* (ED). The extended HH model is described by

$$I(t) = C_m \dot{v}_m(t) + I^F_{Na^+}(t) + I^M_{Na^+}(t) + I^S_{Na^+}(t) + I_l(t), \tag{A.1a}$$

$$I^F_{Na^+}(t) = \bar{g}^F_{Na^+} m_F(t)^3 h_F(t)(v_m(t) - E_{Na^+}), \tag{A.1b}$$

$$I^M_{Na^+}(t) = \bar{g}^M_{Na^+} m_M(t) h_M(t)(v_m(t) - E_{Na^+}), \tag{A.1c}$$

$$I^S_{Na^+}(t) = \bar{g}^S_{Na^+} m_S(t) h_S(t)(v_m(t) - E_{Na^+}). \tag{A.1d}$$

To better understand the influence of the different ion channels on the final membrane voltage, Figure A.1 shows the values of the activation (m) and inactivation (h) parameters of the *fast* (F), *medium* (M), and *slow* (S) sodium ion channels. The different time constants and steady-state values of the activation and inactivation parameters are used to model the different ion channels. Of note, the shape of the m and h parameter graphs is similar to the membrane voltage. A similar shape is expected since these parameters are the building blocks for every individual spike.

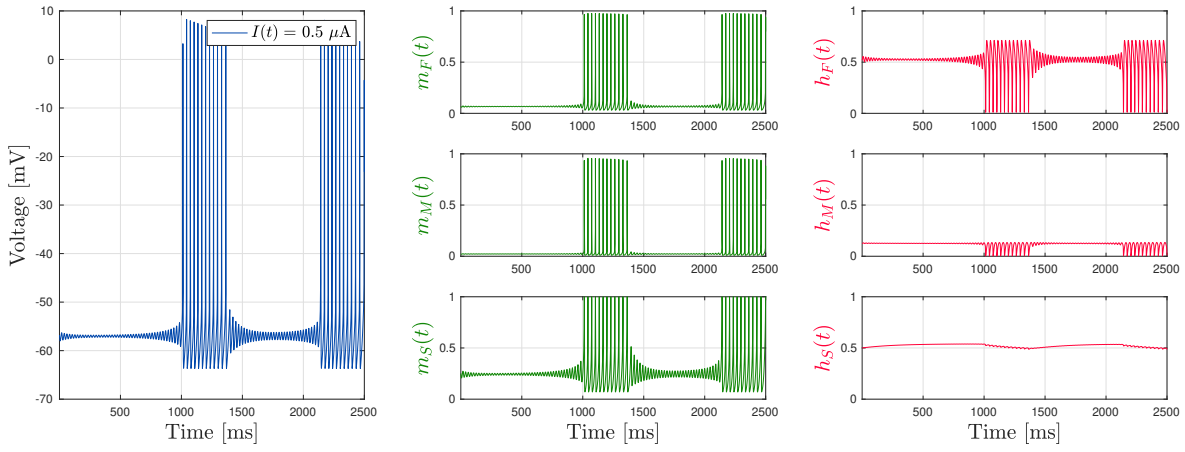

Figure A.1: Simulation of the extended HH model described by Equation (A.1a) - (A.1d). The figure on the left shows the membrane voltage, the smaller plots in the middle, and on the right, visualize the values of the activation m and inactivation h parameters.

The influence of conductance and time constant adjustments were studied before [24], but were repeated, especially because some parameters were not addressed in prior research. Gradually reducing

$\bar{g}^F_{Na^+}$ and $\bar{g}^M_{Na^+}$ removed the oscillations and ectopic activity. A reduction of $\bar{g}^S_{Na^+}$ resulted in a narrower window of stimulation currents that triggered oscillations and ectopic activity. Increasing $\tau_m(v_m(t))$ of the medium and slow sodium channel given by Equation (A.1c) and (A.1d), while $\tau_m(v_m(t))$ of the fast channel given by Equation (A.1b) was kept constant, resulted in a gradual decrease of the stimulation current window that triggered ectopic discharge. At time constants above 0.5 ms, the ectopic activity disappeared

Three crucial aspects were concluded [24]. First, $\overline{g}^F_{Na^+}$ is related to burst and sustained spike discharge. Second, the medium current ($\overline{g}^M_{Na^+}$) is essential for the oscillations, and thirdly, the slow current ($\overline{g}^S_{Na^+}$) is essential for the interrupt tonic firing and enabling bursting.

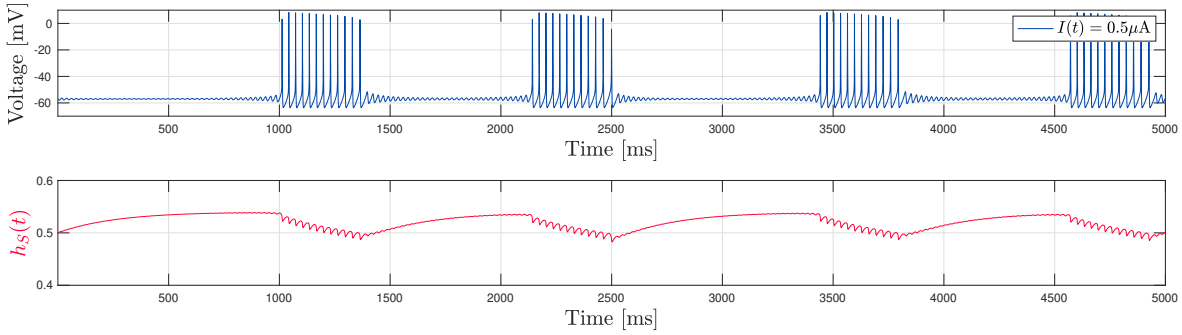

Figure A.2: Similar to Figure A.1 however, only the membrane voltage and the inactivation parameter h of the slow ion channel are shown.

Figure A.2 shows the same input-output response as in Figure A.1. Only the membrane voltage and the inactivation parameter h of the slow channel S are shown. The inactivation parameter h seems to influence the ectopic discharge behavior. During oscillatory periods, the parameter h increases until a threshold is reached, then the neuron starts firing. During this burst, the parameter h decreases until the firing stops. This figure shows that the parameter h is responsible for activating and deactivating the ED.

A.1.2 Extended Morris-Lecar model

The *Morris-Lecar* (ML) model was adapted by others, such that it was capable of capturing spiking activity and subthreshold behavior [25]. The complete extended ML model is given by

$$I(t) = C_m \dot{v}_m(t) + \overbrace{\bar{g}_{Ca^{2+}} M_\infty(v_m(t))(v_m(t) - E_{Ca^{2+}})}^{I_{Ca^{2+}}(t)} + \overbrace{\bar{g}_{K^+} N(t)(v_m(t) - E_{K^+})}^{I_{K^+}(t)} + \overbrace{\bar{g}_l(v_m(t) - E_l)}^{I_l(t)} + n(t), \tag{A.2a}$$

$$\dot{N}(t) = \frac{N_\infty(v_m(t)) - N(t)}{\tau_N(v_m(t))}, \tag{A.2b}$$

$$M_\infty(v_m(t)) = 0.5\left[1 + \tanh\left(\frac{v_m(t) - \beta_m}{\gamma_m}\right)\right], \tag{A.2c}$$

$$N_\infty(v_m(t)) = 0.5\left[1 + \tanh\left(\frac{v_m(t) - \beta_w}{\gamma_w}\right)\right], \tag{A.2d}$$

$$\tau_N(v_m(t)) = \frac{1}{\frac{\cosh(v_m(t) - \beta_w)}{2\gamma_w}}. \tag{A.2e}$$

In this adapted model, $v_m(t)$ represents the membrane voltage and $N(t)$ the recovery variable. $E_{Ca^{2+}} \in \mathbb{R}$, $E_{K^+} \in \mathbb{R}$ and $E_l \in \mathbb{R}$ are the equilibrium potentials of the calcium, potassium and leak ion channels, $\overline{g}_{Ca^{2+}} \in \mathbb{R}_+$, $\overline{g}_{K^+} \in \mathbb{R}_+$ and $\overline{g}_l \in \mathbb{R}_+$ the ion channel conductivities. The external stimulus current is expressed by the parameter $I(t) \in \mathbb{R}$. $\beta_m \in \mathbb{R}$, $\beta_w \in \mathbb{R}$ and $\gamma_w \in \mathbb{R}$ can be used to set

the steady state values of the $M_\infty(v_m)$, $N_\infty(v_m)$ and $\tau_N(v_m)$ parameters. An *additive white Gaussian noise* (AWGN) source $n(t) \sim \mathcal{N}(0, \sigma^2)$ with $\sigma = 20\,\text{mV}$ was added. This noise approximates the effect of stochastic channel opening [25].

This model is capable of generating spiking activity and SO. This (NP) behavior was only seen if β_w was increased from $-21\,\text{mV}$ to $-13\,\text{mV}$. By changing β_w, the voltage versus current relation of slower recovery variable $N(t)$ is adapted. A smaller current flow was noticed while lowering β_w [25]. This lowered flow resulted in a model that could become unstable faster than the original system, explaining the ectopic activity.

A.1.3 Extended map-based model

The standard *map-based* (MB) model appeared to be incapable of including SO and ED. In order to exhibit SO and ED, *Shilnikov and Rulkov* extended the MB model by introducing an additional state. By doing so the model became

$$x_{k+1} = f_\alpha(x_k, y_k + \beta) + \zeta_k, \tag{A.3a}$$
$$y_{k+1} = y_k - \mu(x_k + 1 - \sigma), \tag{A.3b}$$

where $x_k \in \mathbb{R}$ represents the membrane potential and $y_k \in \mathbb{R}$ an arbitrary state that can turn the spike generator on or off [26]. The (dimensionless) injected current is modeled by $\sigma \in \mathbb{R}$, $\alpha, \beta \in \mathbb{R}$ are arbitrary tuning parameters and $0 < \mu \ll 1$ is the coupling parameter of both states. They assumed that noise influences the spiking behavior of a neuron. This noise was modeled by an AWGN source, i.e., $\zeta_k \sim \mathcal{N}(0, s^2)$. The piecewise continuous function $f_\alpha(x_k, y_k + \beta) : \mathbb{R} \times \mathbb{R} \to \mathbb{R}$, was defined by [26] as

$$f_\alpha(x_k, y_k + \beta) = \begin{cases} -\alpha^2/4 - \alpha + y_k + \beta & \text{if } x_k < -1 - \alpha/2, \\ \alpha x_k + (x_k + 1)^2 + y_k + \beta & \text{if } -1 - \alpha/2 \leq x_k \leq 0, \\ y_k + 1 + \beta & \text{if } 0 < x_k < y_k + 1 + \beta, \\ -1 & \text{if } x_k \geq y_k + 1 + \beta. \end{cases} \tag{A.4}$$

The cobweb plot of parameter x_k of the system defined in Equation (A.3a) and (A.3b) is presented in Figure A.3 and A.4; these figures show two cobweb plots for two different parameters y_k in $f_\alpha(x_k, y_k + \beta)$. Figure A.3 shows the trajectory for $y = -0.2$: the trajectory converges to a stable point. Figure A.4 shows the trajectory for $y = 0.2$, in this situation the system did not reach a stable point. Varying the parameter y_k results in turning the ectopic discharge generation on or off.

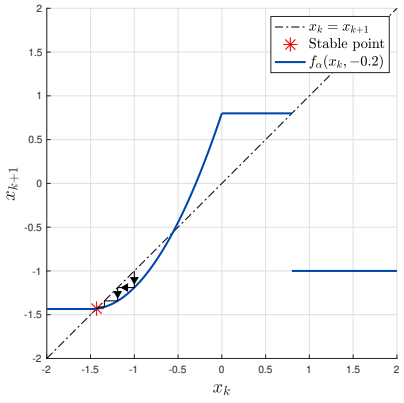

Figure A.3: The cobweb plot of parameter x_k of the system defined in Equation (A.3a) and (A.3b) for $y_k = -0.2$ and $\beta = 0$. A stable point is present that moves along the line $x_k = x_{k+1}$ which results in SO in the time domain. Due to the existence of a stable point, not a single spike (or ED) is generated.

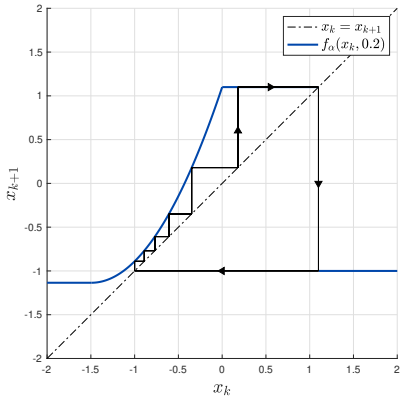

Figure A.4: The cobweb plot of parameter x_k of the system defined in Equation (A.3a) and (A.3b) for $y_k = 0.2$ and $\beta = 0$. The curve f_α from Figure A.3 has slightly moved up. The stable point has disappeared and ED will be generated. The trajectory of a single spike is shown.

It is assumed that an AWGN influences the spiking behavior in a neuron [26], as indicated by ζ_k in Equation (A.3b). This noise can be interpreted as a random vertical shift of the piecewise continuous function f_α as shown in Figures A.3 and A.4. Due to this shift, the stable point (if present) will constantly

move along the line $x_k = x_{k+1}$. In other words, the stable point is different for every time step. This behavior will result in SO in the time domain. If the shift is large enough, stable points are absent, appearing as ED in the time domain. By modifying the parameter σ (stimulation 'current'), the parameter y_k is moved slightly, which changes the probability that ζ_k will introduce ED.

A.2 An MPC with fractional-dynamics proxy approach using a linear control scheme

Figure A.5 shows the closed-loop simulation on the ML model using a $(p = 15)$-step approximation. Figure A.6 shows the closed-loop simulation on the ML model using a $(p = 1)$-step approximation, or simplified linear control scheme. Comparing Figure A.5 with Figure A.6 shows that both approximations are sufficient to suppress SO and ED, although in the $(p = 1)$-step approximation, a positive and a more aggressive stimulation current (in terms of the total applied energy and fluctuations of the actuation current) is required. Translated to the stimulation hardware, this could limit the lifetime of the battery. The different outcomes of both simulations indicate that a more stable membrane potential can be achieved using the $(p = 15)$-step approximation, while the applied charge was lower. Therefore, our proposed dynamical system-based feedback control scheme will resolve problems related to the use of complex well-established neuroma models and the use of a simplified linear control scheme.

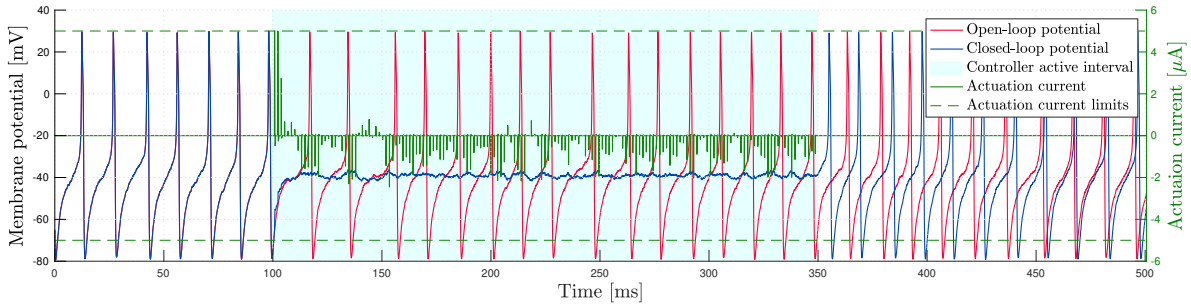

Figure A.5: An MPC with a fractional-dynamics proxy approach applied to the extended ML model. The open-loop response is given by the red curve. The predictive model was a $(p = 15)$-step (0.75 ms) approximation of the FOS plant, using a $(P = 20)$-step (1 ms) prediction horizon and a $(M = 10)$-step (0.5 ms) control horizon. The response is shown by the blue curve. The reference for the membrane potential was −40 mV. Suppression of SO and ED could be observed within the controller active interval (between 100 and 350 ms). The green curve indicates the applied stimulation current.

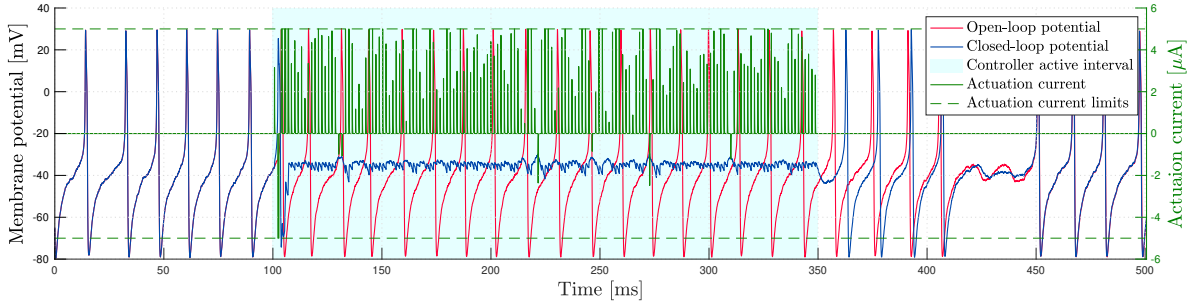

Figure A.6: An MPC with a fractional-dynamics proxy approach applied to the extended ML model. We adapted the predictive model used in Figure A.5 by only adjusting the $(p = 15)$-step (0.75 ms) approximation of the FOS to a $(p = 1)$-step (0.05 ms) approximation. Suppression of SO and ED could be observed within the controller active interval (between 100 and 350 ms). However, the stimulation current in this $(p = 1)$-step approximation is mainly positive, more aggressive, and has larger amplitudes compared to Figure A.5. Thus, the $(p = 1)$-step approximation can lead to significant battery performance decrease.

A.3 An open-loop strategy with predetermined stimulation patterns using the ML model

An open-loop strategy is applied with biphasic pulses (*pulse width* (PW) 250 µs and amplitude 2 µA) at 50 Hz as we show in Figure A.7. In this situation, no SO and ED suppression is achieved.

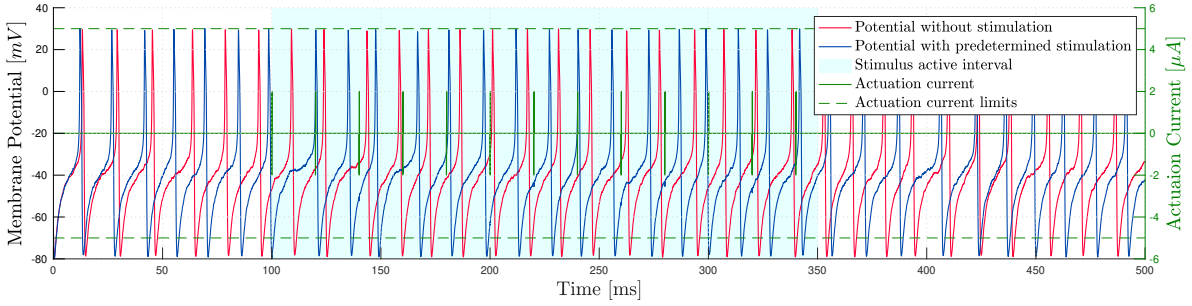

Figure A.7: Open-loop stimulation with biphasic pulses (PW 250 µs and amplitude 2 µA) at 50 Hz using the ML model. The SO and ED are not suppressed.

Updating the stimulation pattern to a non-biphasic anodic pulses (PW 250 µs and amplitude 2 µA) and increasing the stimulation frequency to 500 Hz does not lead to SO and ED suppression either, as we show in Figure A.8. However, application of a cathodic pulse (PW 250 µs and amplitude −2 µA) at a frequency of 500 Hz results in SO and ED suppression (Figure A.9). Open-loop stimulation may lead to SO and ED suppression, however, the required stimulation pattern was found by trial-and-error.

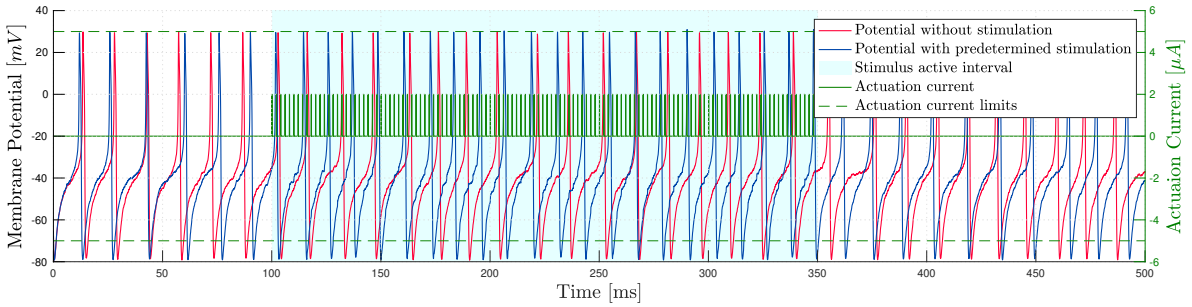

Figure A.8: Open-loop stimulation with anodic pulses (PW 250 µs and amplitude 2 µA) at 500 Hz using the ML model. The SO and ED are not suppressed.

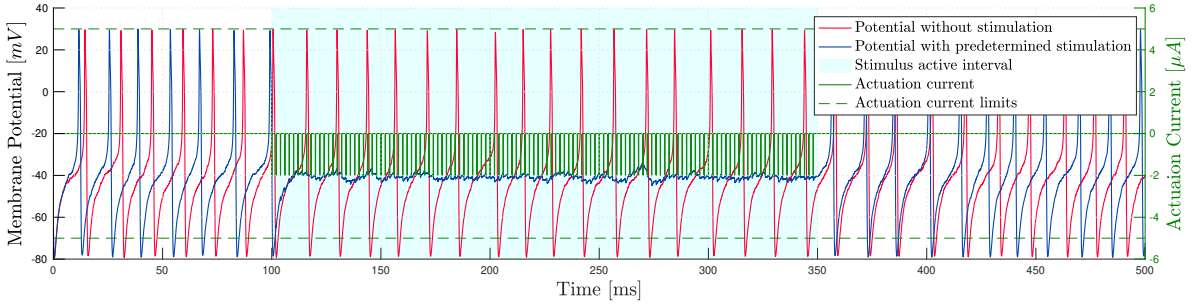

Figure A.9: Open-loop stimulation with cathodic pulses (PW 250 µs and amplitude −2 µA) at 500 Hz using the ML model. The SO and ED are suppressed. The required stimulation pattern was found by trial-and-error.

A.4 An MPC with fractional-dynamics proxy approach including additional constraints

Electrolysis with electrode dissolution and tissue destruction may occur if an imbalanced stimulation is applied to the tissue. To prevent electrolysis, the charge after a stimulation pulse should be equal to zero, $Q = 0$. We added this charge balancing constraint to our MPC strategy to simulate the prevention of electrolysis while SO and ED are suppressed.

A.4.1 Biphasic pulse constraint

Stimulators often apply biphasic pulses to overcome the problem of electrolysis. We defined a biphasic pulse constraint with several domains of freedom for the optimization algorithm: 1) Beginning of the pulse could be anodic or cathodic first, 2) the amplitude can be varied, and 3) the length of anodic and cathodic phase together can be varied. However, the duration of the anodic and cathodic phases should be identical, and the integral over the stimulation amplitude of a single pulse should be equal to zero.

Figure A.10 shows the result of an MPC with a fractional-dynamics proxy approach, including the biphasic pulse constraint. From this figure, it follows that the SO and ED can not be inhibited in this situation.

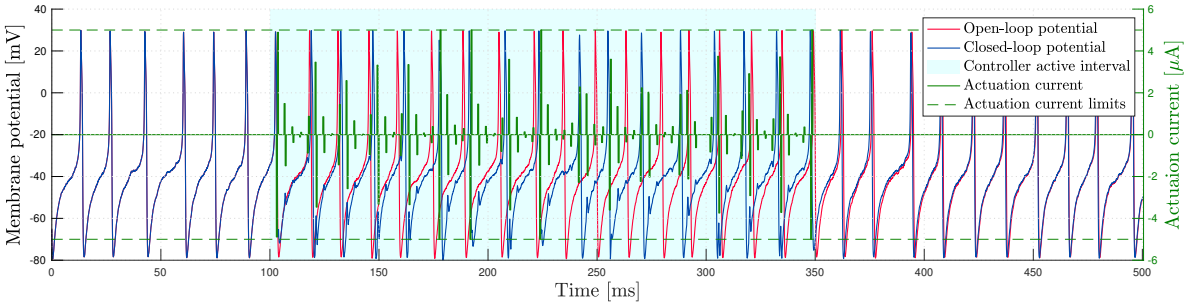

Figure A.10: An MPC with a fractional-dynamics proxy approach, applied to the extended ML model, including a biphasic pulse constraint. The open-loop response is given by the red curve. The predictive model is a ($p = 15$)-step (0.75 ms) approximation of the FOS plant, using a ($P = 20$)-step (1 ms) prediction horizon and a ($M = 10$)-step (0.5 ms) control horizon, this time response is shown by the blue curve. The reference for the membrane potential was −40 mV. Suppression of SO and ED could not be observed within the controller active interval (between 100 and 350 ms). The green curve indicates the applied (biphasic) stimulation current.

A.4.2 Charge balancing constraint

Besides the biphasic constraint, we were able to generate a less restricted stimulation pattern. In order to do so, we defined that the integral over the stimulation amplitude of a single pulse should be equal to zero. From the results in Figure A.11 it can be derived that our MPC strategy will compensate for the total applied current at the end of the pulse. This strategy still resulted in unsuccessful suppression of SO and ED. This does not imply that the charge balancing constraint will not result in unsuccessful SO and ED suppression *in-vivo*. However, we cannot show it using our mathematical models *in-silico*.

A.4.3 Complicated optimization problems

Adding constraints did not result in sufficient suppression of SO and ED. However, due to the simplicity of the applied models, it does not mean that suppression of SO and ED pulses in individual axons is impossible. These models may ignore specific characteristics, while they are essential for SO and ED suppression.

Additional charge constraints to our proposed dynamical system-based feedback control scheme complicated the optimization problem. Our proposed control scheme, including the FOS, resulted in a quadratic objective function with linear constraints, which could be solved easily by a quadratic programming solver. The optimization problem will transform into a constrained nonlinear multivariable function by introducing other nonlinear constraints to describe the biphasic pulse or charge balancing constraint. This problem is more difficult to solve and requires more advanced methods that solve the

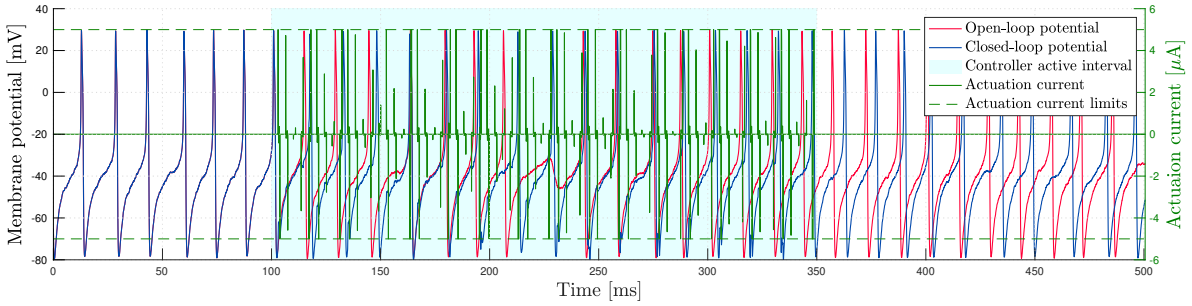

Figure A.11: An MPC with a fractional-dynamics proxy approach, applied to the extended ML model, including a charge balancing constraint. The open-loop response is given by the red curve. The predictive model is a $(p = 15)$-step (0.75 ms) approximation of the FOS plant, using a $(P = 20)$-step (1 ms) prediction horizon and $(M = 10)$-step (0.5 ms) control horizon, this time response is shown by the blue curve. The reference for the membrane potential was -40 mV. Suppression of SO and ED could not be observed within the controller active interval (between 100 and 350 ms). The green curve indicates the applied (balanced) stimulation current.

optimization problem, while including the (nonlinear) constraints.

A.5 Types of axons

Axon type	Subtype	Sheath	Functions	Radius (µm)	Conductance velocity (m/s)	Spike duration (ms)	Absolute refractory period (ms)
A	α	Myelinated	Proprioception somatomotor	12-20	70-120	0.4-0.5	0.4-1
	β		Touch, pressure	5-12	30-70		
	γ		Motor for muscle spindles	3-6	15-30		
	δ		Pain, cold, touch	2-5	12-30		
B		Myelinated	Preganglionic autonomic	<3	3-15	1.2	1.2
C	Dorsal horns	Unmyelinated	Pain, temperature, mechanoreception and reflex response	0.5-2	0.5-2	2	2
	Sympathetic	Unmyelinated	Pilomotor, sudomotor and vasomotor	0.7-2.3	0.7-2.3	2	2

Table A.1: Conductance velocity of different axon types [51].

A.6 Recording neuronal activity

A.6.1 Intracellular recording

During intracellular recordings, the investigator places an electrode in the neuron. A high *signal-to-noise ratio* (SNR) amplifier records the measured voltage in the neuron. Individual action potentials can be measured and analyzed. To study the influence of the different voltage-gated ion channels, researchers use *voltage-clamp techniques*. During these measurements, the potential in the neuron is kept constant by injecting a small current. The injected current will leave the neuron through the neuron's ion channels and, due to the voltage-gated ion channels, the flow depends on the applied potential. This setup is shown in Figure A.12. Individual ion channels could be studied in further detail by blocking specific ion channels using fluids. Researchers can examine the membrane potential vs. ion channel activation characteristic for individual ion channels or ion channel groups in detail.

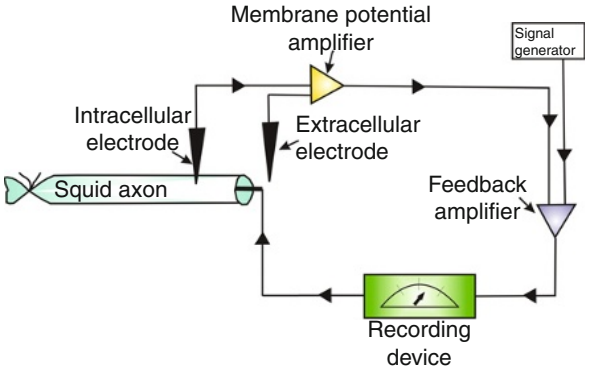

Figure A.12: Intracellular recording setup; the measured potential in the neuron membrane is amplified. During a voltage-clamp measurement, the feedback amplifier regulates the current such that the membrane potential is kept constant. During a current-clamp measurement, the current flow is kept constant and the membrane potential is measured [92].

Besides the *voltage-clamp methods*, also *current-clamp methods* are used to study the neuron behavior. During these experiments, a setup injects a constant current into the neuron. The constant current can also be seen as an external stimulus. If the injected current leads to an exceeding of the firing threshold, the neuron will generate an action potential. Researchers use these *current-clamp methods* to investigate the action potentials of individual neurons. By using specific ion channel blockers, the therapeutic effects of certain drugs can be investigated [93].

A.6.2 Extracellular recording

Instead of measuring inside the neuron, scientists can also place an electrode in the extracellular space (outside the neuron). Depending on the effective electrode tip area, the electrode captures the activity generated by one (single-unit) neuron or multiple (multiple-unit) neurons. The simultaneous activation of many neurons in a small space results in local field potentials [53].

Extracellular recordings have a much smaller amplitude in the order of 'µV', compared to the intracellular recordings that show action potentials in the order of 'mV'. Electrodes could be placed in various tissues (e.g., brain) or close to neurons to measure the activity. To capture the activity in peripheral nerves, scientists use microneurography.

A.7 Theoretical Bode plots of the preamplifier v2.0

The theoretical Bode plots of the preamplifier v2.0 are shown in Figure A.13. The cutoff frequency of the notch filter is at 50 Hz, the cutoff frequency of the HPF at 500 Hz, and of the LPF at 5000 Hz. Figure A.13c shows the effect of component tolerances. In this figure, we used 5% tolerance on the resistors and capacitors. We plotted the worst-case results. A waterbed effect is observed, the damping ratio ζ increases from 0.744 to 1.54.

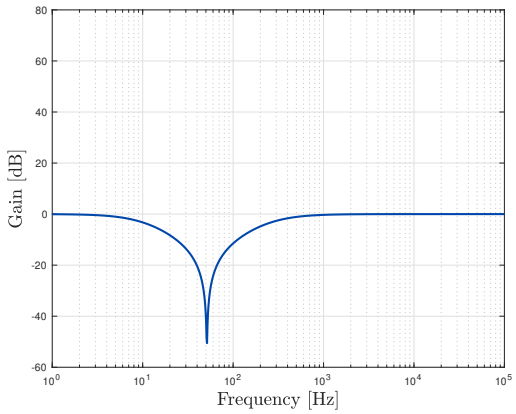

(a) Notch filter of the preamplifier v2.0.

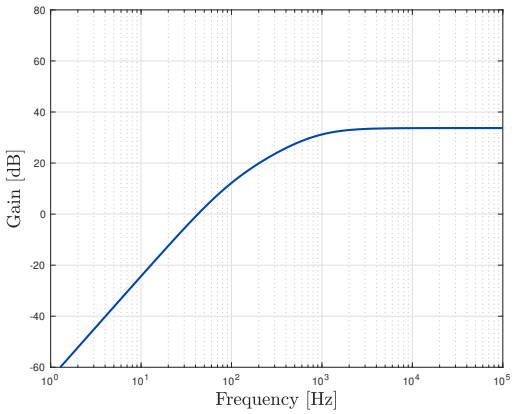

(b) High pass filter of the preamplifier v2.0.

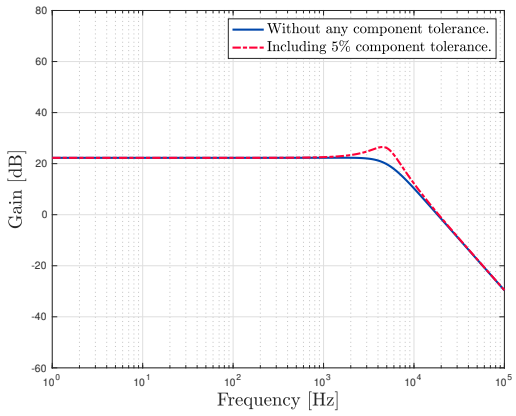

(c) Low pass filter of the preamplifier v2.0. The effect of component tolerances is also shown.

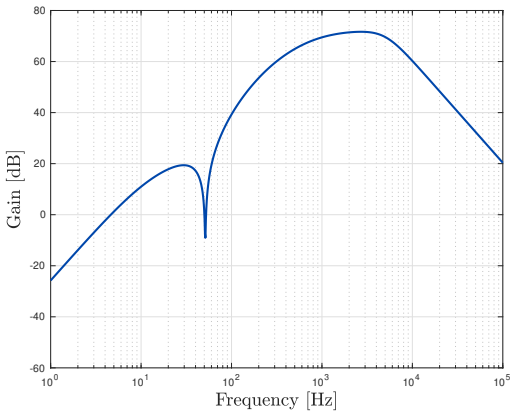

(d) Combined filters of the preamplifier v2.0.

Figure A.13: Theoretical Bode plots of the preamplifier v2.0 filters.

A.8 Preamplifier schematic

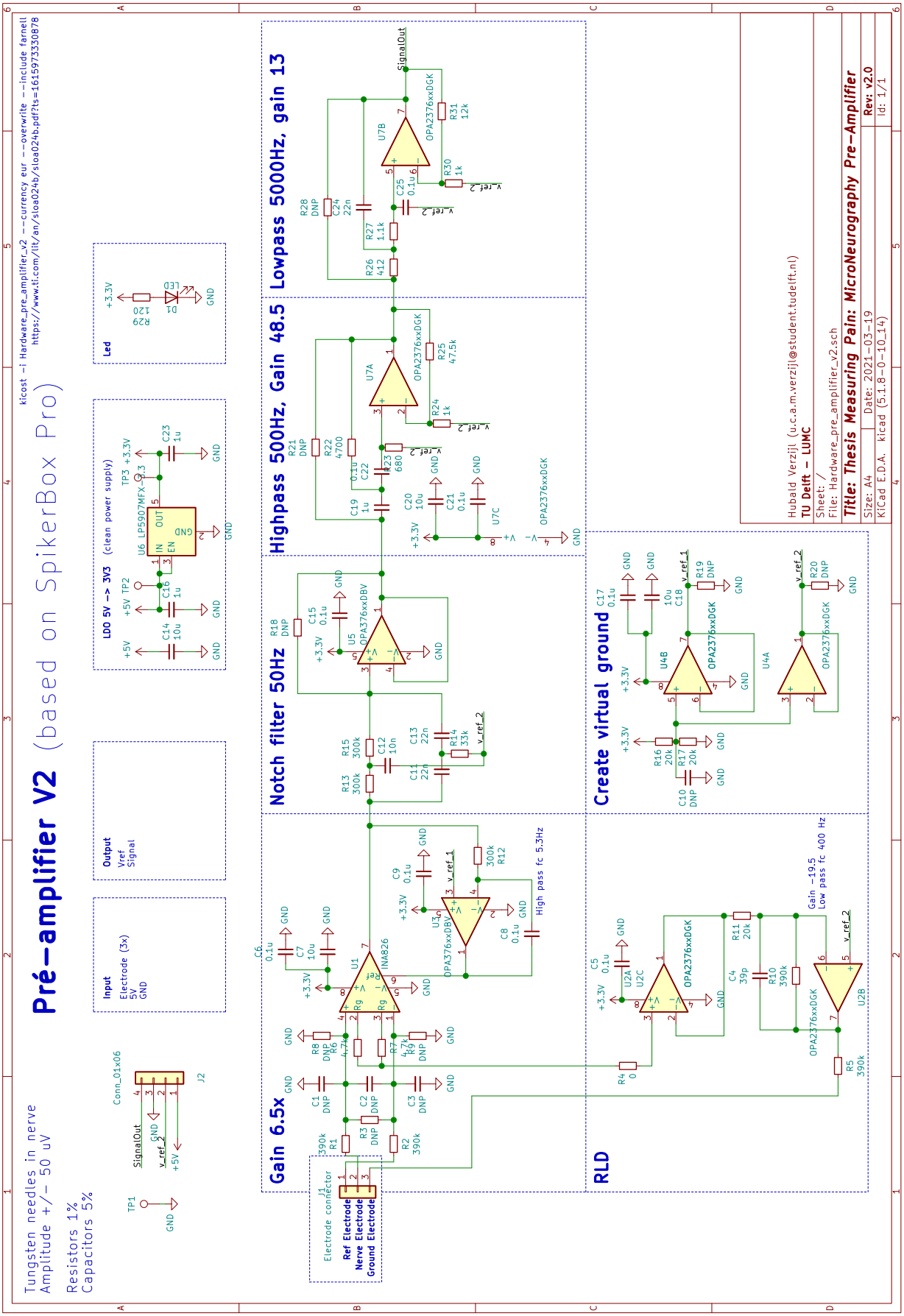

A.9 Main amplifier schematic

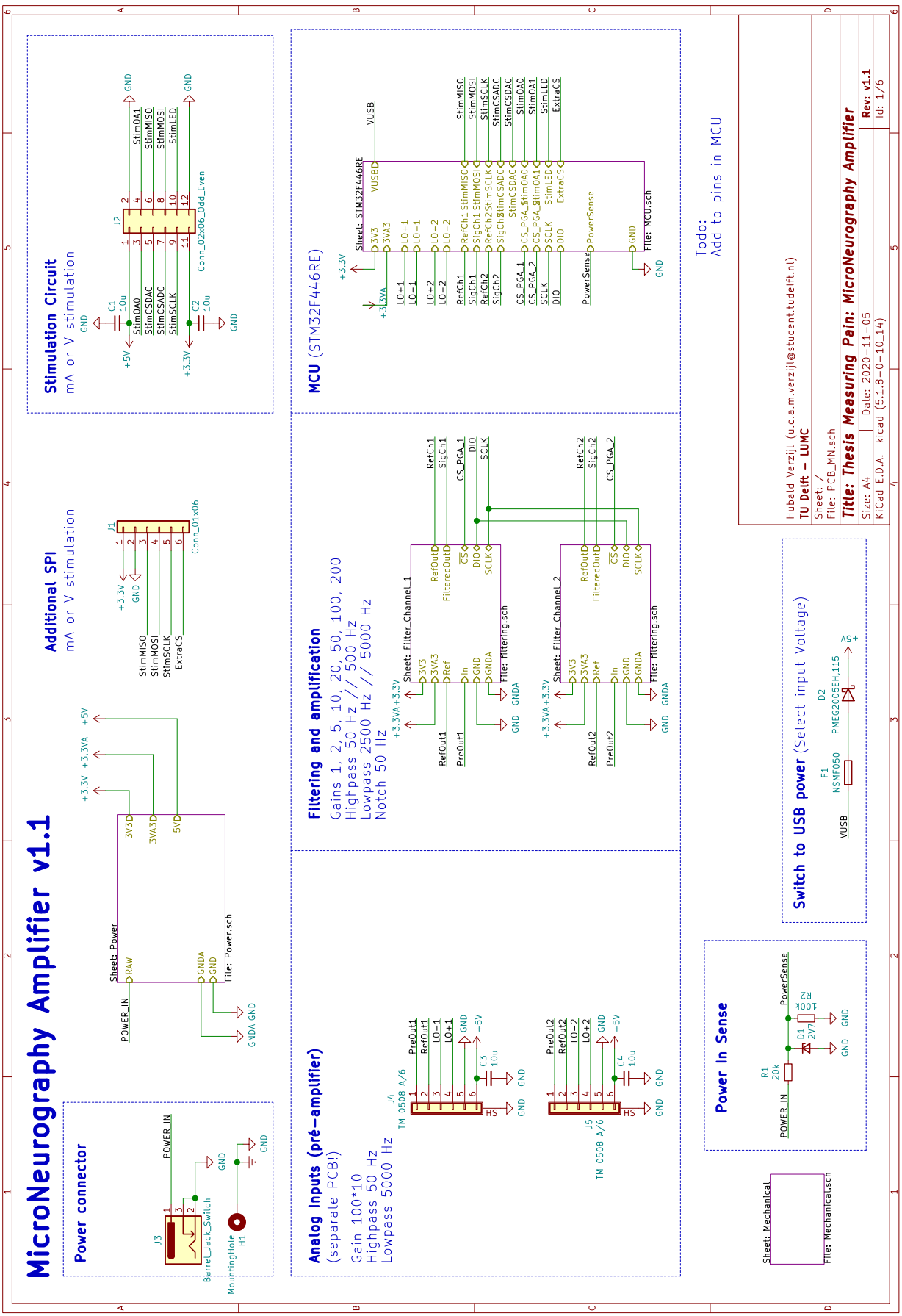

Mechanical

Mounting Holes (4 x M3)
Not to ground (prevent ground loop)

Hubald Verzijl (u.c.a.m.verzijl@student.tudelft.nl)
TU Delft – LUMC

Sheet: /Mechanical/
File: Mechanical.sch

Title: Thesis Measuring Pain: MicroNeurography Amplifier

Size: A4	Date: 2020-11-05	**Rev: v1.1**
KiCad E.D.A. kicad (5.1.8-0-10_14)		Id: 2/6

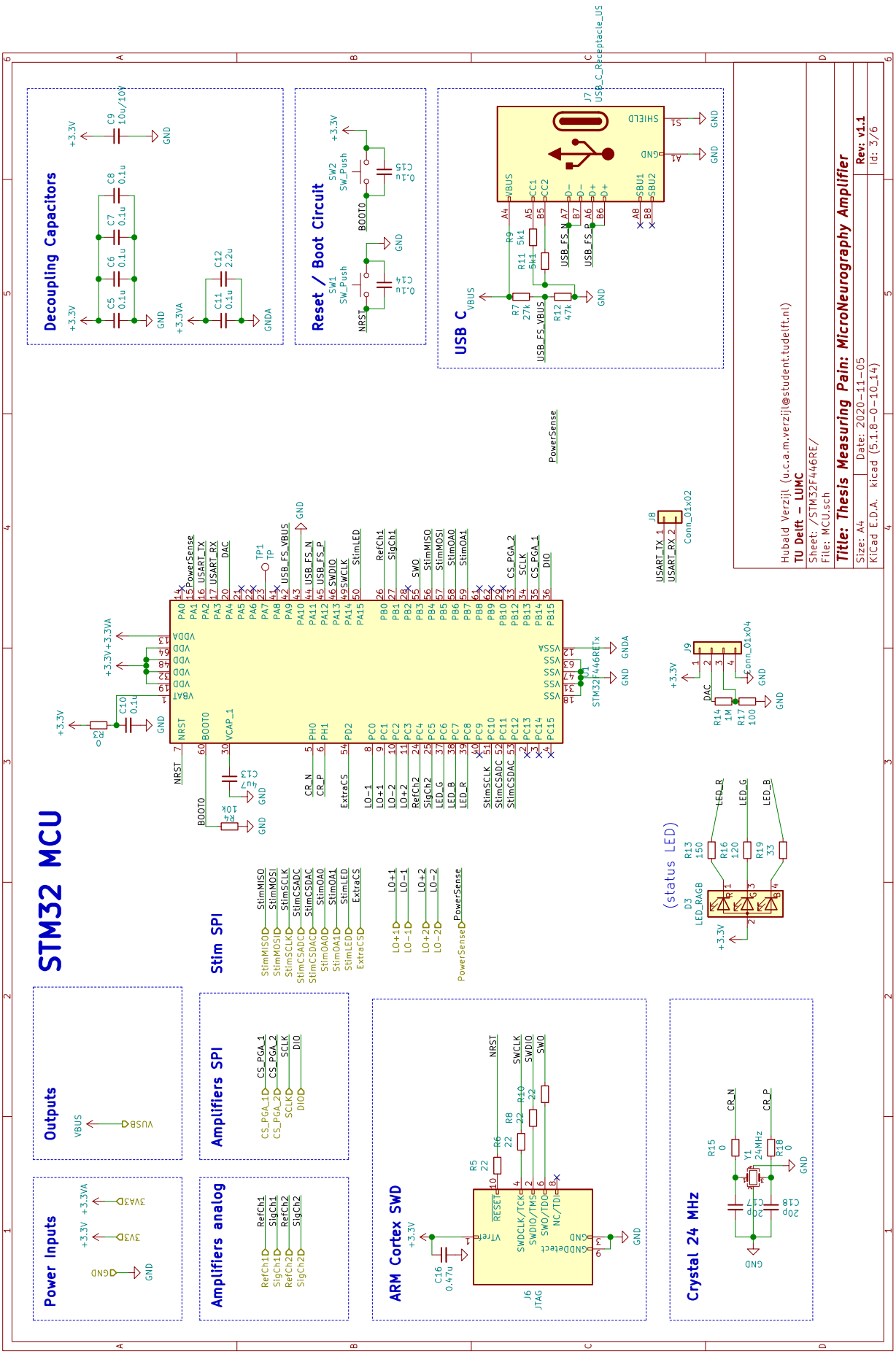
STM32 MCU
Power Inputs
Outputs
Amplifiers analog
Amplifiers SPI
Stim SPI
ARM Cortex SWD
Crystal 24 MHz
Decoupling Capacitors
Reset / Boot Circuit
USB C
(status LED)
PowerSense
Hubald Verzijl (u.c.a.m.verzijl@student.tudelft.nl)
TU Delft – LUMC
Sheet: /STM32F446RE/
File: MCU.sch
Title: Thesis Measuring Pain: MicroNeurography Amplifier
Size: A4
Date: 2020-11-05
Rev: v1.1
KiCad E.D.A. kicad (5.1.8-0-10_14)
Id: 3/6

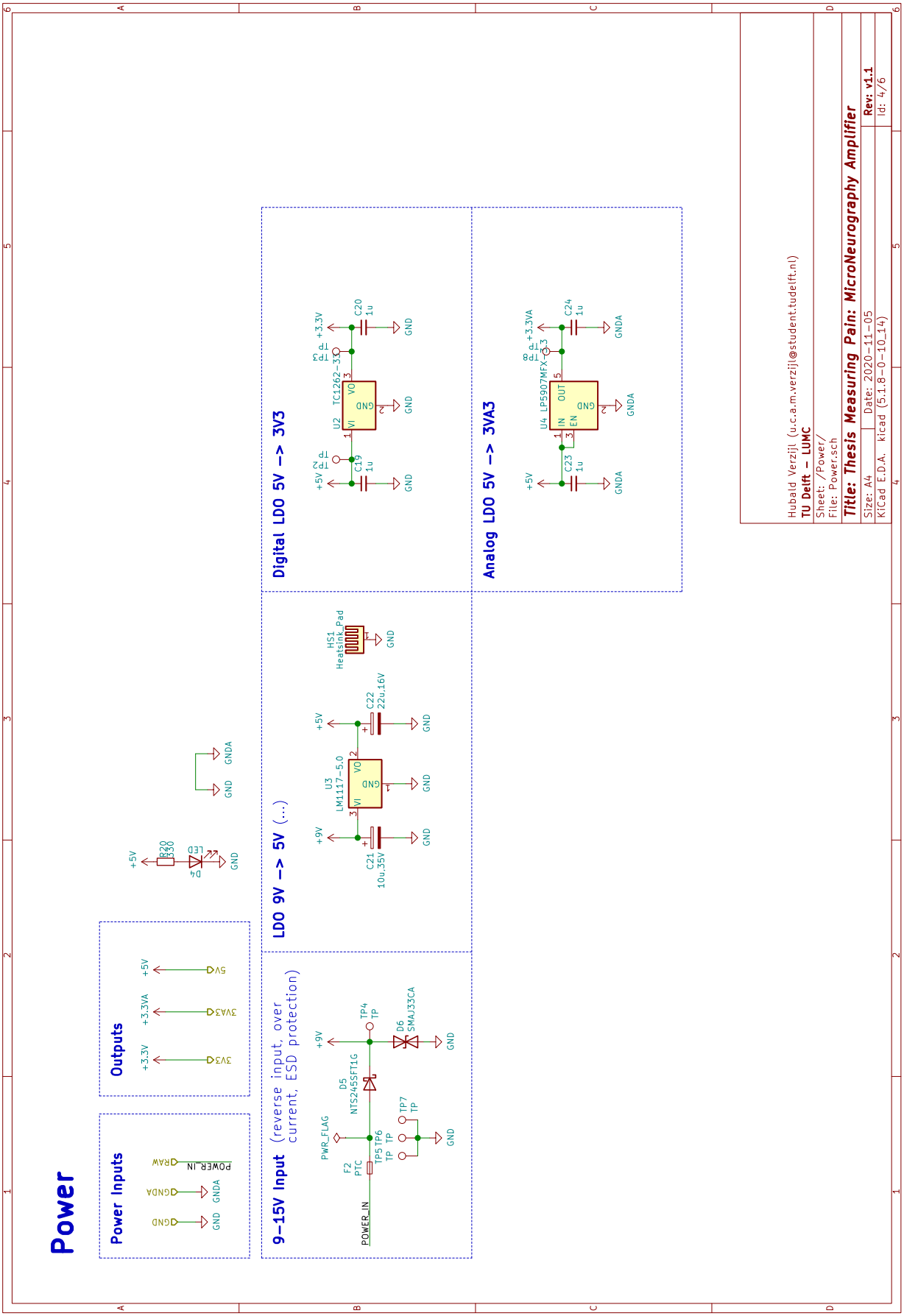
Power
Power Inputs
POWER_IN
RAW
GNDA
GND
Outputs
5V
3V3A
3V3
LED
R20
330
D4
LDO 9V –> 5V (...)
U3
LM1117-5.0
C21
10u,35V
C22
22u,16V
HS1
Heatsink Pad
9–15V Input (reverse input, over current, ESD protection)
F2
PTC
D5
NTS2455FT1G
D6
SMAJ33CA
PWR_FLAG
TP4
TP5
TP6
TP7
Digital LDO 5V –> 3V3
U2
TC1262-33
C19
1u
C20
1u
Analog LDO 5V –> 3VA3
U4
LP5907MFX-3.3
C23
1u
C24
1u
Hubald Verzijl (u.c.a.m.verzijl@student.tudelft.nl)
TU Delft – LUMC
Sheet: /Power/
File: Power.sch
Title: Thesis Measuring Pain: MicroNeurography Amplifier
Size: A4
Date: 2020-11-05
Rev: v1.1
KiCad E.D.A. kicad (5.1.8-0-10_14)
Id: 4/6

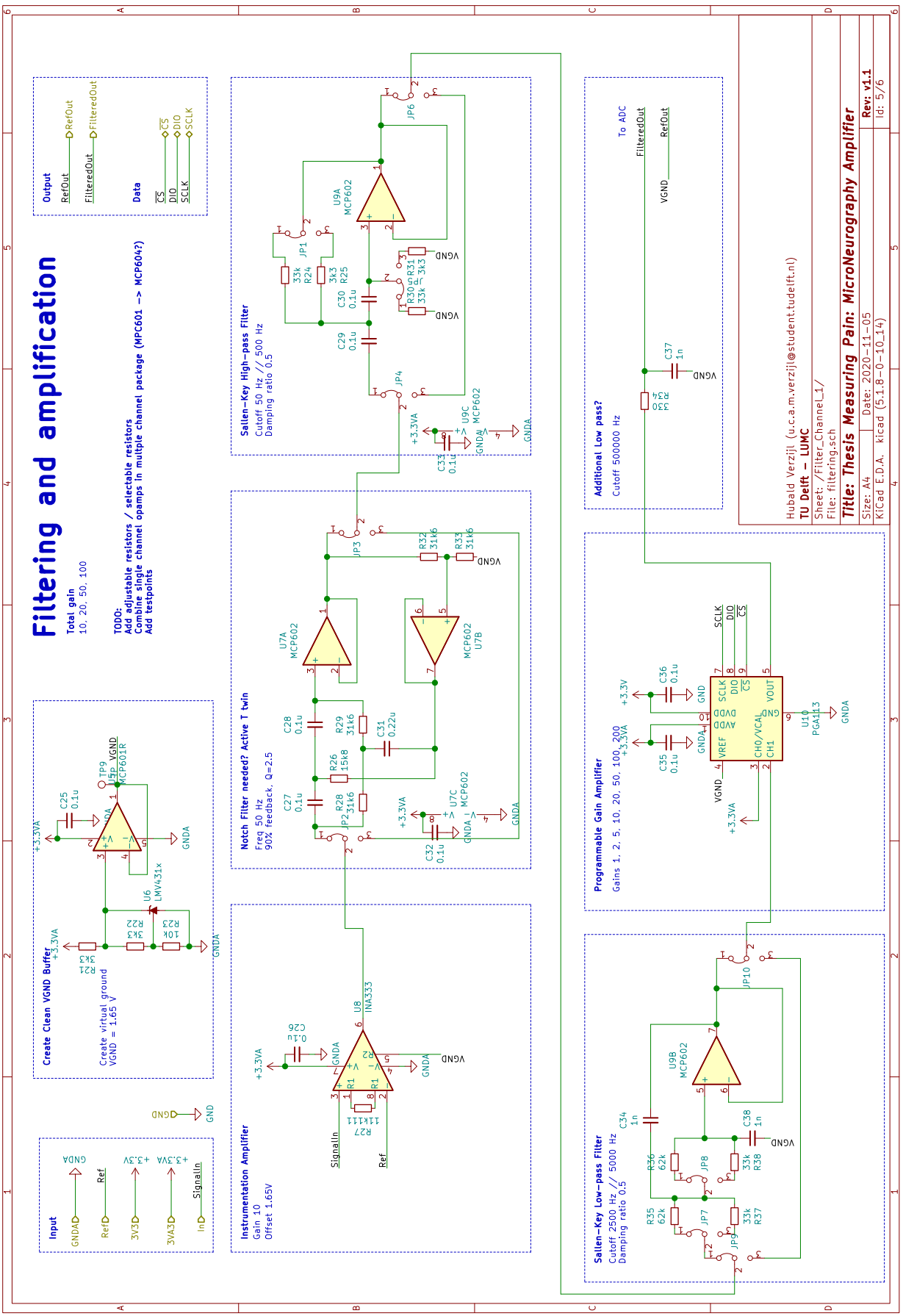
Filtering and amplification
Total gain
10, 20, 50, 100
TODO:
Add adjustable resistors / selectable resistors
Combine single channel opamps in multiple channel package (MPC601 --> MCP6042)
Add testpoints
Output
RefOut
FilteredOut
Data
CS
DIO
SCLK
Create Clean VGND Buffer
Create virtual ground
VGND = 1.65 V
Sallen-Key High-pass Filter
Cutoff 50 Hz // 500 Hz
Damping ratio 0.5
Notch Filter needed? Active T twin
Freq 50 Hz
90% feedback, Q=2.5
Instrumentation Amplifier
Gain 10
Offset 1.65V
Programmable Gain Amplifier
Gains 1. 2. 5. 10. 20. 50. 100. 200
Additional Low pass?
Cutoff 500000 Hz
Sallen-Key Low-pass Filter
Cutoff 2500 Hz // 5000 Hz
Damping ratio 0.5
Input
GNDA
Ref
3V3D
3VA3D
SignalIn
GND
To ADC
Hubald Verzijl (u.c.a.m.verzijl@student.tudelft.nl)
TU Delft – LUMC
Sheet: /Filter_Channel_1/
File: filtering.sch
Title: Thesis Measuring Pain: MicroNeurography Amplifier
Size: A4
Date: 2020-11-05
KiCad E.D.A. kicad (5.1.8-0-10_14)
Rev: v1.1
Id: 5/6

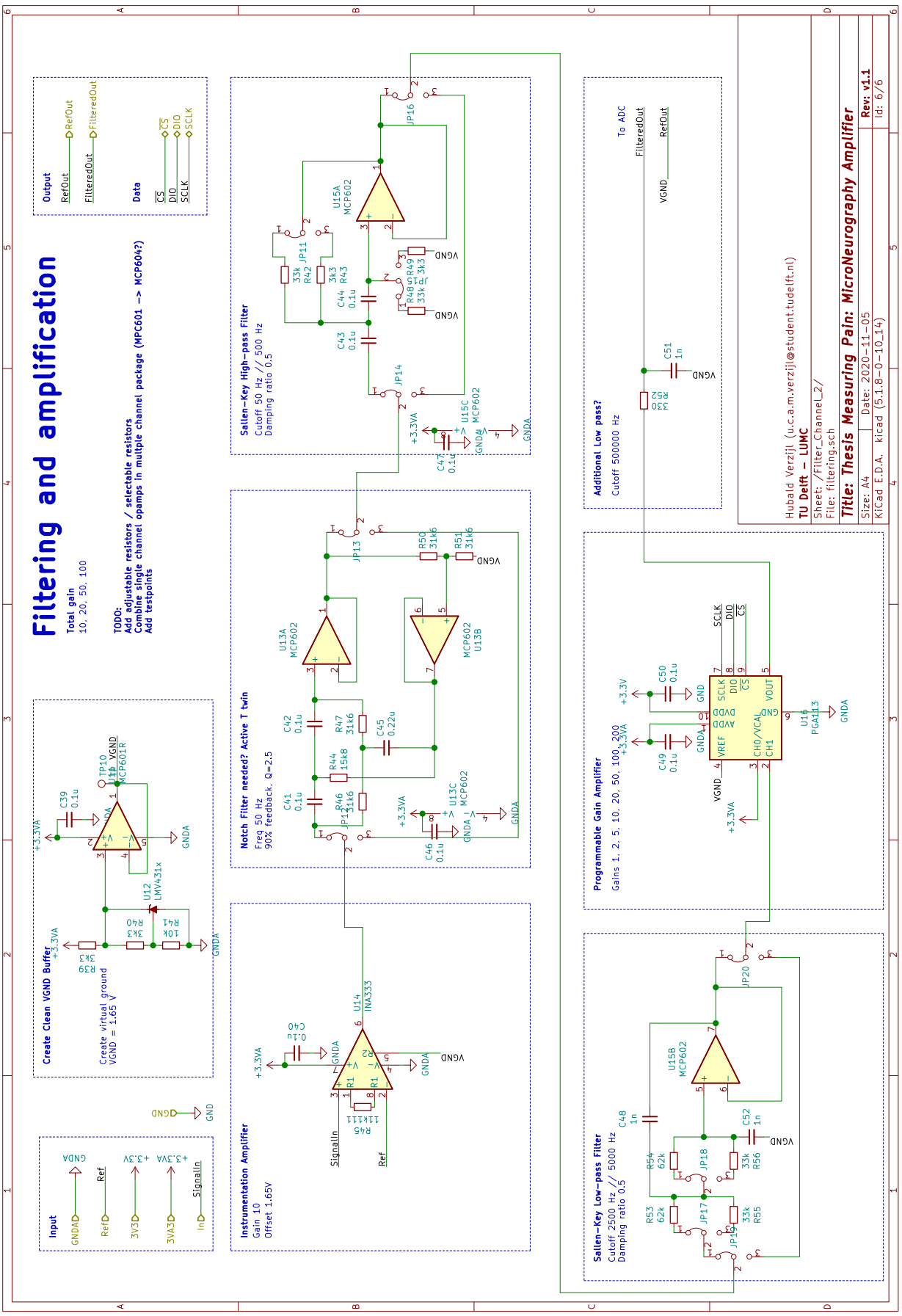
Filtering and amplification
Total gain
10, 20, 50, 100
TODO:
Add adjustable resistors / selectable resistors
Combine single channel opamps in multiple channel package (MPC601 --> MCP6042)
Add testpoints
Output
RefOut
FilteredOut
Data
CS
DIO
SCLK
Create Clean VGND Buffer
Create virtual ground
VGND = 1.65 V
Instrumentation Amplifier
Gain 10
Offset 1.65V
Notch Filter needed? Active T twin
Freq 50 Hz
90% feedback, Q=2.5
Sallen-Key High-pass Filter
Cutoff 50 Hz // 500 Hz
Damping ratio 0.5
Additional Low pass?
Cutoff 500000 Hz
Programmable Gain Amplifier
Gains 1. 2. 5. 10. 20. 50. 100. 200
Sallen-Key Low-pass Filter
Cutoff 2500 Hz // 5000 Hz
Damping ratio 0.5
Input
GNDA
Ref
3V3D
3VA3D
SignalIn
GND
Hubald Verzijl (u.c.a.m.verzijl@student.tudelft.nl)
TU Delft – LUMC
Sheet: /Filter_Channel_2/
File: filtering.sch
Title: Thesis Measuring Pain: MicroNeurography Amplifier
Size: A4
Date: 2020-11-05
KiCad E.D.A. kicad (5.1.8-0-10_14)
Rev: v1.1
Id: 6/6

A.10 Main amplifier PCB regions

We divided the design of the main amplifier into several regions, as illustrated in Figure A.14. Below, we enumerate the different regions:

- *Preamplifier 1 circuit*: The preamplifier is connected through the connector on the right. The first stage is the IA (U8). Next, opamp U7 is used to implement the notch filter. U9 creates the low- and high-pass (Sallen-Key) filters. The resistors and capacitors define the gain and cutoff frequencies of the different filtering stages. The different jumpers (e.g., JP2, JP3, and JP4) can select a different cutoff frequency or disable the selected filter stage. Finally, IC U10 embeds the PGA.
- *Preamplifier 2 circuit*: Similar as the *Preamplifier 1 circuit*, but now for the second preamplifier.
- *Power circuit*: The supply voltage (9 V battery) enters this circuit at the bottom right. First, a large LDO (U3) lowers the supply voltage to 5 V. A heatsink may be used to release excess heat. The large capacitors (C21 and C22) stabilize the supply voltage, U2 lowers the voltage to 3.3 V.
- *Digital circuit*: The MCU is presented by U1, which can be programmed through the JTAG header J6. We embedded a USB-C connector (J7) for communication with the host (PC). Finally, the MCU's operation frequency is determined by crystal Y1.
- *Stimulator connector*: The basic stimulator (Chapter 3) can be connected to this port. The main amplifier provides a supply voltage and communicates with the stimulator through an SPI bus. Different hardware modules could be connected to this port.

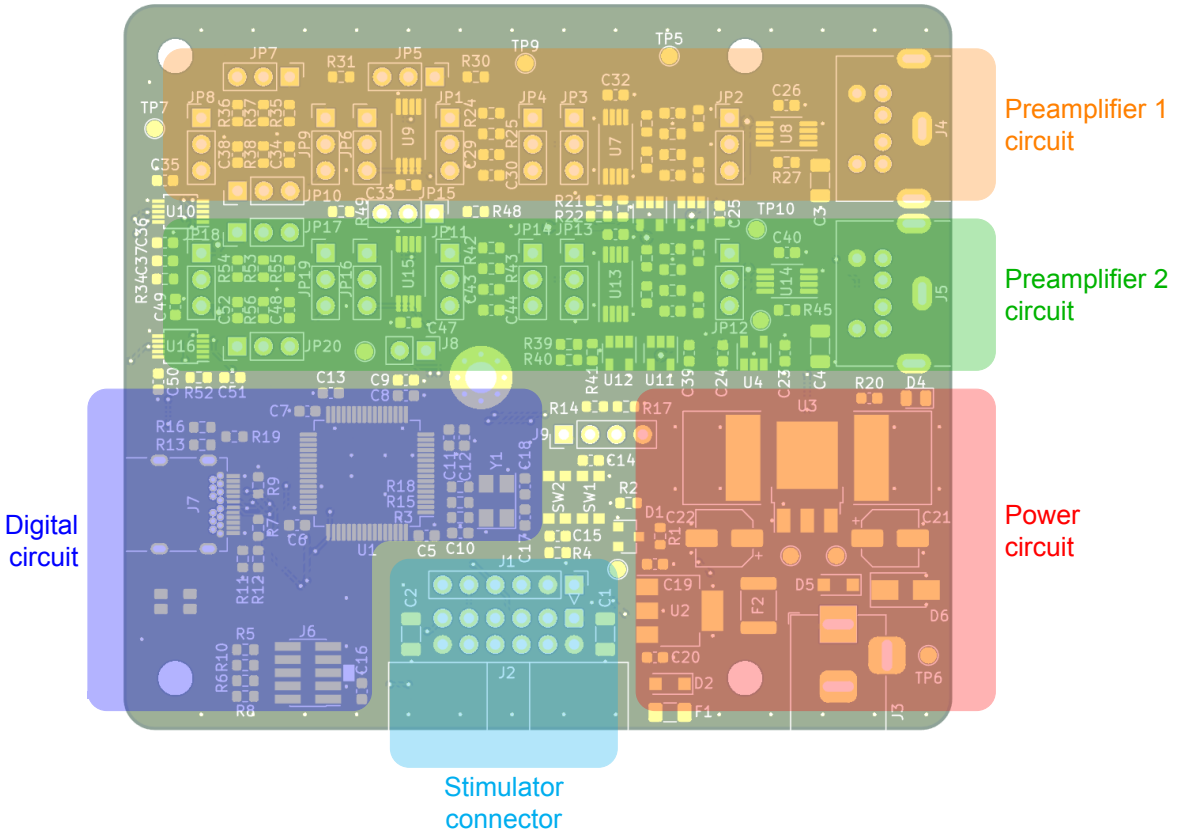

Figure A.14: Main amplifier PCB regions.

A.11 PCB assembling process

In Figure A.15 we show the different steps of the assembling process of the preamplifier (v1.0), the main amplifier, and the stimulator PCB.

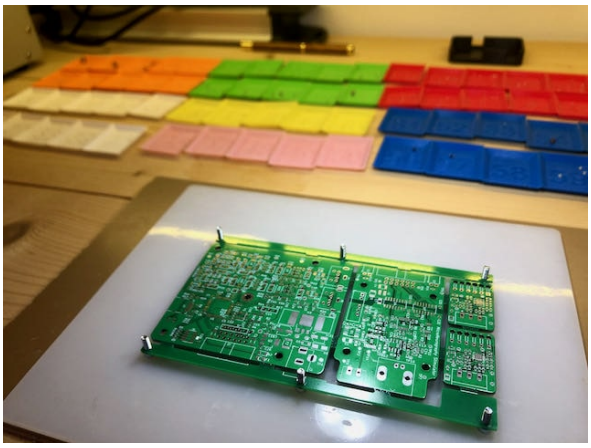

(a) Required parts are sorted in the trays (shown at the top). The PCB was ordered as a panel.

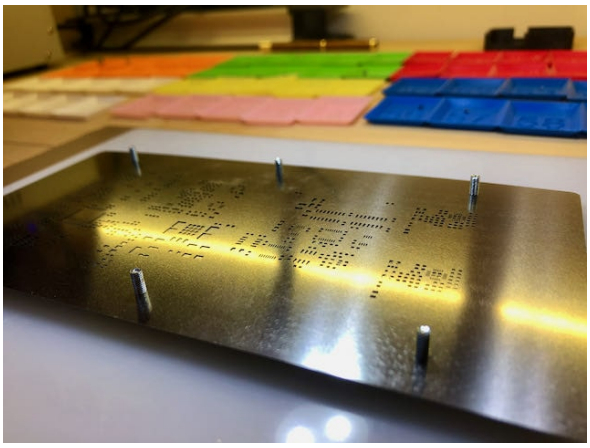

(b) A stencil is placed at the PCB to apply the correct amount of solder paste. The stencil is aligned using bolts.

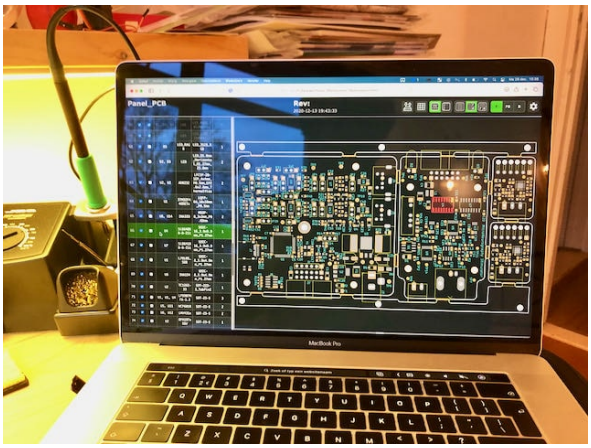

(c) The *interactive HTML BOM* plugin for `KiCad` simplifies the assembly: it shows where each component should be placed at the PCB.

(d) The solder paste is applied, and some *surface mount devices* (SMD) are already placed.

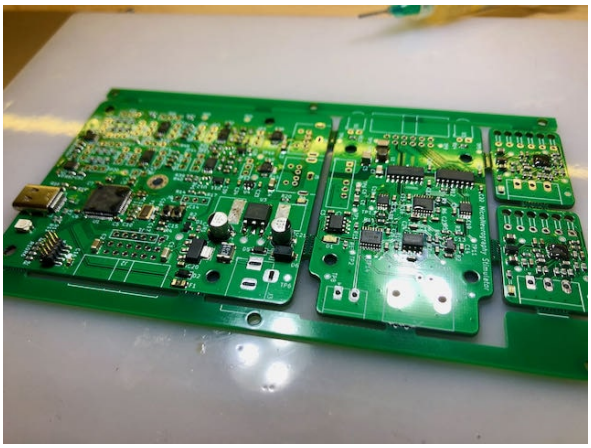

(e) After placing the SMDs, the PCB is heated, and the solder paste melts. After cooling down, the components are fixed.

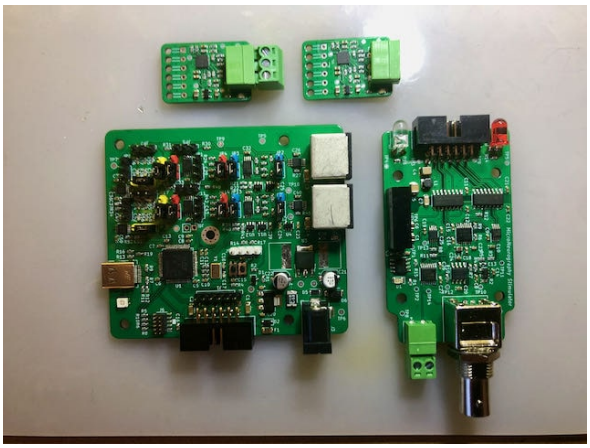

(f) The last step is assembling the through-hole components by hand soldering. After that, the boards can be separated.

Figure A.15: Assembling process of the preamplifier (v1.0), the main amplifier, and the stimulator PCB.

A.12 Stimulator power efficiency

Figure A.16 shows a constant-current topology. This circuit uses a sense resistor R_{sense} to keep the voltage constant by controlling a transistor. The sense resistor is constant, the current through the load R_{load} will be constant too, independent of the applied load [84]. Consider, e.g., a tissue impedance of $R_{tissue} = 10\,\text{k}\Omega$, a stimulation current of $I_{stim} = 0.1\,\text{mA}$ and a supply voltage of $V_{DD} = 3\,\text{V}$. This results in a voltage drop of 1 V across the load (e.g., the tissue). The voltage drop across the current driver will be 2 V, which results in a power loss of 0.2 mW in the current driver. Therefore, the system, as shown in Figure A.16, is in an inefficient system. In the case of an implantable device (which often has a battery as a power source), an inefficient system results in reduced battery life.

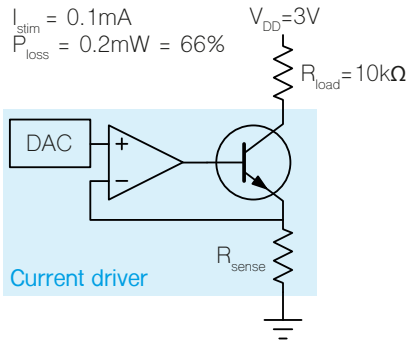

Figure A.16: Custom schematic of a possible current driver topology. A constant R_{sense} is used to create a constant current, independent of the load. The voltage overhead is lost in the current driver.

One of the challenges is to limit the amount of lost energy. It could be limited by lowering the voltage supply towards the required voltage across the load (e.g., the electrodes). Several methods are proposed to lower the voltage. The first method generates multiple voltage supplies from the main power supply. During stimulation, the system switches to the closest minimum supply voltage required for the electrodes [94]. However, it does not result in a significant improvement due to the additional hardware that is required, since the additional hardware also requires energy [84]. A second method proposes a circuit that continuously adjusts the supply voltage [95, 96]. However, for a system containing many stimulation channels (in which many different impedance levels are involved), the supply voltage required for the lower output voltages is too high, which leads to inefficiencies [84].

Ultra-high frequency stimulation may resolve the power efficiency problem. Many small stimulation pulses may be used to build up the charge within the tissue. A current driver is in this situation not required anymore. However, the power efficiency investigation is not part of this thesis.

A.13 Basic stimulator schematic

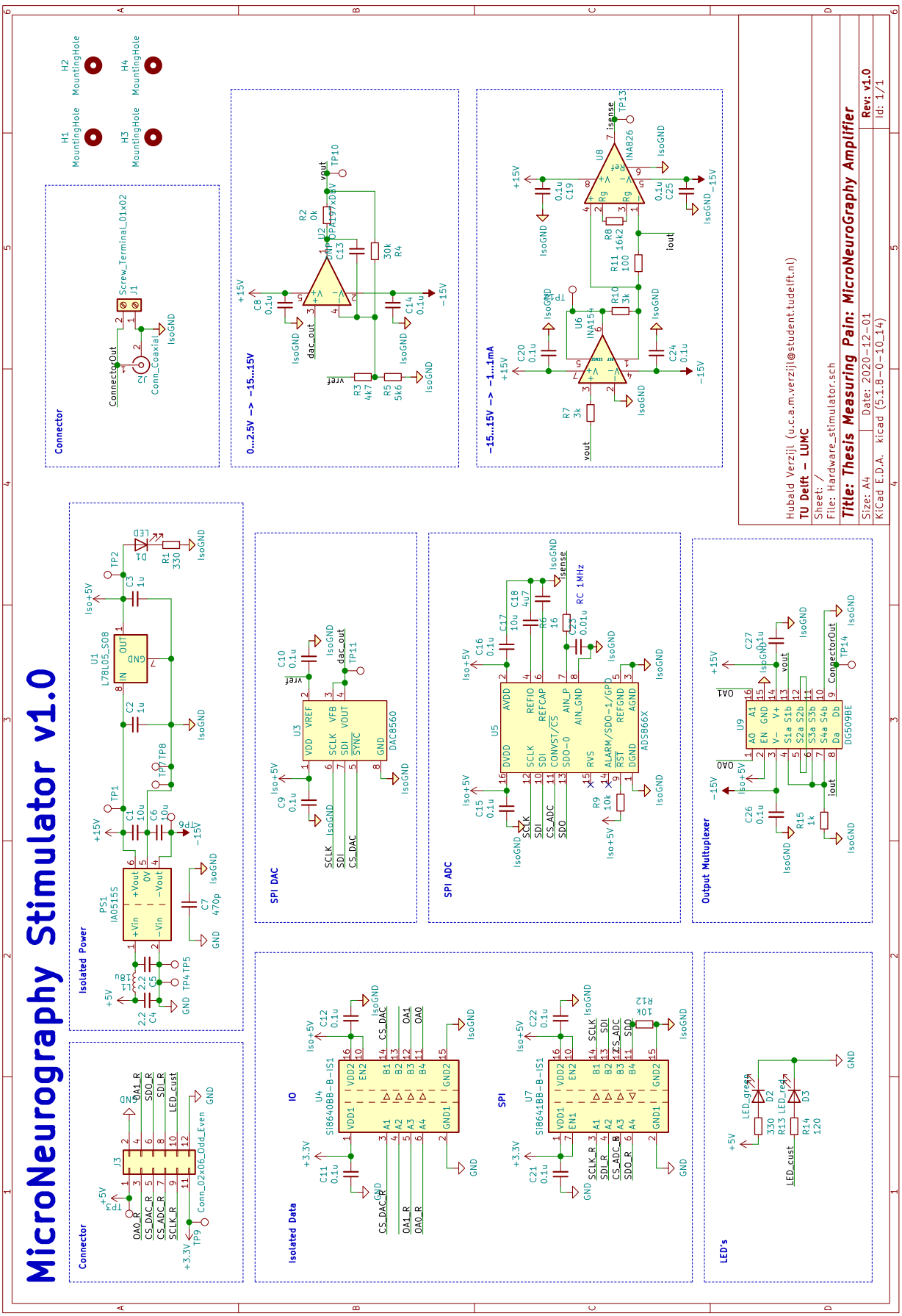

References

[1] B. H. Smith and N. Torrance. “Epidemiology of neuropathic pain and its impact on quality of life”. In: *Current Pain and Headache Reports* 16.3 (2012), pp. 191–198.

[2] J. L. Ochoa. “Neuropathic pain: Redefinition and a grading system for clinical and research purposes”. In: *Neurology* 72.14 (2009), pp. 1282–1283.

[3] C. E. Zelaya, J. M. Dahlhamer, J. W. Lucas, and E. M. Connor. “Chronic Pain and High-impact Chronic Pain Among U.S. Adults, 2019”. In: *NCHS data brief* 390 (2020), pp. 1–8.

[4] B. H. Smith, H. L. Hébert, and A. Veluchamy. “Neuropathic pain in the community: prevalence, impact, and risk factors”. In: *Pain* 161 (2020), S127–S137.

[5] N. Torrance, K. D. Lawson, E. Afolabi, M. I. Bennett, M. G. Serpell, K. M. Dunn, and B. H. Smith. “Estimating the burden of disease in chronic pain with and without neuropathic characteristics: Does the choice between the EQ-5D and SF-6D matter?” In: *Pain* 155.10 (2014), pp. 1996–2004.

[6] J. C. Ballantyne, S. M. Fishman, and J. P. Rathmell. *Bonica’s Management of Pain*. 5th ed. Lippincott Williams and Wilkins, 2018.

[7] K. Rajput, S. Reddy, and H. Shankar. “Painful Neuromas”. In: *The Clinical Journal of Pain* 28.7 (2012), pp. 639–645.

[8] H. McQuay. *Relief of Chronic Non-Malignant Pain*. URL: `http://www.bandolier.org.uk/booth/painpag/wisdom/493HJM.html` (visited on 10/20/2021).

[9] R. A. Moore, S. Derry, D. Aldington, P. Cole, and P. J. Wiffen. “Amitriptyline for neuropathic pain in adults”. In: *Cochrane Database of Systematic Reviews* 7 (2015).

[10] A. B. O’Connor and R. H. Dworkin. “Treatment of Neuropathic Pain: An Overview of Recent Guidelines”. In: *The American Journal of Medicine* 122.10 (2009), S22–S32.

[11] F. Kompas. *Amitriptyline*. 2002. URL: `https://www.farmacotherapeutischkompas.nl/bladeren/preparaatteksten/a/amitriptyline` (visited on 10/06/2021).

[12] J. Lewin-Kowalik, W. Marcol, K. Kotulska, M. Mandera, and A. Klimczak. “Prevention and management of painful neuroma”. In: *Neurologia Medico-Chirurgica* 46.2 (2006), pp. 62–67.

[13] L. H. Poppler, R. P. Parikh, M. J. Bichanich, K. Rebehn, C. R. Bettlach, S. E. Mackinnon, and A. M. Moore. “Surgical interventions for the treatment of painful neuroma: A comparative meta-analysis”. In: *Pain* 159.2 (2018), pp. 214–223.

[14] M. Devor and M. Tal. “Nerve resection for the treatment of chronic neuropathic pain”. In: *Pain* 155.6 (2014), pp. 1053–1054.

[15] G. Colini Baldeschi, A. Dario, G. De Carolis, N. Luxardo, M. Natale, P. Nosella, A. Papa, M. Raggi, and C. Reverberi. “Peripheral Nerve Stimulation in the Treatment of Chronic Pain Syndromes From Nerve Injury: A Multicenter Observational Study”. In: *Neuromodulation* 20.4 (2017), pp. 369–374.

[16] P. Verrills, C. Sinclair, and A. Barnard. “A review of spinal cord stimulation systems for chronic pain”. In: *Journal of Pain Research* Volume 9 (2016), pp. 481–492.

[17] F. T. Sun and M. J. Morrell. “Closed-loop Neurostimulation: The Clinical Experience”. In: *Neurotherapeutics* 11.3 (2014), pp. 553–563.

[18] Y. Liu, A. Urso, R. Martins, T. Costa, V. Valente, V. Giagka, W. A. Serdijn, T. G. Constandinou, and T. Denison. “Bidirectional Bioelectronic Interfaces”. In: *IEEE Solid State Circuits Magazine* 12.2 (2020), pp. 30–46.

[19] J. D. England, L. T. Happel, D. G. Kline, F. Gamboni, C. L. Thouron, Z. P. Liu, and S. R. Levinson. “Sodium channel accumulation in humans with painful neuromas”. In: *Neurology* 47.1 (1996), pp. 272–276.

[20] J. D. England, L. T. Happel, Z. Liu, C. L. Thouron, and D. G. Kline. “Abnormal distributions of potassium channels in human neuromas”. In: *Neuroscience Letters* 255.1 (1998), pp. 37–40.

[21] E. V. Bird, C. R. Christmas, A. R. Loescher, K. G. Smith, P. P. Robinson, J. A. Black, S. G. Waxman, and F. M. Boissonade. “Correlation of Nav1.8 and Nav1.9 Sodium Channel Expression with Neuropathic Pain in Human Subjects with Lingual Nerve Neuromas”. In: *Molecular Pain* 9.1 (2013), pp. 1744–8069.

[22] M. Devor. “Neuropathic Pain: Pathophysiological Response of Nerves to Injury”. In: *Wall & Melzack’s Textbook of Pain*. Elsevier B.V., 2006, pp. 861–888.

[23] R. Amir, M. Michaelis, and M. Devor. “Membrane potential oscillations in dorsal root ganglion neurons: Role in normal electrogenesis and neuropathic pain”. In: *Journal of Neuroscience* 19.19 (1999), pp. 8589–8596.

[24] Y. Kovalsky, R. Amir, and M. Devor. “Simulation in sensory neurons reveals a key role for delayed Na+ current in subthreshold oscillations and ectopic discharge: Implications for neuropathic pain”. In: *Journal of Neurophysiology* 102.3 (2009), pp. 1430–1442.

[25] Y.-A. Rho and S. A. Prescott. “Identification of Molecular Pathologies Sufficient to Cause Neuropathic Excitability in Primary Somatosensory Afferents Using Dynamical Systems Theory”. In: *PLoS Computational Biology* 8.5 (2012). Ed. by B. S. Gutkin, e1002524.

[26] A. L. Shilnikov and N. F. Rulkov. “Subthreshold oscillations in a map-based neuron model”. In: *Physics Letters, Section A: General, Atomic and Solid State Physics* 328.2-3 (2004), pp. 177–184.

[27] T. Mano, S. Iwase, and S. Toma. “Microneurography as a tool in clinical neurophysiology to investigate peripheral neural traffic in humans”. In: *Clinical Neurophysiology* 117.11 (2006), pp. 2357–2384.

[28] F. M. Petrini, A. Mazzoni, J. Rigosa, F. Giambattistelli, G. Granata, B. Barra, A. Pampaloni, E. Guglielmelli, L. Zollo, M. Capogrosso, S. Micera, and S. Raspopovic. “Microneurography as a tool to develop decoding algorithms for peripheral neuro-controlled hand prostheses”. In: *BioMedical Engineering OnLine* 18.1 (2019), p. 44.

[29] S. Luan, I. Williams, K. Nikolic, and T. G. Constandinou. “Neuromodulation: present and emerging methods”. In: *Frontiers in Neuroengineering* 7 (2014), pp. 1–9.

[30] P. Vannemreddy and K. Slavin. “Spinal cord stimulation: Current applications for treatment of chronic pain”. In: *Anesthesia: Essays and Researches* 5.1 (2011), pp. 20–27.

[31] N. Mekhail, R. M. Levy, T. R. Deer, L. Kapural, S. Li, K. Amirdelfan, C. W. Hunter, S. M. Rosen, S. J. Costandi, S. M. Falowski, A. H. Burgher, J. E. Pope, C. A. Gilmore, F. A. Qureshi, P. S. Staats, J. Scowcroft, J. Carlson, C. K. Kim, M. I. Yang, T. Stauss, L. Poree, D. Brounstein, R. Gorman, G. E. Gmel, E. Hanson, D. M. Karantonis, A. Khurram, D. Kiefer, A. Leitner, D. Mugan, M. Obradovic, J. Parker, P. Single, and N. Soliday. “Long-term safety and efficacy of closed-loop spinal cord stimulation to treat chronic back and leg pain (Evoke): a double-blind, randomised, controlled trial”. In: *The Lancet Neurology* 19.2 (2020), pp. 123–134.

[32] L. Lundy-Ekman. *Neuroscience: Fundamentals for Rehabilitation*. 4th ed. Elsevier - Health Sciences Division, 2012.

[33] B. Friedland. *Control System Design: An Introduction to State-Space Methods*. Dover Books on Electrical Engineering. Dover Publications, 2005.

[34] K. Åström and B. Wittenmark. *Computer-Controlled Systems: Theory and Design*. 3rd ed. Prentice Hall, 1997.

[35] A. L. Hodgkin and A. F. Huxley. “A quantitative description of membrane current and its application to conduction and excitation in nerve”. In: *The Journal of Physiology* 117.4 (1952), pp. 500–544.

[36] R. Amir and M. Devor. “Spike-evoked suppression and burst patterning in dorsal root ganglion neurons of the rat”. In: *Journal of Physiology* 501.1 (1997), pp. 183–196.

[37] C. Morris and H. Lecar. “Voltage oscillations in the barnacle giant muscle fiber”. In: *Biophysical Journal* 35.1 (1981), pp. 193–213.

[38] B. Ibarz, J. Casado, and M. Sanjuán. “Map-based models in neuronal dynamics”. In: *Physics Reports* 501.1-2 (2011), pp. 1–74.

[39] S. J. Qin and T. A. Badgwell. “A survey of industrial model predictive control technology”. In: *Control Engineering Practice* 11 (2003), pp. 733–764.

[40] K. Liu, Y. Q. Chen, and X. Zhang. “An evaluation of ARFIMA (autoregressive fractional integral moving average) programs”. In: *Axioms* 6.2 (2017).

[41] J. E. Vera-Valdés. “On long memory origins and forecast horizons”. In: *Journal of Forecasting* 39.5 (2020), pp. 811–826.

[42] G. Gupta, S. Pequito, and P. Bogdan. “Dealing with Unknown Unknowns: Identification and Selection of Minimal Sensing for Fractional Dynamics with Unknown Inputs”. In: *2018 Annual American Control Conference (ACC)*. IEEE, 2018, pp. 2814–2820.

[43] S. Chatterjee, O. Romero, A. Ashourvan, and S. D. Goncalves Melo Pequito. “Fractional-order model predictive control as a framework for electrical neurostimulation in epilepsy”. In: *Journal of Neural Engineering* September (2020), pp. 1–18.

[44] A. Scheiner, J. T. Mortimer, and U. Roessmann. “Imbalanced Biphasic Electrical Stimulation: Muscle Tissue Damage”. In: *Annals of Biomedical Engineering* 18 (1990), pp. 407–425.

[45] M. Aminoff. *Aminoff’s Electrodiagnosis in Clinical Neurology*. Saunders, 2012.

[46] D. Boinagrov, J. Loudin, and D. Palanker. “Strength-duration relationship for extracellular neural stimulation: Numerical and analytical models”. In: *Journal of Neurophysiology* 104.4 (2010), pp. 2236–2248.

[47] L. Lundy-Ekman. *Neuroscience : fundamentals for rehabilitation*. St. Louis, Missouri: Elsevier, 2018.

[48] T. Apland. *Nervous system in man, Nerve cells types & Nature of nerve impulse*. 2018. URL: https://www.tamiapland.com/blog/2018/8/7/fascial-layers-part-2-anatomy-of-a-nerve (visited on 05/13/2021).

[49] H. Soffar. *Nervous system in man, Nerve cells types & Nature of nerve impulse*. 2018. URL: https://www.online-sciences.com/biology/nervous-system-in-man-nerve-cells-types-nature-of-nerve-impulse/ (visited on 03/03/2021).

[50] M. Raghavan, D. Fee, and P. E. Barkhaus. *Generation and propagation of the action potential*. 1st ed. Vol. 160. Elsevier B.V., 2019, pp. 3–22.

[51] I. Varga and B. Mravec. *Nerve Fiber Types*. Vol. 1. Elsevier Ltd., 2015, pp. 107–113.

[52] C. L. Hill and G. J. Stephens. “An Introduction to Patch Clamp Recording”. In: *Patch Clamp Electrophysiology: Methods and Protocols*. Ed. by M. Dallas and D. Bell. New York, NY: Springer US, 2021, pp. 1–19.

[53] O. Herreras. “Local field potentials: Myths and misunderstandings”. In: *Frontiers in Neural Circuits* 10.DEC (2016), pp. 1–16.

[54] T. Sprung. *A successful median nerve challenge with lots of beautiful recordings*. 2015. URL: https://twitter.com/torisprung/status/633819196388868096 (visited on 06/09/2021).

[55] Å. B. Vallbo. “Microneurography: How it started and how it works”. In: *Journal of Neurophysiology* 120.3 (2018), pp. 1415–1427.

[56] J. Inglis, J. B. Leeper, D. Burke, and S. C. Gandevia. “Morphology of action potentials recorded from human nerves using microneurography”. In: *Experimental Brain Research* 110.2 (1996), pp. 308–314.

[57] Å. Vallbo, L. Löken, and J. Wessberg. “Sensual Touch: A Slow Touch System Revealed with Microneurography”. In: *Affective Touch and the Neurophysiology of CT Afferents*. New York, NY: Springer New York, 2016, pp. 1–30.

[58] J. H. Nagel. “Biopotential Amplifiers”. In: *The Biomedical Engineering Handbook: Second Edition*. CRC Press, 2000, pp. 301–309.

[59] V. Acharya. *Improving Common-Mode Rejection Using the Right-Leg Drive Amplifier*. 2011. URL: https://e2e.ti.com/cfs-file/__key/communityserver-discussions-components-files/73/Improving-Common_2D00_Mode-Rejection-Using-the-Right_2D00_Leg-Driver-Amplifier.pdf (visited on 09/22/2021).

[60] ADInstruments. *Microneurography*. 2021. URL: https://www.adinstruments.com/research/human/autonomic/microneurography (visited on 09/22/2021).

[61] J. Serra, H. Bostock, R. Solà, J. Aleu, E. García, B. Cokic, X. Navarro, and C. Quiles. "Microneurographic identification of spontaneous activity in C-nociceptors in neuropathic pain states in humans and rats". In: *Pain* 153.1 (2012), pp. 42–55.

[62] V. G. Macefield. "Recording and quantifying sympathetic outflow to muscle and skin in humans: methods, caveats and challenges". In: *Clinical Autonomic Research* 31.1 (2021), pp. 59–75.

[63] R. Getz. *Activity: Cascaded RC low pass filters*. 2021. URL: https://wiki.analog.com/university/courses/alm1k/circuits1/alm-cir-cascade-rc (visited on 09/21/2021).

[64] J. Karki. *Analysis of the Sallen-Key Architecture*. 2002. URL: https://www.ti.com/lit/an/sloa024b/sloa024b.pdf?ts=1629276460691 (visited on 09/21/2021).

[65] ADIEngineerZone. *How does the right leg drive technique work?* 2021. URL: https://ez.analog.com/amplifiers/w/documents/1847/how-does-the-right-leg-drive-technique-work (visited on 09/22/2021).

[66] I. Zepeda-Carapia, A. Marquez-Espinoza, and C. Alvarado-Serrano. "Measurement of Skin-Electrode Impedance for a 12-lead Electrocardiogram". In: *2005 2nd International Conference on Electrical and Electronics Engineering*. Vol. 2005. IEEE, 2005, pp. 193–195.

[67] E. W. Weisstein. *Fourier Series–Square Wave*. URL: https://mathworld.wolfram.com/FourierSeriesSquareWave.html (visited on 09/22/2021).

[68] B. Brains. *Neuron SpikerBox*. URL: https://backyardbrains.com/products/spikerbox (visited on 09/22/2021).

[69] O. E. Design. *Twin-T Notch Filter Design Tool*. URL: http://sim.okawa-denshi.jp/en/TwinTCRkeisan.htm (visited on 09/22/2021).

[70] S. Labs. *AN118: Improving ADC resolution by oversampling and averaging*. URL: https://www.silabs.com/documents/public/application-notes/an118.pdf (visited on 09/24/2021).

[71] S. K. Lam, A. Pitrou, and S. Seibert. "Numba". In: *Proceedings of the Second Workshop on the LLVM Compiler Infrastructure in HPC - LLVM '15*. New York, New York, USA: ACM Press, 2015, pp. 1–6.

[72] K. Stam. *The Long-Held Secret Of Lugworms*. 2020. URL: https://www.futurefrogmen.org/blog/2020/12/5/the-long-kept-secret-of-lugworms (visited on 10/18/2021).

[73] B. Cummings. *Earthworms*. URL: https://www.sas.upenn.edu/~rlenet/Earthworms.html (visited on 10/18/2021).

[74] J. Serra, H. Bostock, and X. Navarro. "Microneurography in rats: A minimally invasive method to record single C-fiber action potentials from peripheral nerves in vivo". In: *Neuroscience Letters* 470.3 (2010), pp. 168–174.

[75] V. Tognon-Miguel, A. H. d. Nascimento-Elias, M. C. L. Schiavoni, and A. A. Barreira. "A histomorphometric study of unmyelinated fibers of the fibular nerve in Wistar rats". In: *Arquivos de Neuro-Psiquiatria* 74.5 (2016), pp. 367–372.

[76] H. Schmalbruch. "Fiber composition of the rat sciatic nerve". In: *The Anatomical Record* 215.1 (1986), pp. 71–81.

[77] R. N. Scott, L. McLean, and P. A. Parker. "Stimulus artefact in somatosensory evoked potential measurement". In: *Medical & Biological Engineering & Computing* 35.3 (1997), pp. 211–215.

[78] M. M. Ottaviani, L. Wright, T. Dawood, and V. G. Macefield. "In vivo recordings from the human vagus nerve using ultrasound□guided microneurography". In: *The Journal of Physiology* 598.17 (2020), pp. 3569–3576.

[79] C. Drewes. *Functional organization of the nervous system in Lumbriculus variegatus*. 2002. URL: https://www.eeob.iastate.edu/faculty/DrewesC/htdocs/LVCNSa.htm (visited on 09/27/2021).

[80] K. M. Shannon, G. J. Gage, A. Jankovic, W. J. Wilson, and T. C. Marzullo. “Portable conduction velocity experiments using earthworms for the college and high school neuroscience teaching laboratory”. In: *Advances in Physiology Education* 38.1 (2014), pp. 62–70.

[81] X. Liu, A. Demosthenous, M. Rahal, and N. Donaldson. “Recent advances in the design of implantable stimulator output stages”. In: *2007 18th European Conference on Circuit Theory and Design*. IEEE, 2007, pp. 204–207.

[82] J. Simpson and M. Ghovanloo. “An experimental study of voltage, current, and charge controlled stimulation front-end circuitry”. In: *Proceedings - IEEE International Symposium on Circuits and Systems* (2007), pp. 325–328.

[83] A. D. Sdrulla, Y. Guan, and S. N. Raja. “Spinal Cord Stimulation: Clinical Efficacy and Potential Mechanisms”. In: *Pain Practice* 18.8 (2018), pp. 1048–1067.

[84] A. Urso, V. Giagka, M. Van Dongen, and W. A. Serdijn. “An Ultra High-Frequency 8-Channel Neurostimulator Circuit with 68 Peak Power Efficiency”. In: *IEEE Transactions on Biomedical Circuits and Systems* 13.5 (2019), pp. 882–892.

[85] N. Cermak, M. A. Wilson, J. Schiller, and J. P. Newman. “Stimjim: Open source hardware for precise electrical stimulation”. In: *bioRxiv* (2019).

[86] M. N. van Dongen, F. E. Hoebeek, S. K. Koekkoek, C. I. De Zeeuw, and W. A. Serdijn. “High frequency switched-mode stimulation can evoke post synaptic responses in cerebellar principal neurons”. In: *Frontiers in Neuroengineering* 8.MAR (2015).

[87] S. Gabriel, R. W. Lau, and C. Gabriel. “The dielectric properties of biological tissues: III. Parametric models for the dielectric spectrum of tissues”. In: *Physics in Medicine and Biology* 41.11 (1996), pp. 2271–2293.

[88] K. S. Cole and R. H. Cole. “Dispersion and Absorption in Dielectrics I. Alternating Current Characteristics”. In: *The Journal of Chemical Physics* 9.4 (1941), pp. 341–351.

[89] A. Tepljakov, E. Petlenkov, and J. Belikov. “FOMCON: a MATLAB Toolbox for Fractional-Order System Identification and Control”. In: (2011), pp. 684–689.

[90] P. F. Grant and M. M. Lowery. “Simplified parametric models of the dielectric properties of brain and muscle tissue during electrical stimulation”. In: *Medical Engineering & Physics* 65 (2019), pp. 61–67.

[91] E. Warman, W. Grill, and D. Durand. “Modeling the effects of electric fields on nerve fibers: Determination of excitation thresholds”. In: *IEEE Transactions on Biomedical Engineering* 39.12 (1992), pp. 1244–1254.

[92] G. V. Petkov. “Ion Channels”. In: *Pharmacology* (2009), pp. 387–427.

[93] M. Häusser. “The hodgkin-huxley theory of the action potential”. In: *Nature Neuroscience* 3.11s (2000), p. 1165.

[94] S. K. Kelly and J. L. Wyatt. “A power-efficient neural tissue stimulator with energy recovery”. In: *IEEE Transactions on Biomedical Circuits and Systems* 5.1 (2011), pp. 20–29.

[95] E. Noorsal, K. Sooksood, H. Xu, R. Hornig, J. Becker, and M. Ortmanns. “A neural stimulator frontend with high-voltage compliance and programmable pulse shape for epiretinal implants”. In: *IEEE Journal of Solid-State Circuits* 47.1 (2012), pp. 244–256.

[96] C.-Y. Lin, W.-L. Chen, and M.-D. Ker. “Implantable stimulator for epileptic seizure suppression with loading impedance adaptability”. In: *IEEE Transactions on Biomedical Circuits and Systems* 7.2 (2013), pp. 196–203.